Optimisation of quantitative SPECT/CT with a 360º CZT detector for ^{123}I, ^{99m}Tc and ^{177}Lu imaging

Rafaela Rodrigues Carvalhais
Master in Medical Physics
Department of Physics and Astronomy
Faculty of Sciences of the University of Porto
2026

U.PORTO
FACULDADE DE CIÊNCIAS
UNIVERSIDADE DO PORTO

MSc

Optimisation of quantitative SPECT/CT with a 360º CZT detector for ^{123}I, ^{99m}Tc and ^{177}Lu imaging

Rafaela Rodrigues Carvalhais

Dissertation carried out as part of the Master in Medical Physics

Department of Physics and Astronomy

2026

Supervisor
Prof. Dr. João António Miranda dos Santos, Medical Physics Expert, Instituto Português de Oncologia Francisco Gentil, E.P.E.; Affiliate Professor of University of Porto (ICBAS)
Co-supervisor
MSc. Vera Catarina Marques Antunes, Medical Physics Expert, Instituto Português de Oncologia Francisco Gentil, E.P.E.

Research Output

Conference Contributions

As a result of the research conducted in this dissertation, the following conference contributions were accepted:

- **Poster Communication: Carvalhais, R.**, Teixeira, J., Santos, J., Antunes, V. Optimisation of Reconstruction Parameters for Lesion Detectability in a CZT SPECT/CT Using Recovery Coefficients and Background Variability. 6^{th} European Congress of Medical Physics (ECMP) 2026, Valencia, Spain. [Accepted for Poster Communication].
- **Oral Communication:** Teixeira, J., **Carvalhais, R.**, Antunes, V., Santos, J., Duarte, H. Application of Optimised Reconstruction Parameters to Paediatric I-123 MIBG SPECT/CT: Impact on Lesion Detectability and Diagnostic Confidence. 6^{th} European Congress of Medical Physics (ECMP) 2026, Valencia, Spain. [Accepted for Oral Communication].

Journal Article

At the time of submission of this dissertation, a manuscript based on these results is in preparation and is expected to be submitted for publication in the coming weeks.

Acknowledgements

First and foremost, I would like to express my utmost gratitude to my supervisor, Prof. Dr. João Santos, for giving me the opportunity to work in such a fascinating field, which has undoubtedly contributed to my growth both scientifically and personally. I am sincerely grateful for his guidance, unwavering support, and expertise, without which this dissertation would not have been possible.

I extend a heartfelt thank you to my co-supervisor, Dr. Vera Antunes, for her dedication to making this dissertation possible, her guidance, and her daily support during my time at IPO Porto, which made this journey a truly enjoyable experience. This work would not be the same without her valuable advice and expertise.

I am also grateful to Dr. Joana Teixeira, from whom I have learned so much, for her insightful advice, willingness to help, and companionship, all of which were essential to this work.

I would like to thank IPO Porto for giving me this opportunity and for providing me with all the resources and support I needed throughout this year. I am also grateful to every professional at the Nuclear Medicine Department who, in one way or another, contributed to making this experience both enriching and memorable.

On a personal note, I would like to thank everyone in my life who has helped shape me into the person I am today and whose presence was essential to the completion of this dissertation.

To my beloved mother, thank you for giving me everything in this life. Thank you for your endless support, sacrifices, love, and friendship. Thank you for all the moments we have shared and for all those still to come. Thank you for teaching me the true meaning of family.

To my dearest father, thank you for always believing I could do anything I set my mind to. Thank you for always being available and for never shying away from helping me, even from afar.

To my first and forever friend, my brother Paulo, thank you for your companionship and endless amusing distractions throughout this year. Even without knowing it, you helped me smile through difficult days. We will always have each other.

To Rita, whose friendship means the world to me and who always supports me, no matter what chaotic plans I put her through. I extend my gratitude to João Paulo and Isabel for making me part of their family and never questioning my presence in their home.

To Mariana, Luana, Carolina, and Patrícia, for all the fun and beautiful moments we have spent together. Your friendship is a much-needed constant in my life, for which I will be forever grateful.

To André, Carlos, Matilde, José, Beatriz, and Gonçalo, whose friendship (and card games) made even the most difficult moments of this journey easier to bear, and to whom I wish the greatest success.

To Mariana C., for your friendship, companionship, and the dramatic stories that helped me decompress after long days.

To Inês, whose company throughout these past two years made my days infinitely better and whose support in the final days of this work was essential. It was a pleasure to learn and work beside you.

Finally, to João, who always has my last words. These past three years have been a whirlwind of emotions, hardships, and challenges, and I will be forever grateful to have had you by my side, supporting my dreams and carrying me through the hard days. Thank you for always believing in me even when I didn't, and for filling my life with love, light, and hope. There are no words that can possibly quantify how important your presence in my life is to me, and this dissertation would not have been possible without you, your love, and your constant support. Your love has been the pillar of my strength. Thank you for everything you have done and, most importantly, thank you for being you.

Resumo

Os detetores anelares de telureto de cádmio e zinco (CZT) representam uma das inovações mais recentes no âmbito da tecnologia SPECT. Um exemplo destes equipamentos é o sistema StarGuide SPECT/CT, recentemente instalado no IPO Porto. Este sistema faz uso do algoritmo de reconstrução Q.Clear, correspondente a uma aplicação comercial do algoritmo de verosimilhança penalizada *Block Sequential Regularised Expectation Maximisation* (BSREM). Neste âmbito, o presente estudo teve como objetivos: 1) otimizar os parâmetros de reconstrução do algoritmo Q.Clear para imagens de ^{123}I, ^{99m}Tc e ^{177}Lu, 2) avaliar o impacto destes parâmetros na qualidade de imagem, ruído e exatidão na quantificação e 3) comparar o desempenho quantitativo do sistema StarGuide com o sistema convencional disponível no IPO Porto, a câmara gama de cabeça dupla Symbia Pro.specta, que utiliza o algoritmo de reconstrução OSEM. Para tal, foi realizado um estudo de otimização para cada radionuclídeo, recorrendo a um fantoma NEMA IEC PET Body. O fantoma foi adquirido nos sistemas StarGuide e Symbia Pro.specta sob condições de aquisição semelhantes. Os dados foram reconstruídos recorrendo ao algoritmo Q.Clear com regularização *relative difference prior* (RDP) e ao algoritmo OSEM, respetivamente. Todas as imagens foram avaliadas quantitativamente utilizando como métricas os coeficientes de recuperação (RC), a variabilidade de fundo (BV), a razão sinal-ruído (SNR) e os coeficientes de recuperação de contraste (Q_H), determinadas através de ferramentas de análise de imagem desenvolvidas por recurso ao MIM Software e ao Python. Para o ^{123}I, foram realizadas vinte reconstruções Q.Clear, considerando todas as combinações possíveis dos seguintes parâmetros de regularização β e γ: $\beta = 0.01, 0.05, 0.1, 0.5, 1$; $\gamma = 0.1, 0.5, 1, 3$. Para o ^{99m}Tc e o ^{177}Lu, foram testados parâmetros de reconstrução utilizados no IPO Porto e parâmetros reportados na literatura, tendo sido selecionado para otimização adicional o protocolo com melhor desempenho em termos de recuperação de atividade. Todas as reconstruções OSEM foram realizadas utilizando as configurações clínicas aplicadas no IPO Porto e serviram como referência para a avaliação do desempenho quantitativo do algoritmo Q.Clear. Para o ^{123}I, o melhor desempenho foi obtido para valores de β entre 0.05 e 0.1 e valores de γ entre 0.5 e 1, que proporcionaram o melhor compromisso entre a exatidão na quantificação e a redução de ruído. De forma geral, os coeficientes de recuperação, a variabilidade de fundo e os coeficientes de recuperação de contraste diminuíram com o aumento de β, enquanto a razão sinal-ruído aumentou, em geral, com este parâmetro. O parâmetro γ revelou uma influência reduzida nas métricas avaliadas. Tanto para o ^{99m}Tc como para o

^{177}Lu, foram estabelecidos protocolos de reconstrução que apresentaram maior recuperação de atividade e recuperação de contraste comparativamente aos obtidos utilizando configurações de reconstrução reportadas na literatura aplicadas aos mesmos dados. De forma geral, as reconstruções Q.Clear apresentaram um desempenho semelhante (para o ^{99m}Tc) ou superior (para o ^{123}I e o ^{177}Lu) ao das reconstruções OSEM em termos de recuperação de atividade. Relativamente a Q_H, foram observadas melhorias nas imagens de ^{123}I e ^{177}Lu, particularmente para as esferas mais pequenas. Contudo, as reconstruções Q.Clear apresentaram um desempenho inferior às reconstruções OSEM em termos de ruído e razão sinal-ruído. Dado que um dos princípios orientadores do processo de otimização foi a maximização da recuperação, investigações futuras, centradas principalmente na redução do ruído, poderão ajudar a reduzir a diferença entre os dois algoritmos de reconstrução. Estes resultados demonstram a importância da otimização adequada dos parâmetros de algoritmos de reconstrução de verosimilhança penalizada, de forma a alcançar um equilíbrio aceitável entre a exatidão na quantificação e o ruído para diferentes radionuclídeos.

Palavras-chave: Reconstrução em SPECT/CT, Q.Clear, OSEM, SPECT Quantitativa, Detetor Anelar CZT, ^{123}I, ^{99m}Tc, ^{177}Lu

Abstract

A recent development in SPECT technology is the introduction of 360° cadmium-zinc-telluride (CZT) whole-body SPECT systems, such as the StarGuide SPECT/CT system, recently installed at IPO Porto. This system employs Q.Clear, a commercial implementation of the Block Sequential Regularised Expectation Maximisation (BSREM) reconstruction algorithm, a penalised-likelihood reconstruction method. This study aimed to: 1) optimise Q.Clear reconstruction parameters for ^{123}I, ^{99m}Tc and ^{177}Lu imaging, 2) evaluate their impact on image quality, noise, and quantification accuracy, and 3) compare the quantitative performance of StarGuide with the current best option at IPO Porto, the Symbia Pro.specta dual-head gamma camera using the OSEM reconstruction algorithm. To achieve this, a radionuclide-specific phantom study was conducted using a NEMA IEC Body phantom, which was acquired on both the StarGuide and Symbia Pro.specta systems under similar acquisition conditions. The data were reconstructed using Q.Clear with relative difference prior (RDP) regularisation and OSEM, respectively. The images were quantitatively assessed using recovery coefficients (RC), background variability (BV), signal-to-noise ratio (SNR), and contrast recovery coefficients (Q_H) as metrics, determined using image analysis tools developed in MIM Software and Python. For ^{123}I, twenty Q.Clear image reconstructions were performed, considering every different combination of the regularisation parameters β and γ: $\beta = 0.01, 0.05, 0.1, 0.5, 1$; $\gamma = 0.1, 0.5, 1, 3$. For ^{99m}Tc and ^{177}Lu, reconstruction settings used at IPO Porto and reported in the literature were tested, with the best-performing protocol regarding RC values selected for further fine-tuning. All OSEM reconstructions were performed using the clinical settings applied at IPO Porto and served as a reference for evaluating the quantitative performance of Q.Clear. For ^{123}I, optimal performance was achieved for β values in the range 0.05-0.1 and γ values in the range 0.5-1, yielding the best trade-off between quantitative accuracy and noise reduction. In general, RC, BV and Q_H decreased as β increased, while SNR generally increased with β. The γ parameter showed little influence on the evaluated metrics. For both ^{99m}Tc and ^{177}Lu, optimal protocols that presented superior RC and Q_H values compared to those obtained using literature-reported reconstruction settings applied to the same data were achieved. In general, Q.Clear reconstructions performed similarly (for ^{99m}Tc) or superiorly (for ^{123}I and ^{177}Lu) to the OSEM reconstructions in terms of quantitative accuracy as measured by RC. Regarding Q_H, improvements were observed for the ^{123}I and ^{177}Lu images, particularly for the smallest spheres of the phantom. However, Q.Clear reconstructions were generally outperformed by the OSEM reconstructions in terms of image noise and SNR. As one of the guiding principles during the optimisation process was to maximise recovery, further investigation, primarily focused on noise reduction, could help close the gap between the two reconstruction algorithms. These findings highlight the importance of appropriate optimisation of penalised-likelihood algorithms reconstruction parameters to achieve an optimal balance between quantitative accuracy and image noise across radionuclides.

Keywords: SPECT/CT Image Reconstruction, Q.Clear, OSEM, Quantitative SPECT, CZT Ring Detector, ^{123}I, ^{99m}Tc, ^{177}Lu

Table of Contents

List of Tables

List of Figures

List of Abbreviations

^{123}I	Iodine-123
^{177}Lu	Lutetium-177
^{99m}Tc	Technetium-99
AC	Attenuation Correction
BSREM	Block Sequential Regularised Expectation Maximisation
C3D	Clarity 3D
CT	Computed Tomography
CZT	Cadmium-Zinc-Telluride
DEW	Dual-Energy-Window
EANM	European Association of Nuclear Medicine
FBP	Filtered Backprojection
GP	General-Purpose
HE	High-Energy
HR	High-Resolution
HS	High-Sensitivity
HU	Hounsfield Units
LE	Low-Energy
MELP	Medium Energy Low Penetration
MLEM	Maximum-Likelihood Expectation Maximisation
MRP	Median Root Prior
OSEM	Ordered Subset Expectation Maximisation
PET	Positron Emission Tomography
PL	Penalised-Likelihood
PMT	Photomultiplier Tube

PSF	Point Spread Function
PVE	Partial Volume Effect
Q_H	Contrast Recovery Coefficient
RC	Recovery Coefficient
RDP	Relative Difference Prior
ROI	Region of Interest
SC	Scatter Correction
SNR	Signal-to-Noise Ratio
SPECT	Single-Photon Emission Computed Tomography
TEW	Triple-Energy-Window
TRT	Targeted Radionuclide Therapy
VOI	Volume of Interest

1. Introduction

1.1. Motivation

Recent developments in SPECT/CT detection technology include the rising popularity of CZT detectors, associated with higher energy resolution, higher sensitivity, and innovative acquisition geometries when compared to their Anger counterparts [1]. Additionally, in the SPECT image reconstruction domain, the iterative reconstruction algorithm OSEM has been established as the routine reconstruction algorithm used in clinical applications. Nevertheless, new reconstruction approaches are emerging, focused on compensating for OSEM's downsides, such as the increase in image noise with the number of iterations. One such approach is the Q.Clear reconstruction algorithm, a penalised-likelihood algorithm based on the BSREM framework. This algorithm has been introduced as part of the whole-body $360°$ CZT-based StarGuide SPECT/CT system, recently installed at IPO Porto.

The installation of new imaging equipment in a Nuclear Medicine department is accompanied by the need to explore its new functionalities and to establish its performance baselines. This allows for its efficient integration into routine clinical practice. Within this context, this study aimed to explore the new reconstruction paradigm introduced by Q.Clear. Whilst OSEM reconstruction was routinely employed at IPO Porto, and OSEM has been extensively studied in the literature, the same cannot be said for Q.Clear, whose first application in the SPECT domain is precisely the StarGuide SPECT/CT system. Consequently, as examinations involving different radionuclides started being performed on the StarGuide system at IPO Porto, there was a need to explore and optimise Q.Clear to ensure its best performance.

1.2. Objectives

The main objective of this study was to explore, assess, and optimise the reconstruction settings of the Q.Clear reconstruction algorithm for ^{123}I, ^{99m}Tc, and ^{177}Lu imaging.

The radionuclides selected for this study were chosen to represent three clinically relevant and strategically important use cases for CZT-based SPECT imaging. ^{99m}Tc was included as the standard reference radionuclide in nuclear medicine imaging, providing a well-established benchmark against which the performance of Q.Clear reconstruction could be assessed. ^{177}Lu was selected because of its central role in molecular radiotherapy, theranostics, and patient-specific dosimetry, making it a natural and clinically important target for quantitative CZT-SPECT optimisation. ^{123}I was included as a diagnostically and dosimetrically relevant radionuclide whose image acquisition and quantification are more challenging, due to factors such as higher-energy emissions, septal penetration, scatter contribution, and the need for careful validation of reconstruction and correction strategies. This selection was intended to assess Q.Clear under conditions of increasing quantitative complexity: from the conventional and widely standardised case of ^{99m}Tc, through the therapeutically and dosimetrically relevant case of ^{177}Lu, to the more technically demanding case of ^{123}I, for which image acquisition and quantitative validation remain particularly challenging.

As part of the optimisation process, two additional objectives were considered: to evaluate the impact of Q.Clear reconstruction parameters on image quality and quantitative metrics, and to achieve quantitative performance equal to or superior to that obtained with images reconstructed using OSEM on a standard dual-head Anger-based camera.

1.3. Structure

This dissertation is divided into five chapters. In the present chapter, the motivation of this work and the objectives of this study were presented. Chapter 2 provides an overview of SPECT detection technology, image reconstruction approaches, and quantitative SPECT. It also describes the novel SPECT/CT system used in this study and establishes the theoretical foundation of the reconstruction algorithm investigated. Chapter 3 outlines the methodology employed in this study, focusing on phantom preparation, image acquisition, image reconstruction and image analysis. Chapter 4 presents and discusses the findings of this study. Finally, chapter 5 summarises the key findings of this study, highlights their significance for the field of SPECT image reconstruction, and offers suggestions for future work.

2. State of the Art

The recent technological advances in SPECT/CT are marked by the shift from NaI(Tl)-based gamma cameras to CZT-based systems and by the expansion of the image reconstruction process, with the introduction of penalised-likelihood algorithms, such as BSREM, that allow for greater customization of the reconstruction process when compared to the well-established OSEM algorithm. The progress made in acquisition geometry, detector hardware, and image reconstruction techniques has helped transition SPECT into a quantitative imaging modality. Within this context, this chapter provides an overview of SPECT detector hardware, starting with the conventional Anger camera and culminating in the recently introduced whole-body 360° systems based on CZT technology. The image reconstruction process is then described, from the traditional filtered back-projection method to the latest iterative reconstruction approaches. Finally, an overview of quantitative SPECT is provided, concluding with a review of the characteristics of the radionuclides used in this study.

2.1. SPECT/CT Imaging

Nuclear Medicine can be defined as the clinical field that oversees the administration of compounds labelled with radionuclides into a patient's body for diagnostic and/or therapeutic purposes. These labelled compounds, referred to as *radiopharmaceuticals* or *radiotracers*, produce a three-dimensional (3D) activity distribution within the patient's body. Radiopharmaceuticals are specifically designed to target tissues based on the pathology of interest. Consequently, SPECT imaging provides detailed physiological and functional information about the targeted tissues [2].

Nuclear Imaging refers to the process of creating an image of the radiopharmaceutical's distribution within the body. *Single Photon Emission Tomography* (SPECT) is the nuclear medicine imaging modality used for radionuclides that emit γ radiation [3]. γ-ray detectors are known as *gamma cameras*. In SPECT, one or more gamma cameras rotate around the patient's body, acquiring γ-ray emission data for several angular positions. For a given angle, the acquired data are reffered to as a *projection*. These projection data are then used to produce a 3D image of the activity distribution within the patient, in a process known as *image reconstruction*, described in detail in section 2.2 of this chapter. Conventional SPECT systems consist of two detectors that rotate around the patient's body, typically acquiring data over a 180° arc for each detector, following circular or body contouring orbits [4]. These systems are known as *dual-head* cameras.

SPECT/CT is a hybrid imaging modality that combines functional and physiological SPECT data with detailed anatomical data from CT. SPECT/CT addresses two well-known limitations of SPECT: the lack of precision in assigning sites of high radiotracer uptake, when compared to the surrounding tissues, to specific anatomic locations, as SPECT alone provides no anatomical reference, and the need of using transmission measurements obtained with radioactive sources to apply attenuation correction [4, 5]. The SPECT and CT scanners are installed sequentially and share the exam table. The CT scan provides an attenuation map of the patient's body, which can be used to correct for γ-ray attenuation. The SPECT scan and the CT scan are precisely aligned to match radiotracer uptake sites with their corresponding anatomical locations, producing *fusion* images.

2.1.1 Anger Gamma Camera

Most SPECT detectors are based on the Anger gamma camera, developed by Hal Anger [6]. The main components of an Anger gamma camera are a collimator, a scintillation crystal, a light guide, and an array of photomultiplier tubes (PMTs) (figure 2.1) [3]. When

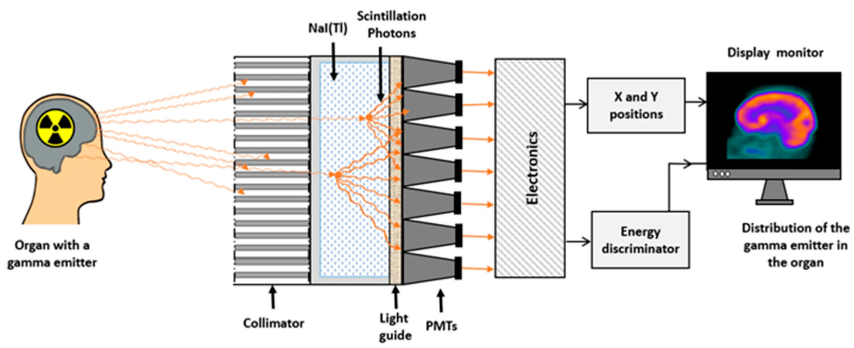

Figure 2.1: Schematic representation of a conventional gamma camera [1].

a γ-ray interacts with the scintillation crystal, light photons are produced. These photons travel through the scintillator and reach the PMTs, where they are converted into electrical signals. Typically, the scintillation crystal used is thallium-doped sodium iodide (NaI(Tl)). NaI(Tl) has a high light output and can be manufactured in large-area crystals with suitable size for body imaging. The PMTs are coupled to the crystal and are positioned, typically, in a close-packed hexagonal array [7]. Inside a PMT, light photons interact with the *photocathode*, a surface that emits electrons when struck by photons. These electrons are accelerated toward a *dynode*, a metal electrode held at a positive potential, which emits secondary electrons upon impact. This process is repeated for a given number of dynodes, and the resulting electrons are collected at the anode, producing a large current pulse, proportional to the energy deposited by the γ-ray in the crystal [3].

To determine the position of a scintillation event, the centroid of the position-weighted PMT signals, $(\hat{x}, \hat{y})$, is computed, in a process known as *Anger logic* [6]:

$$\hat{x} = \frac{\sum_{S_i \geq S_{min}} x_i \, w\left(x_i, S_i\right)}{\sum_{S_i \geq S_{min}} w\left(x_i, S_i\right)}; \quad \hat{y} = \frac{\sum_{S_i \geq S_{min}} y_i \, w\left(y_i, S_i\right)}{\sum_{S_i \geq S_{min}} w\left(y_i, S_i\right)} \tag{2.1}$$

where S_i is the signal from the PMT at position (x_i, y_i), S_{min} is an amplitude threshold, and w is the PMT signal weighted according to a predefined scheme. In the simplest case, w is equal to the raw signal, S_i [7]. The outputs from each PMT are summed and analysed by a *pulse height analyser*. Only signals with amplitudes within a predefined energy window, known as the *photopeak* energy window, are accepted and associated with the corresponding $(\hat{x}, \hat{y})$ location of the scintillation event [8].

The collimator is a crucial component of a gamma camera, as it defines the direction of the detected γ photons. The parallel-hole collimator is the most commonly used in SPECT [3, 8]. It consists of a plate with multiple holes parallel to each other and separated by equally spaced partitions, the *septa*. It is typically made of a material with high atomic number and stopping potential material, such as lead or tungsten [4, 8]. γ-rays that are not travelling parallel to the holes' axis are absorbed by the septa. As a result, only a reduced fraction of the γ-rays emitted from the patient's body reach the crystal, leading to SPECT's reduced detection efficiency when compared to Positron Emission Tomography (PET) [5] and lower image quality [3].

Some high energy γ photons that are not travelling perpendicular to the detector surface can penetrate the septa and be detected. This phenomenon, known as *septal penetration*, leads to image blurring, as the SPECT system assumes that all detected photons follow the direction defined by the collimator. To limit this phenomenon, the septal thickness of parallel-hole collimators is defined according to the energy of the γ photons emitted by the imaged radionuclide. These collimators are classified as *low-* (up to $150\,keV$), *medium-* (up to $400\,keV$) and *high-energy* collimators (LE, ME, and HE, respectively), with septal thickness increasing accordingly [8].

Collimator efficiency, E_g, can be defined as the number of γ photons that pass through the collimator holes per unit of activity of the source [8]. For a parallel-hole collimator, it is given by:

$$E_g \propto \frac{d^4}{a_{eff}^2 (d+t)} \tag{2.2}$$

where d is the hole diameter, t is the septal thickness and a_{eff} is the effective length of the hole [8, 9]. The hole length, a, can be empirically corrected for septal penetration by using an effective hole length $a_{eff} = a - 2\mu$, where μ is the linear attenuation coefficient for the collimator material [3, 8]. The spatial resolution of a collimator, R_g, can be empirically determined as the full width at half maximum (FWHM) of the radiation profile obtained from γ-ray point source, known as the *point spread function* (PSF) [3]. R_g can be computed as:

$$R_g = \frac{d(a_{eff} + b + c)}{a_{eff}} \tag{2.3}$$

where b is the distance from the point source to the collimator face and c is the distance from the collimator back to the crystal's midplane [9]. Consequently, increasing the hole diameter, d, or decreasing the hole length, a, improves the collimator efficiency, at the expense of degrading the spatial resolution. Parallel-hole collimators can, subsequently, be further classified as *high-resolution* (HR), *high-sensitivity* (HS) or *general purpose* (GP), with the latter considering intermediate values of the collimator parameters to provide a balance between efficiency and spatial resolution. Naturally, high-resolution collimators will have longer and narrower holes than high-sensitivity collimators.

Although the Anger gamma camera remains the foundation of most currently used SPECT detectors [5], it has some limitations. Its design is typically bulky to accommodate the large scintillation crystal, the PMTs and associated electronics [10]. Light photons can also be lost at the interface between the scintillator and the PMTs, thereby degrading image quality and limiting energy resolution [1, 11]. The energy resolution represents the system's capability of discriminating between distinct deposited energies. It can be computed as the ratio of the FWHM of the energy peak to the energy of the corresponding γ photon [12]. Additionally, Anger logic, which is used to determine the position of a scintillation event, breaks down near the edges of the detector, resulting in several centimetres of "dead" space [11]. To address this limitation, some gamma camera designs replace the standard continuous scintillation crystal with an array of small individual scintillation elements, known as *pixels*. In pixelated detectors, the position of an event is determined based on the pixel in which the signal originates, allowing full use of the detection area, as "dead" space is no longer a concern [13]. Pixelated crystals reduce the lateral spread of scintillation light within the crystal, thus improving spatial resolution [14]. Their thickness is typically reduced to ensure that each detected signal can be attributed to a single pixel. This reduction limits the stopping power, thereby hampering the system's sensitivity and energy resolution. The sensitivity of a gamma camera can be defined as the number of counts per unit time detected per unit of activity present in a source [8]. Moreover, conventional NaI(Tl) present moderate intrinsic spatial resolution * - $3 \sim 5\,mm$ at $140\,keV$ [15] - and energy resolution, particularly for γ photons with energy lower than $200\,keV$ [1]. To overcome the limitations of conventional SPECT systems, novel detection technologies have emerged, such as solid-state detectors. Among these, cadmium-zinc-telluride (CZT) detectors represent a paradigm shift in SPECT technology, offering higher sensitivity, improved energy resolution and a more compact design, and have become widely used, particularly in cardiac imaging applications [1, 15].

2.1.2 CZT Gamma Camera

Semiconductor detectors directly convert γ photons into electrical signals. When a γ-ray is absorbed by the semiconductor, electron-hole pairs are generated. A bias voltage is applied across the semiconductor using two electrodes, causing the charge carriers to drift towards the one they are attracted to, thereby inducing a current on the electrodes. The amplitude of the resulting electrical signal is proportional to the energy deposited by the γ-ray [11, 12]. Semiconductor detectors are often pixelated, with each pixel being usually associated with a single anode for electron collection [13, 16]. Compared to conventional scintillation detectors, semiconductor detectors have higher energy resolution due to the direct conversion mechanism: the production of an electron-hole pair requires an energy of $3 - 6\,eV$, compared to $\sim 30\,eV$ needed to produce scintillation light in a standard NaI(Tl) crystal [14]. The limit energy resolution, R_{limit}, for a given detector material can be computed as the Poisson limit resolution, given by:

$$R_{limit} = 2.35\sqrt{\frac{F}{N}} \tag{2.4}$$

where F is the Fano factor†, that can be defined as the ratio of the variance to the mean of a given integer-value variable [17], such as the number of photons or charge carriers produced, and N is the number of carriers [12]. As a significantly lower energy is needed to produce electron-hole pairs, semiconductors benefit of an increased number of carriers, which contributes to an improvement in energy resolution [18]. CZT detectors have

*The limit of spatial resolution achieved by the SPECT detector and associated electronics, not considering the contribution of the collimator [3].

†The Fano factor depends on the detector material and is approximately 1 for scintillation detectors. For CZT detectors, the Fano factor has been measured as 0.089 ± 0.05 [12].

become widely used because they overcome some limitations of other semiconductors, such as Ge or Si-based semiconductors. These detectors, such as high-purity germanium (HPGe) [11], must be operated at a low temperature to avoid thermally induced currents. CZT detectors can operate at room temperature without excessive electronic noise and also benefit from a high effective atomic number, resulting in high stopping power [3, 14]. According to Hutton et al. [13], CZT commercially available systems typically have an energy resolution around 5.5%, compared to $9-10\%$ for conventional gamma camera systems.

The CZT energy spectrum typically presents a significant tail on the lower-energy side of the photopeak - *tailing effect* (figure 2.2). CZT crystals may have some impurities, which create energy levels near the band gap, causing some charge carriers to become trapped in these levels for a significant amount of time. Simultaneously, electron-hole pairs can recombine before the charge carriers are collected at the electrodes. *Charge trapping* and *recombination* lead to the detection of fewer charge carriers and, consequently, a γ-ray interaction can be recorded as a lower-energy event [18, 19]. Moreover, the electron cloud generated by a γ-ray interaction disperses as it moves towards the anodes. If its radius is bigger than the pixel target anode area, part of the charge can be shared between pixels, in a phenomenon known as *charge sharing*. Consequently, primary photons are recorded outside of the photopeak area [16]. Collectively, these events contribute to the observed tail. The first commercially available CZT SPECT camera was the cardiac-dedicated D-

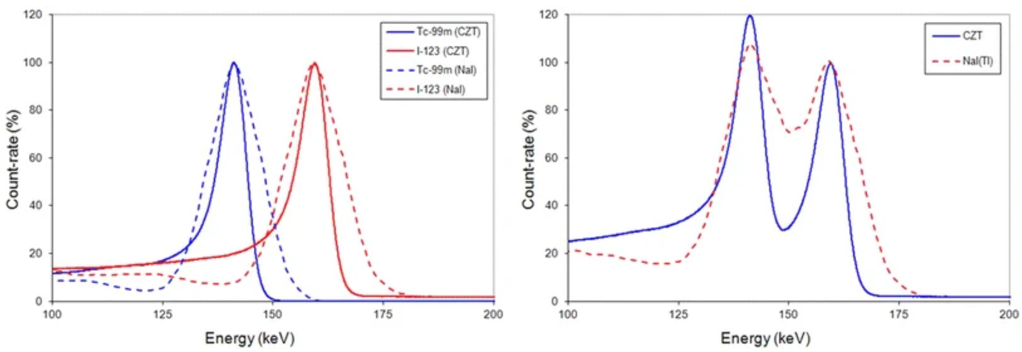

Figure 2.2: Representative spectra for ^{99m}Tc and ^{123}I acquired with CZT (solid line) and NaI(Tl) (dashed line) detectors (left), along with the corresponding combined dual-radionuclide spectra (right) [13].

SPECT system (Spectrum Dynamics, Caesarea, Israel) [10]. The D-SPECT system features 9 arrays of CZT detectors arranged in a $90°$ geometry, dedicated to cardiac imaging. Upon its introduction, the D-SPECT system showed higher energy resolution and superior sensitivity when compared to a conventional gamma camera [20]. Since then, significant progress has been made in this field, with the introduction of rectangular digital detector systems, such as the NM/CT 870 CZT model (GE Healthcare, Haifa, Israel), as well as whole-body systems equipped with flat CZT panels, such as the CZT SPECT/CT DNM 670 CZT (GE Healthcare) [10].

Recently, a new CZT SPECT design has been introduced to the market: $360°$ CZT whole-body SPECT systems, also known as 3D-ring CZT SPECT systems. To date, two SPECT/CT systems have been developed with this SPECT design: VERITON* (Spectrum Dynamics), introduced in 2017, and StarGuide (GE Healthcare), introduced in 2021 [21].

2.1.2.1 StarGuide SPECT/CT System

StarGuide combines GE Healthcare's Optima CT540 CT scanner with a ring-shaped SPECT gantry. A total of 12 CZT detectors are evenly distributed around the $360°$ gantry (figure 2.3). Each detector is composed of 7 CZT modules, forming an axial field of view

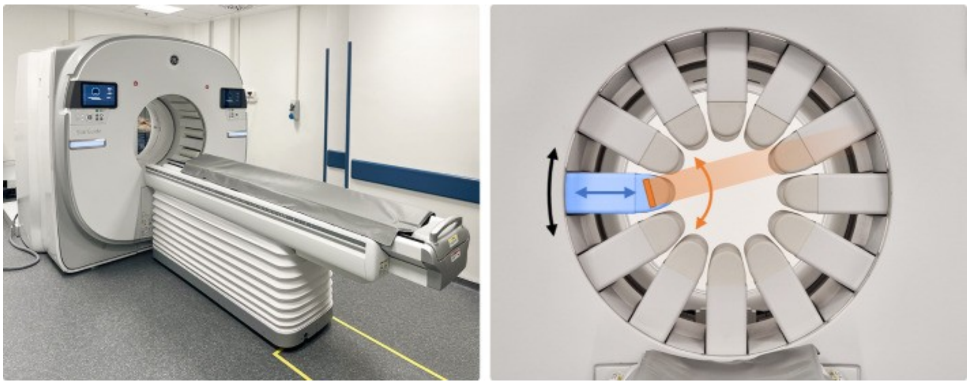

Figure 2.3: StarGuide SPECT/CT system (left) and StarGuide detector motion range (right) [22].

(FOV) of $27.5\,cm$. Each module contains a 16×16 pixel matrix, with an individual pixel size of $2.46 \times 2.46\,mm^2$. The CZT crystals have a thickness of $7.25\,mm$, granting StarGuide an imaging energy range of $40 - 279\,keV$. Additionally, each detector is coupled to a fixed LEHR dual-channel tungsten collimator, that inhibits the imaging of low- and medium-energy radionuclides without having to exchange the collimator. Consequently, StarGuide can image both ^{177}Lu energy peaks ($113\,keV$ and $208\,keV$) [23–25].

The detector arms are capable of independent radial motion (inward or outward). They can also rotate simultaneously with the gantry, allowing acquisitions in various angular

*Currently, two models of the VERITON system are available: one designed for photons up to $200\,keV$ (VERITON 200), and another capable of imaging photons with higher energies (VERITON 400) [21].

positions. For a given acquisition position, the tip of each detector arm will swivel during the scan. The detector sweep rate over the FOV can be set to be constant or to be slowed down over a user-defined region of interest (ROI) to collect more data from that region (*focused* acquisition mode) [21–23]. A sensor ring, comprised of transmitting and receiving infrared diodes is coupled to the front of the SPECT gantry. Using this infrared technology, an optical scout of the imaged object is conducted prior to the SPECT acquisition. The data from this scout is used to define the position of the table and to optimise the radial position of each detector arm [23, 25].

The StarGuide system has been shown to acquire faster whole-body scans, being able to perform vertex to mid-thigh scans in 12 minutes, compared to 32 minutes for a standard dual-head camera, thereby increasing patient comfort [26]. Andelius et al. [27] reported the successful implementation of the StarGuide system in routine clinical practice for bone, cardiac and lung imaging using ^{99m}Tc-labelled radiopharmaceuticals, with image quality comparable to that of conventional dual-head cameras. Zorz et al. [22] evaluated the performance of the StarGuide system according to the NEMA NU 1-2018 standards, with adaptions to accommodate its novel design. The StarGuide system presented an energy resolution of $5-6\%$ for all radionuclides considered, representing a twofold increase compared to conventional NaI(Tl) cameras. Moreover, the spatial resolution was superior to that of a conventional system, as well as the measured volume sensitivity *.

Stenvall et al. [24] showed that the StarGuide system is a viable alternative to conventional dual-head Anger cameras for ^{177}Lu quantitative imaging, demonstrating a lower bias in activity-concentration estimation when using the $113\,keV$ energy window, while performing similarly to the Anger system for imaging at the $208\,keV$ peak. Images acquired at $208\,keV$ were visually similar between the two systems, whereas those acquired at $113\,keV$ with StarGuide system appeared sharper.

A known limitation of the StarGuide system in the context of ^{177}Lu imaging is septal penetration. As StarGuide collimators are optimised for both low- and medium-energy radionuclides, a higher fraction of $208\,keV$ photons penetrates the septa compared to traditional medium-energy collimators [23]. As stated by Danieli et al. [23], in the first quantitative ^{177}Lu SPECT/CT study performed with the StarGuide system, septal penetration can negatively affect both quantification accuracy and recovery coefficients, while also introducing artefacts such as axial streaks near hot lesions. A similar effect was observed by Stenvall

*The volume sensitivity accounts for the number of detected events per unit of concentration for a uniform activity concentration in a cylindrical phantom [3].

et al. [24] in the images of an anthropomorphic phantom with spherical hot lesions, when using the $208\,keV$ energy window.

In addition to StarGuide, two other CZT whole-body SPECT/CT systems are currently available: VERITON 200 and VERITON 400 (Spectrum Dynamics). These systems operate similarly to StarGuide, sharing the acquisition geometry, with VERITON 200 limited to photons up to $200\,keV$, and VERITON 400 enabling acquisition beyond this limit. In the first comparative study of these three systems, using ^{99m}Tc and ^{177}Lu-filled phantoms, Hoog et al. [21] showed that, although the VERITON cameras exhibited higher sensitivity and energy resolution, StarGuide produced images of comparable quality. The cameras behaved similarly in ^{99m}Tc imaging, whereas StarGuide and VERITON 400 showed a greater potential for ^{177}Lu imaging due to the dual-peak acquisition. However, the collimator design of StarGuide, which enables this feature, was identified as a primary factor contributing to its reduced sensitivity compared to the other systems. Despite the recent advancements in acquisition geometry, no specific standards for these novel systems are available, hampering standardised comparison and performance evaluation of these systems [22]. Within this context, a common limitation is the use of main and scatter energy windows inherited from conventional Anger cameras, which do not fully exploit the improved energy resolution of CZT detectors, with further studies being required to define appropriate window settings [21, 24, 27, 28].

2.2. SPECT Image Reconstruction

The process of *image reconstruction* corresponds to the generation of a three-dimensional (3D) image of the source activity distribution from two-dimensional (2D) projection data. Typically, the projection data are reconstructed into tomographic images, corresponding to cross-sectional images of the imaged object at a given plane. The collection of these tomographic images, also known as *slices*, forms the 3D dataset [29]. The projection data are processed by specialised mathematical methods, know as *reconstruction algorithms*. Based on their mathematical treatment of the projection data, reconstruction algorithms can be classified as analytic or iterative.

2.2.1 Analytic Reconstruction

The analytic approach to SPECT image reconstruction relies on the *line integral* model to describe the data acquisition. The line integral model, also known as the Radon model, neglects physical phenomenons such as photon attenuation and scattering [30]. The geometry of the data acquisition is illustrated in figure 2.4. $f(x,y)$ corresponds to the

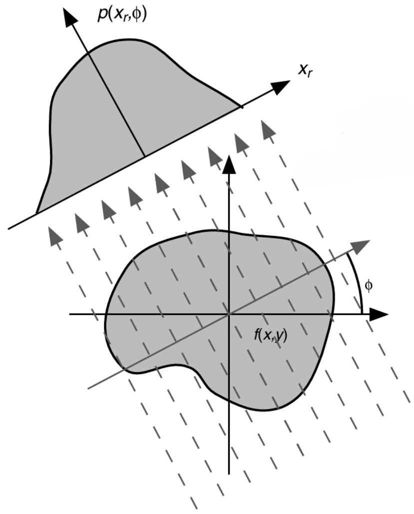

Figure 2.4: Geometry of data acquisition considered for the 2D Radon model [30].

radiotracer distribution within the considered slice and $p(x_r, \phi_i)$ corresponds to the number of counts recorded at location x_r on the detector for the acquisition angle ϕ_i. Ideally, only photons with direction parallel to the collimator holes' axis are potentially detected. For each location x_r on the detector and for each acquisition angle ϕ_i, this direction is defined by a line with the equation [29]:

$$s_i = x\, cos\phi_i + y\, sin\phi_i \tag{2.5}$$

In this idealised SPECT system, the total number of counts recorded by a detector for a given volume of interest (VOI) is proportional to the amount of radioactivity contained in that VOI [3, 29, 30]. Consequently, $p(x_r, \phi_i)$ corresponds to the sum of values $f(x,y)$ along the corresponding line and can be written as [29]:

$$p(x_r, \phi_i) = \int_{-\infty}^{+\infty} f(x,y)du \tag{2.6}$$

where u the defines the location of the points along the considered line. Equation 2.6 corresponds to the line integral of $f(x,y)$ along the given line or, equivalently, the Radon transform of the function $f(x,y)$. In practice, $p(x_r, \phi_i)$ is acquired at discrete angles ϕ_i and sampled at discrete intervals across x_r, and the slice is reconstructed on a 2D matrix of discrete pixels in the (x,y) coordinate system [3]. The set of projection data $p(x_r, \phi_i)$ can be organized into a 2D matrix - the *sinogram* - where each row corresponds to an angle ϕ_i and each column corresponds to a position x_r on the detector. Each matrix entrance, $p(x_r, \phi_i)$, defines a *bin*. Following the formalism presented by [29], the rows of the matrices can be stacked to obtain two vectors: $\mathbf{f} = \{f_i : i = 1, ..., N\}$, where

f_i represents the radioactivity within pixel i and N represents the number of pixels, and $\mathbf{g} = \{g_j : j = 1, ..., M\}$, where g_j represents a bin and M the number of bins. Therefore, $\mathbf{g}$ can be understood as the projection of $\mathbf{f}$ onto the detector as allowed by the implemented collimation:

$$\mathbf{g} = \mathbf{P}\,\mathbf{f} \tag{2.7}$$

where $\mathbf{P}$ is called the *forward projection operator*, mathematically defined by the discrete Radon transform [29]. The reconstruction problem can, accordingly, be defined as: *Given the projection data* $\mathbf{g}$*, what is the activity distribution* $\mathbf{f}$*?* This problem requires the inversion of a discrete form of the Radon transform and can be solved by filtered backprojection (FBP) [30].

2.2.1.1 Filtered Backprojection

FBP is the most widely used analytic reconstruction method [31]. The discrete backprojection operator can be defined as:

$$b(x, y) = \sum_{j=1}^{N_p} p(s_j, \phi_j)\Delta\phi \tag{2.8}$$

where N_p is the number of projections and $\Delta\phi = \frac{\pi}{N_p}$ represents the angular step between projections [3, 29]. Ideally, no new information should be added by the data acquired for $\phi \in [\pi, 2\pi]$ due to the periodicity and symmetry properties of $p(x_r, \phi)$: $p(x_r, \phi) = p(x_r, \phi + 2\pi)$ and $p(x_r, \phi) = p(-x_r, \phi + \pi)$. Therefore, ϕ can be limited to π radians and $\Delta\phi = \frac{\pi}{N_p}$ [29, 30]. Conceptually, for a pixel (x, y), all $p(s_j, \phi_j)$ values, each one corresponding to the projection of the pixel along a direction s_j (equation 2.5), are summed and the resultant value is divided by the number of projections acquired and assigned to the reconstructed pixel. Consequently, each $p(s_j, \phi_j)$ value is *uniformly* placed back - *backprojected* - into the image matrix along the corresponding s_j direction. As such, all pixels along s_j receive the same value, regardless of their actual contribution to $p\left(s_j, \phi_j\right)$. The final result is a blurred representation of $f(x, y)$, as counts are inevitably misplaced across the reconstruction matrix [3, 29]. In FBP, the projection data are first transformed into the frequency domain through the application of a Fourier transform. In this domain, a reconstruction filter, known as a *ramp filter*, is applied to the transformed data. This filter amplifies high-frequency components while suppressing low-frequency components, thereby compensating for the blurring effect. The filtered data are then subjected to conventional backprojection, resulting in an improved reconstruction [3].

2.2.2 Iterative Reconstruction

Currently, iterative reconstruction represents the standard approach to SPECT reconstruction [5]. The accuracy of analytically reconstructed SPECT images is limited due to the approximations inherent in the line integral model, particularly, the neglect of the randomness of the γ-ray detecting process and the neglect of physical phenomena, such as attenuation and scattering. The former contributes to reconstructed images with a high level of noise [18] and the latter obligates to the development of analytic models of the corresponding phenomena to compensate them. Typically, these models are computationally demanding and are not optimised for low-count data [31]. Iterative reconstruction methods can explicitly incorporate the physical and statistical properties of a SPECT system, and, consequently, are preferred over analytic reconstruction methods, despite being computationally more demanding.

The iterative reconstruction problem can be written as $\mathbf{g} = \mathbf{P}\,\mathbf{f}$, where $\mathbf{f} = \{f_i : i = 1, ..., N\}$ represents the unknown activity distribution, with f_i corresponding to the activity within the *ith* voxel out of a total of N voxels. $\mathbf{g} = \{g_j : j = 1, ..., M\}$ denotes the acquired projection data, with g_j corresponding to the *jth* measurement among M measurements. $\mathbf{P}$, known as the SPECT *system matrix*, contains information about the imaging process, with P_{ij} representing the mean contribution of voxel j to measurement i [31, 32].

In essence, the iterative method develops as follows [8]: An initial guess, $\hat{\mathbf{f}}^{\mathbf{0}}$, is used to obtain an estimate of the projection data, $\hat{\mathbf{g}}^{\mathbf{0}}$, such that $\hat{\mathbf{g}}^{\mathbf{0}} = \mathbf{P}\,\hat{\mathbf{f}}^{\mathbf{0}}$. The measured projection data, $\mathbf{g}$, is then compared to $\hat{\mathbf{g}}^{\mathbf{0}}$. Based on this comparison, the initial image estimate is updated according to a numerical optimiser algorithm [31], originating a new image estimate, $\hat{\mathbf{f}}^{\mathbf{1}}$. This process is repeated for $\hat{\mathbf{f}}^{\mathbf{1}}$, and for all subsequent image estimates, $\hat{\mathbf{f}}^{\mathbf{k}}$, until a predefined satisfaction criterion is achieved.

2.2.2.1 Maximum-Likelihood Criterion

The probability of obtaining the projection data $\mathbf{g}$, given the activity distribution $\mathbf{f}$, corresponds to the *conditional probability* of $\mathbf{g}$ given $\mathbf{f}$ or, simply, to the *likelihood* function $p(\mathbf{g}|\mathbf{f})$. According to the maximum-likelihood criterion, the best estimate, $\hat{\mathbf{f}}$, of the activity distribution is the one that maximises $p(\mathbf{g}|\mathbf{f})$. As the logarithm function is monotonic, maximising the log-likelihood function, $L(\mathbf{g}|\mathbf{f})$, produces equivalent solutions to maximising the likelihood function [31]. Provided that detector dead time can be neglected and that the data has not undergone any correction, both γ-ray emissions and detections are known to follow the independent Poisson distribution [32, 33]. Consequently, $g_i \sim Poisson\left([Pf]_i + r_i\right)$, and:

$$p(\mathbf{g}|\mathbf{f}) = \prod_{i=1}^{M} \frac{\overline{g_i}^{g_i} e^{-\overline{g_i}}}{g_i!} \quad (2.9)$$

where $\overline{g_i}$ represents the expected value of measurement g_i, and is given by $\overline{g_i} = [Pf]_i + r_i = \sum_{i=1}^{M} P_{ij} f_i + r_i$. r_i represents the expectations of scatter and background events [31]. $L(\mathbf{g}|\mathbf{f})$ assumes the form:

$$L(\mathbf{g}|\mathbf{f}) = \sum_{i=1}^{M} g_i\, ln(\overline{g_i}) \;-\; \overline{g_i} - ln(g_i!) \quad (2.10)$$

In this framework, the function to be maximised is reffered to as the *objective* function: $\phi(\mathbf{f}) = L(\mathbf{g}|\mathbf{f})$.

2.2.2.2 MLEM and OSEM

The maximum-likelihood expectation maximisation (MLEM) algorithm, introduced by Shepp and Vardi [34], computes image estimates based on the ML criterion. Considering an old image estimate, $\hat{\mathbf{f}}^{(\mathbf{n})}$, a new image estimate, $\hat{\mathbf{f}}^{(\mathbf{n+1})}$, can be obtained by applying the following update equation:

$$\hat{f_j}^{(n+1)} = \frac{\hat{f_j}^{(n)}}{\sum_q P_{qj}} \sum_i P_{ij} \frac{g_i}{\sum_k P_{ki} \hat{f_k}^{(n)} + r_i} \quad (2.11)$$

Briefly, projection estimates are computed by applying the system matrix $\mathbf{P}$ to $\hat{\mathbf{f}}^{\mathbf{n}}$. The resulting projections are then compared to the measured projections by dividing the latter by the former. This ratio is backprojected, normalised and multiplied by the previous image estimate to produce an updated one. This entire sequence constitutes one iteration of the algorithm. A disadvantage of MLEM corresponds to its slow rate of convergence to the ML solution. As such, a high number of iterations, typically 30 to 50, is necessary to reach a usable solution [32].

To accelerate the rate of convergence of MLEM, Hudson and Larkin [35] introduced an extension of this algorithm, known as the ordered subset expectation maximisation (OSEM) algorithm. In this framework, the projection data is grouped into ordered subsets - $S_1, ..., S_m$ -, and the objective function is divided into a sum of sub-objective functions, each valid for a given subset of data:

$$\phi(\mathbf{f}) = \sum_{m=1}^{N_s} \phi_m(\mathbf{f}) \tag{2.12}$$

where N_s represents the number of subsets and $\phi_m(\mathbf{f})$ is a function of subset S_m [31, 35]. The MLEM algorithm is applied to each subset, using the reconstruction that resulted from the previous subset as the initial image estimate. An OSEM iteration is completed when the MLEM algorithm has been applied to all the subsets. The algorithm's update equation is given by:

$$\hat{f}_j^{(m,n+1)} = \frac{\hat{f}_j^{(m,n)}}{\sum_{q\in S_m} P_{qj}} \sum_{i\in S_m} P_{ij} \frac{g_i}{\sum_k P_{ik}\hat{f}_k^{(m,n)} + r_i} \tag{2.13}$$

where $\hat{f}_k^{(m,n)}$ represents estimate $\hat{f}_k$ at subset m and iteration n [31].

Iterative algorithms based on the ML criterion enforce maximum consistency between the reconstructed image and the projection data. Since SPECT projection data are inherently noisy, the reconstructed image are likewise noisy [32, 36]. The noise is known to increase with the number of iterations, as increases in the likelihood function lead to the emergence of high frequency components related to noise [36, 37]. Consequently, to obtain images with acceptable noise levels, the number of iterations of both MLEM and OSEM has to be limited. One approach to address this limitation is considering the *maximum a posterior* (MAP) criterion, which incorporates prior information through regularisation terms to guide the reconstruction towards a more acceptable solution, i.e., a smoother image.

2.2.2.3 MAP Criterion

The probability of obtaining the activity distribution, $\mathbf{f}$, given the projection data, $\mathbf{g}$, corresponds to the *posterior probability* and can be expressed through Bayes's theorem as:

$$p(\mathbf{f}|\mathbf{g}) = \frac{p(\mathbf{g}|\mathbf{f})\, p(\mathbf{f})}{p(\mathbf{g})} \tag{2.14}$$

where $p(\mathbf{f})$ represents the state of knowledge before the data acquisition, known as the *prior* probability [38]. According to the MAP criterion, the best estimation, $\hat{\mathbf{f}}$, is the one that maximises the posterior probability, as given by equation 2.14, or, equivalently, the one that maximises the logarithm of the posterior probability function, given by:

$$L(\mathbf{f}|\mathbf{g}) \approx L(\mathbf{g}|\mathbf{f}) + ln\, p(\mathbf{f}) \tag{2.15}$$

where the normalization term, $p(\mathbf{g})$, can be neglected, as it is not a function of $\mathbf{f}$ [31, 38]. Considering the Poisson model, $L(\mathbf{f}|\mathbf{g})$ assumes the form:

$$\phi(\mathbf{f}) = L(\mathbf{f}|\mathbf{g}) = \sum_{i=1}^{M} g_i \, ln(\overline{g_i}) \; - \; \overline{g_i} \; - ln(g_i!) \; + \; ln \, p(\mathbf{f}) \tag{2.16}$$

Equation 2.16 combines consistency with the projection data, through the likelihood term, with compliance with prior expectations, through the prior term. This term inserts considerations about the properties the true image should exhibit, such as smoothness. Smoothness can be described as a high probability of neighbouring voxels having similar values. A commonly used prior that encourages this property is given by the Gibbs distribution [32]:

$$p(\mathbf{f}) = \frac{1}{Z} e^{-\beta R(\mathbf{f})} \tag{2.17}$$

where Z represents the normalization partition function, β determines the strenght of the prior, and $R(\mathbf{f})$ is known as an *energy* function of $\mathbf{f}$ [38]. Considering a Gibbs prior, equation 2.15 assumes the following simplified form:

$$L(\mathbf{f}|\mathbf{g}) \approx L(\mathbf{g}|\mathbf{f}) \; - \; \beta R(\mathbf{f}) \tag{2.18}$$

The term $\beta R(\mathbf{f})$ can be interpreted as a *penalty* (or *regularisation*) term. The penalty function, $R(\mathbf{f})$, suppresses large differences between neighbouring voxels, steering the estimate away from the ML solution [37]. As $\beta R(\mathbf{f})$ penalises the likelihood function, MAP-based algorithms are also known as *penalised likelihood* (PL) algorithms. β determines the strength of regularisation to control image noise [39].

Two examples of Gibbs priors are the relative difference prior (RDP) and the median root prior (MRP). The RDP penalises relative differences in value between neighbouring voxels and is given by:

$$R(\mathbf{f}) = \sum_{j} \sum_{k \in N_j} w_{jk} \frac{(f_j - f_k)^2}{(f_j + f_k) + \gamma \, |f_j - f_k|} \tag{2.19}$$

where N_j represents the neighbourhood of voxel j, w_{jk} represents a weighting factor concerning the distance between voxels j and k, and γ is a parameter that controls the shape of the prior [37, 40, 41]. Particularly, γ controls the degree of edge-preservation; the higher its value, the sharper the image. RDP regularisation imposes more smoothing in areas with lower activity and less smoothing in areas with higher activity [42].

The MRP is given by:

$$R(f^k) = \frac{f_i^k - Med(f_i)}{Med(f_i)} \tag{2.20}$$

where $Med(f_i)$ corresponds to the median of the voxels in the neighbourhood of voxel i [43].

2.2.2.4 BSREM

Currently, OSEM is the most widely used iterative reconstruction method, providing superior image quality compared to FBP, while benefiting from low computational costs [31]. However, OSEM is not a globally convergent algorithm: Given any initial image guess, it is not guaranteed that OSEM will converge to the ML solution. One method for making an OS method converge is known as *relaxation*, in which the step size is forced to gradually decrease as the algorithm goes through each subset [44]. In OSEM, the old image estimate for a given subset is multiplied by a given term (equation 2.13) to create the new image estimate. This term can be understood as a *step size*, that is, how much of the old image estimate contributes to the new one. In relaxed OSEM, this term is altered by the introduction of relaxation parameters that diminish the old image estimate contribution [31]. The row-action maximum-likelihood algorithm (RAMALA), introduced by Browne and De Pierro [36], is an example of a relaxed OS method. RAMALA's update equation is given by:

$$f_j^{(k,q)} = f_j^{(k,q-1)} + \eta_k f_j^{(k,q-1)} \sum_{i \in S_q} \left(\frac{P_{ij} g_i}{\sum_l P_{il} f_l^{(k,q-1)} + r_i} - 1 \right) \tag{2.21}$$

where η_k corresponds to a sequence of positive relaxation parameters obeying the following conditions:

$$\lim_{k \to \infty} \eta_k = 0 \; ; \; \sum_{k=0}^{\infty} \eta_k = +\infty \tag{2.22}$$

Browne and De Pierro proved RAMALA's global convergence for a strictly concave objective function. De Pierro and Yamagishi [45] extended this method to the MAP formulation, treating the prior term as another subset of the objective function. The resulting algorithm is known as the block sequential regularised expectation maximisation (BSREM) algorithm. BSREM's global convergence proof required certain *a priori* assumptions and, posteriorly, a modified version of BSREM that allowed for a global convergence proof without those assumptions was introduced by Ahn and Fessler [44]. The BSREM update equation is given by:

$$f_j^{(k,q)} = f_j^{(k,q-1)} + \eta_k f_j^{(k,q-1)} \nabla \phi_q \left(f_j^{(k,q-1)} \right) \tag{2.23}$$

2.2.2.5 Q.Clear

A commercial application of BSREM corresponds to Q.Clear (GE Healthcare). Q.Clear's objective function, following the PL formulation, can be written as [37]:

$$\phi(\mathbf{f}) = \sum_{i=1}^{M} g_i \, log([Pf]_i + r_i) - ([Pf]_i + r_i) - \beta R(\mathbf{f}) \tag{2.24}$$

Q.Clear was first incorporated to GE's PET/CT systems, allowing for reconstructions using RDP regularisation and having β as the only adjustable parameter. Recently, a more flexible version of Q.Clear has been implemented in the StarGuide SPECT/CT system. In StarGuide, Q.Clear can be applied with and without regularisation. It allows for RDP or MRP regularisation, and both γ and β are adjustable parameters. While optimisation of the β parameter has been extensively studied for PET/CT systems, few studies have addressed the performance and the optimisation of Q.Clear in the SPECT domain, particularly due to the novelty of the StarGuide system. Most studies have either used StarGuide's OSEM algorithm [22, 24, 28] or employed Q.Clear with only the reconstruction parameters recommended by the manufacturer, without exploring the algorithm's full capabilities [21, 22, 26].

Danieli et al. [23] conducted the first study of Q.Clear's performance for quantitative ^{177}Lu SPECT/CT, using both a cylindrical phantom and a NEMA IEC Body phantom. An optimisation of the number of iterations and the number of subsets was performed for three reconstruction methods: OSEM, Q.Clear without regularisation and Q.Clear with RDP regularisation. For the latter, γ and β were kept constant. Image quality was evaluated by calculating the spatial resolution (NEMA IEC Body phantom) and the coefficient of variation (cylindrical phantom) as a noise measure. Compared to OSEM, Q.Clear showed reduced noise accumulation and fewer Gibbs-like artefacts as the number of iterations increased. For a fixed number of updates (iterations $\times$ subsets), both image quality parameters were found to depend on the number of subsets. Overall, Q.Clear enabled the quantification of ^{177}Lu, with the quantification accuracy error (cylindrical phantom) not surpassing 10%.

As noted previously, Andelius et al. [27] conducted a comparative study of the StarGuide system's performance relative to conventional gamma camera systems for bone, cardiac and lung scans. An optimisation of the number of iterations, number of subsets, and the γ and β values was performed on a small cohort of patient images for each scan type. Image quality was qualitatively assessed by physicians, and Q.Clear's images were considered to be of similar quality to those obtained with traditional systems.

Recently, Yamaguchi et al. [46] optimised Q.Clear's γ $(1 - 50)$ and β $(0.01 - 0.1)$ parameters for striatal SPECT using the StarGuide system and an ^{123}I-FP-CIT-filled striatum phantom. Increases in β were found to reduce the coefficient of variation of the reconstructed image, while increases in γ improved the image's contrast. A visual evaluation of the images, performed by physicians and technicians, concluded that the combinations $\beta = 0.03$ and $\gamma = 5$, and $\beta = 0.05$ and $\gamma = 10$ produced the images that most accurately described the tracer accumulation in the striatal regions. Similarly, an effort to harmonize acquisition and reconstruction protocols for $[^{123}I]$-Ioflupane imaging using the StarGuide system was conducted by independent research groups across seven European centres [47]. Each group evaluated the StarGuide system, first according to the NEMA NU 1-2018 standards and subsequently through in-house phantom studies. These procedures included variations in Q.Clear's reconstruction parameters, namely the number of iterations and subsets, the γ $(0.2 - 2)$ and β $(0.01 - 0.08)$ values, and post-filtering options. Using clinically relevant quantitative metrics derived from a striatum phantom, optimal reconstruction parameters were identified, leading to consensus across the centres.

2.3. Quantitative SPECT

SPECT has historically been regarded as a non-quantitative nuclear imaging modality, with images being reconstructed in units of counts and image analysis relying mostly on relative radiopharmaceutical uptake, i.e., the comparison of uptake between imaged body structures. In contrast, PET images have traditionally been reconstructed in units of activity concentration and/or standardised uptake value (SUV). The lower spatial resolution, sensitivity and image quality of SPECT, when compared to PET, made the first a less attractive option for absolute quantification. However, recent advancements in SPECT technology have enabled the quantification of SPECT data in a similar manner to PET data. These include improvements in image reconstruction algorithms and correction methods for image-degrading phenomena, such as photon attenuation, scatter, collimator-detector response and the partial volume effect (PVE). The development of quantitative SPECT has been driven by progress in *targeted radionuclide therapy* (TRT) and, particularly, in *theranostics* [48, 49].

In TRT, a radionuclide is attached to a *vector*, a molecule that has an affinity for a specific biological target or receptor, thereby enabling the selective delivery of radiation [50]. In this framework, theranostics has emerged as a precision medicine approach that combines nuclear medicine imaging with TRT [51]. This combination can be achieved using a radionuclide with both diagnostic and therapeutic capabilities; that is, in the SPECT domain, a radionuclide that emits both γ and β radiation, such as ^{177}Lu. The ability to perform SPECT imaging during treatment enables internal dose calculations, verification of treatment delivery, and personalisation of therapy over the course of several sessions [50]. Another theranostic approach involves the use of a *theranostic radionuclide pair*, consisting of a γ-emitting radionuclide (imaging) and a β-emitting radionuclide (therapy), both labelling vectors targetting the same structure [52]. This approach enables, for example, pre- and post-therapeutic imaging to assess and monitor treatment response.

Accurate quantitative SPECT reconstruction requires attenuation and scatter correction, as attenuated and scattered photons degrade image quality and reduce quantitative reconstruction accuracy. In iterative reconstruction methods, the attenuation correction is performed by incorporating an attenuation map of the patient's body into the system matrix [48, 53]. In SPECT/CT, the attenuation map is obtained from the CT scan. To do so, the CT images are converted from Hounsfield units (HU) into corresponding linear attenuation coefficients for the appropriate radionuclide photon energy [54]. To compensate for scatter, *multiple energy window* scatter correction methods are typically used, including the dual-energy-window (DEW) and the triple-energy-window (TEW) methods [48]. In these approaches, scatter windows are used to estimate the number of scattered photons recorded in the photopeak energy window, and these estimate is then subtracted from the photopeak counts to obtain corrected values [55]. In the TEW method, two subwindows are defined: one below the photopeak energy window - *lower scatter window* - and one above the photopeak energy window - *upper scatter window*. The scatter component for a voxel i is estimated as:

$$C_{i,scatter} = \left(\frac{C_{i,lower}}{W_{lower}} + \frac{C_{i,upper}}{W_{upper}} \right) \times \frac{W_{main}}{2} \tag{2.25}$$

where $C_{i,lower}$ and $C_{i,upper}$ are the counts recorded in the lower and upper scatter windows, respectively, and W_{lower}, W_{upper} and W_{main} represent the width of the corresponding energy windows [53, 55]. The TEW method is used for radionuclides with emissions above the photopeak of interest, as these higher energy photons can be scattered and recorded in the main energy window, in a process known as *downscatter*. In contrast, the DEW method considers only a low scatter window [18, 53]. Additionally, *resolution recovery* algorithms are used to correct for the collimator-detector response. The same amount of activity can be viewed differently by a detector due to detector intrinsic response and collimator response, which includes geometric response, scatter, and septal penetration. These components collectively define the collimator-detector response function*, which can be modelled and incorporated into the reconstruction process to compensate for the these effects [56, 57].

The PVE refers to the apparent underestimation or overestimation of the activity within a structure that occurs for structures smaller than 3 times the FWHM of the spatial resolution of the reconstructed images or for structures located at the edge of larger objects, due to a combination of count *spill-out* and *spill-in* effects [53, 58]. The former effect corresponds to the distribution of activity beyond the borders of the structure, causing a loss of signal for that structure and subsequent underestimation of activity. The latter corresponds to the integration of counts within a structure that is surrounded by regions with higher activity, leading to an overestimation of the structure's activity [58]. PVE is due to the SPECT system limited spatial resolution. Although partial volume corrections are not generally available commercially, EANM† guidelines for quantitative SPECT encourage the empirical determination of PVE correction factors, also known as *recovery coefficients* (RCs) [48]. These correspond to the ratio of the apparent (measured) activity concentration to the true concentration and can be applied to correct for the PVE [3]. The determination of RCs, and associated recovery curves, is typically performed using phantoms with spherical inserts, such as the NEMA IEC PET Body Phantom [59], filled with known activity concentrations.

To perform quantitative SPECT, a *calibration factor*, which converts reconstructed image counts into activity concentration units (Bq/ml), must be determined. The calibration factor depends on the chosen radionuclide and on the acquisition, reconstruction, and image correction parameters defined. A commonly used method to determine the calibration factor is to perform volumetric measurements of a large phantom filled uniformly with a known activity concentration [48]. Quantitative SPECT can be applied to patient scans only if the phantoms used are acquired, reconstructed and corrected using the same parameters as those applied in patient imaging [53].

---

*Scatter and septal penetration functions model the interactions between photons and the collimator. The detector intrinsic response function models the effects of interactions within the detector itself, while the collimator response function models the effects of the source-to-collimator distance [56].

†European Association of Nuclear Medicine.

Despite significant technological and methodological advances in SPECT/CT, several limitations remain that hinder its full establishment as a robust quantitative modality. Quantitative accuracy remains heavily dependent on acquisition protocols, reconstruction algorithms, and the selection of their respective parameters, particularly within the context of iterative and penalised-likelihood methods. The lack of standardisation across systems, notably between conventional NaI(Tl) crystal-based cameras and newer systems based on CZT detectors, further complicates the reproducibility and comparability of results. Additionally, although algorithms such as BSREM (Q.Clear) have demonstrated advantages regarding noise control and convergence, their performance in the SPECT domain remains insufficiently characterised. In particular, the impact of fundamental reconstruction parameters, such as γ and β, on image quality, noise behaviour, and quantitative accuracy is not fully understood, especially in 360° geometry CZT systems like the StarGuide. Existing studies are still limited in scope, often based on specific phantoms or small patient cohorts, failing to provide a systematic framework for the optimisation of these parameters. Consequently, there is an evident need for a systematic evaluation and optimisation of reconstruction strategies tailored to CZT-based SPECT/CT systems, with a particular focus on their quantitative performance. Addressing these limitations is essential to ensure reliable activity quantification and to support the clinical implementation of personalised dosimetry approaches in radionuclide therapy.

2.4. Radionuclides

This section provides an overview of the radionuclides used in this study.

2.4.1 ^{99m}Tc

^{99m}Tc is a metastable state of ^{99}Tc. It has a physical half-life of 6.01 hours, emits γ photons with an energy of $140.51\,keV$ (88.5%), and can be easily obtained from a ^{99}Mo-^{99m}Tc generator [60]. These properties have made ^{99m}Tc the most widely used radionuclide for SPECT imaging. Some of its applications include measurements of bone metabolism, myocardial perfusion, and cerebral blood flow, enabling, respectively, the assessment of metastatic spread of cancer, coronary artery disease, and neurological disorders [3].

2.4.2 ^{177}Lu

^{177}Lu has a physical half-life of 6.64 days and decays into the stable radionuclide ^{177}Hf by β^- emission. Consequently, ^{177}Lu can be used for therapeutic purposes. The emitted

β^- particles have a maximum energy of $496.80\,keV$ (79.5%). During the decay process, γ-rays that can be imaged by SPECT are also emitted, with energies of $112.95\,keV$ (6.2%) and 208.37 (10.4%) [61]. Currently, this radionuclide is commonly used for the treatment of metastatic castration-resistant prostate cancer with radiopharmaceutical [^{177}Lu]Lu-PSMA-617, which targets the prostate-specific membrane antigen (PSMA) overexpressed in these tumours, and for inoperable SSTR-positive gastroenteropancreatic neuroendocrine tumours with radiopharmaceutical [^{177}Lu]Lu-DOTATATE, which targets somatostatin receptors (SSTRs) overexpressed in neuroendocrine tumours [62].

2.4.3 ^{123}I

^{123}I has a physical half-life of 13.22 hours and emits γ photons with an energy of $158.97\,keV$ (83.3%) [63]. In addition to the primary photons, ^{123}I emits a series of high-energy photons, between 248 and $784\,keV$, with a total abundance of 3.0% [3]. The most abundant emission occurs at $529\,keV$ (1.4%) and is associated with a backscatter peak at $172\,keV$, which typically falls within the photopeak energy window defined for imaging. Overall, these high energy photons can penetrate the collimator septa and can also be scattered and detected into the photopeak energy window, thereby compromising image quality [51].

It is commonly paired with ^{131}I, which emits β^- particles used for treatment, forming the theranostic pair $^{123}I/^{131}I$. This approach enables pre- and post-therapeutic assessment of differentiated thyroid cancer by SPECT/CT imaging. Additionally, the radiopharmaceutical [^{123}I]-metaiodobenzylguanidine ([^{123}I]-MIBG) is used to identify neuroendocrine tumours that express that express the norepinephrine transporter, which MIBG targets, and that are subsequently treated with [^{131}I]-MIBG [62].

3. Materials and Methods

The primary objective of this study was the optimisation of Q.Clear reconstruction parameters for quantitative ^{123}I, ^{99m}Tc, and ^{177}Lu imaging on the StarGuide SPECT/CT system. To this end, a NEMA IEC PET Body phantom was filled separately with each radionuclide and acquired on both the StarGuide and Symbia Pro.specta SPECT/CT systems. The StarGuide datasets were used to evaluate different Q.Clear reconstruction parameter combinations, whereas the Symbia Pro.specta datasets, reconstructed using the well-established OSEM algorithm, served as a reference for quantitative performance comparison. The reconstructed images were assessed using recovery coefficients, background variability, signal-to-noise ratio, and contrast recovery coefficients. To enable systematic quantitative analysis of the phantom images, dedicated workflows were developed in MIM Software and Python. These tools also enabled the implementation of a method for calibration factor determination directly from NEMA phantom acquisitions. To evaluate this approach, a secondary study was performed using a Jaszczak Deluxe SPECT phantom filled with ^{123}I, allowing comparison with the calibration factor determination methodology recommended by the EANM guidelines. The following sections describe the phantoms used and their preparation, the acquisition and reconstruction procedures, the development of the quantitative analysis tools, and the image quality metrics employed throughout the study.

3.1. Radionuclides

This study focused on three radionuclides, whose characteristics were summarised in chapter 2. Following the installation of the StarGuide SPECT/CT system in the Nuclear Medicine Department at IPO Porto, replacing a conventional Anger camera system, routine clinical examinations began to be performed on this equipment, motivating the need to assess and optimise its quantitative performance. Within this context, as paediatric ^{123}I-MIBG SPECT examinations, which were frequently performed at IPO Porto, were subsequently transferred to the StarGuide system, optimising its performance for this radionuclide became particularly relevant. ^{99m}Tc was included in the study because it is the most widely used radionuclide in SPECT imaging. Although its quantitative performance has been extensively investigated using OSEM reconstruction and conventional Anger camera systems, its behaviour under the novel acquisition geometry and reconstruction framework provided by the StarGuide system remains less well established, warranting further investigation. Finally, ^{177}Lu was included in the study owing to its growing role in theranostics, enabled by its combined beta- and gamma-emitting properties. Its clinical use has expanded considerably, particularly for the treatment of prostate cancer and neuroendocrine tumours [64]. Furthermore, the StarGuide system's ability to simultaneously image both ^{177}Lu photopeaks makes it a promising candidate for quantitative ^{177}Lu imaging, supporting personalised dosimetry and theranostic applications [23].

^{123}I is a particularly challenging radionuclide to image due to the emission of several high-energy photons, which lead to septal penetration and scatter [65]. In turn, these phenomena are known to reduce image contrast and spatial resolution, and to create image artefacts that compromise quantification accuracy [66]. Hence, the use of ME collimators for this radionuclide is often suggested to reduce the influence of the scatter component. However, for studies where high spatial resolution is required, LEHR collimators should be used. In this context, scatter correction methods assume great importance, as there is a large contribution from down-scattered high energy photons in the photopeak window [67]. The challenges associated with the imaging of ^{177}Lu are also related to scatter and septal penetration. In particular, the $113\,keV$ energy window is highly affected by scattered high-energy photons, and the $208\,keV$ photons largely contribute to septal penetration, both of which compromise image quality [66]. Hence, the choice of collimator (ME for the $208\,keV$ peak [66]) and the implementation of scatter and septal penetration correction methods are essential to mitigate these phenomenons and improve image quality.

The clean $140.51\,keV$ gamma emission of ^{99m}Tc, characterised by the absence of primary particle radiation and the low abundance of emissions at other energies, has, together with its wide range of clinical applications, established ^{99m}Tc as the workhorse of SPECT [3, 68]. Consequently, the performance of NaI(Tl) Anger cameras has generally been evaluated using this radionuclide as a reference, establishing well-know benchmarks for energy resolution, spatial resolution and sensitivity. In this domain, CZT cameras have consistently show greater energy resolution (5% at $140\,keV$ compared to 10% for a conventional camera), sensitivity, spatial resolution and shorter acquisition times [1, 69, 70].

The improved energy resolution in CZT detectors can facilitate scatter correction through better discrimination between primary and scattered photons, thereby improving imaging performance for radionuclides such as ^{123}I and ^{177}Lu [70]. However, septal penetration is primarily determined by collimator design (septa thickness and length). Consequently, improvements in the compensation of septal penetration artefacts are expected to arise mainly from dedicated correction models rather than from the CZT technology itself. Additionally, unlike conventional Anger cameras, where different collimators can be selected based on the radionuclide being imaged, systems such as StarGuide have fixed collimators often focused on ^{99m}Tc imaging [24]. As a result, the acquisition setup cannot be changed to adapt to and mitigate septal penetration from high-energy photons, such as the $208\,keV$ emission of ^{177}Lu. Furthermore, CZT detectors are susceptible to charge-sharing effects, leading to the appearance of low-energy tails in the recorded energy spectrum, which can compromise the performance of window-based scatter correction methods for all tested radionuclides [24].

3.2. Phantoms

Two phantoms were used in this study: a NEMA IEC PET Body phantom (Data Spectrum, Durham, North Carolina, USA) and a Jaszczak Deluxe SPECT phantom (Data Spectrum, Durham, North Carolina, USA) (figure 3.1). These will be hereafter referred to as the NEMA phantom and the Jaszczak phantom, respectively. The NEMA phantom served as the primary phantom for reconstruction optimisation, image quality evaluation, and quantitative performance assessment, whereas the Jaszczak phantom was used exclusively for the calibration factor study described in section 3.5.2.

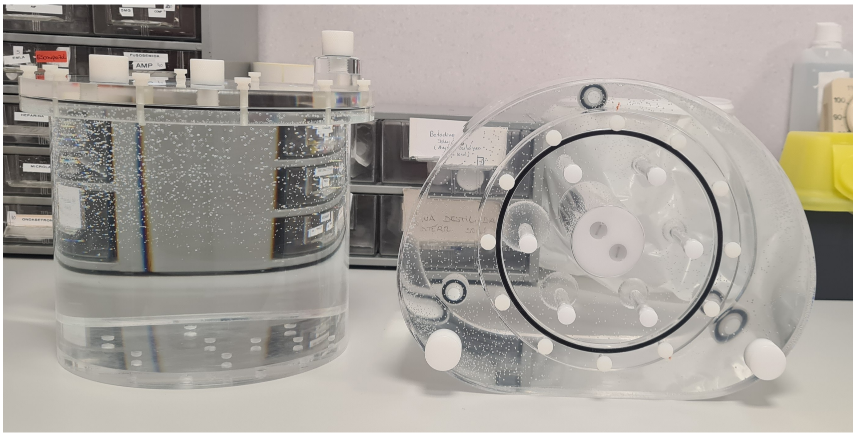

Figure 3.1: Jaszczak phantom (left) and NEMA phantom (right).

3.2.1 NEMA Phantom

The NEMA phantom consists of a main PMMA cylinder, with a nominal volume of approximately $9700\,ml$ when empty, a cylindrical lung insert, with a nominal volume of approximately $260\,ml$, and an insert with six fillable hollow spheres. The spheres have internal diameters of $10, 13, 17, 22, 28$, and $37\,mm$, corresponding, respectively, to fillable volumes of $0.5, 1.2, 2.6, 5.6, 11.5$, and $26.5\,ml$ [59].

The six spheres and the phantom's background compartment (i.e. the remaining fillable volume of the main cylinder with all inserts in place) were filled on separate occasions with dedicated solutions of ^{123}I, ^{99m}Tc, and ^{177}Lu, and subsequently acquired on both the StarGuide and the Symbia Pro.specta (Siemens Healthineers, Erlangen, Germany) SPECT/CT systems. The activity concentrations at the time of acquisition for both the spheres - $c_{spheres}$ - and the background - $c_{background}$, for each acquisition, are presented in table 3.1. For simplicity, each acquisition was assigned a unique identifier (ID), encoding the SPECT/CT system (StarGuide or Symbia Pro.specta) used and the imaged radionuclide (^{123}I, ^{99m}Tc or ^{177}Lu). To distinguish between different acquisitions performed on the same SPECT/CT system for the same radionuclide, a sequential number (from 1 to the total number of acquisitions) was appended to the ID. The values presented in table 3.1 correspond to the time-decay-corrected initial activity concentrations used to fill the referred compartments of the NEMA phantom, as the acquisitions did not immediately follow phantom preparation. This correction is given by:

$$c_{acq.} = c_{prep.} \times e^{-\frac{ln(2)\Delta t}{T_{1/2}}} \tag{3.1}$$

where $c_{prep.}$ is the activity concentration at the time of phantom filling, $c_{acq.}$ is the activity concentration at the time of phantom acquisition, Δt is the time interval between phantom acquisition and phantom preparation, and $T_{1/2}$ is the physical half-life of the considered radionuclide.

As shown in table 3.1, multiple acquisitions with different time durations for the same radionuclide were performed throughout the course of this study. Acquisitions ^{123}I_StarGuide_1 and ^{123}I_Symbia_1 were available at IPO Porto at the beginning of this study, having been performed on 29/10/2025. These datasets and corresponding reconstructions were used, as detailed in sections 3.4 and 3.5, to conduct the optimisation of Q.Clear's reconstruction parameters for ^{123}I and to develop software tools for the quantitative analysis of NEMA phantom images, respectively. The remaining ^{123}I acquisitions were performed on 24/03/2026 to evaluate the determination of the calibration factor using the developed software tools, as further detailed in section 3.5. Once the optimisation for this radionuclide was completed, the phantom was filled with ^{99m}Tc and acquired for 5

*Sphere-to-background activity concentration ratio.

ID	Acquisition Time [min]	$c_{spheres}$ $[MBq/ml]$	$c_{background}$ $[MBq/ml]$	SBR*
^{123}I_StarGuide_1	15	0.068	0.0067	10
^{123}I_StarGuide_2	15	0.169	0.0157	11
^{123}I_StarGuide_3	10	0.166	0.0154	11
^{123}I_StarGuide_4	5	0.163	0.0151	11
^{123}I_Symbia_1	15	0.053	0.0053	10
^{99m}Tc_StarGuide_1	15	0.736	0.068	11
^{99m}Tc_StarGuide_2	5	0.762	0.071	11
^{99m}Tc_Symbia_1	15	0.695	0.064	11
^{99m}Tc_Symbia_2	15	0.673	0.062	11
^{177}Lu_StarGuide_1	15	0.726	0.078	9
^{177}Lu_StarGuide_2	5	0.725	0.078	9
^{177}Lu_StarGuide_3	15	0.318	0.034	9
^{177}Lu_Symbia_1	15	0.591	0.0064	9
^{177}Lu_Symbia_2	5	0.590	0.0064	9

Table 3.1: Activity concentrations, at the time of image acquisition, used for the spheres and the background of the NEMA phantom.

and 15 minutes on both SPECT/CT systems to perform the optimisation for this radionuclide on 12/05/2026. The same procedure was conducted on 20/05/2026 (StarGuide) and 22/05/2026 (Symbia Pro.specta) for ^{177}Lu. This ensured that quantitative performance could be compared between systems and between different acquisition times.

At this stage of the study, images were routinely reconstructed immediately after phantom acquisition, and quantitative analysis, as described in section 3.5, was performed typically on the same day, allowing for repetition of acquisitions when deemed necessary. For the ^{177}Lu-filled phantom, on 27/05/2026, both StarGuide acquisitions were repeated due to a suspected dataset mix-up between the ^{177}Lu_StarGuide_1 and ^{177}Lu_StarGuide_2 datasets, prompted by unexpectedly high recovery coefficients obtained for the 5-minute images, when compared to the 15-minutes images, obtained for the reconstruction protocols tested the previous day. Due to a technical malfunction in the StarGuide system, no scatter windows were acquired for the new 15-minute acquisition, requiring the acquisition to be repeated the following day (^{177}Lu_StarGuide_3). Subsequent evaluation of additional reconstruction protocols confirmed that no dataset mix-up had occurred. Consequently, the acquisitions performed on 27/05/2026 will not be considered in this study; however, since the optimisation procedure for this radionuclide also used data from acquisition ^{177}Lu_StarGuide_3, this acquisition was included in table 3.1.

3.2.1.1 Phantom Preparation

The preparation of the NEMA phantom was identical for each radionuclide studied. First, based on phantom preparation data from previous studies involving the NEMA phantom conducted at IPO Porto, two activity values were established: one for the spheres and another for the background, aiming for a final sphere-to-background activity concentration ratio of approximately 10. Subsequently, using two syringes, the calculated activities were withdrawn from the vials available in IPO Porto's radiopharmacy hot cell, where the radionuclides are stored. After withdrawal, each syringe was placed in a dedicated holder and inserted into the hot cell's dose calibrator, where the activity was measured, with the measured value and the time of measurement being recorded for time-decay correction purposes.

To fill the spheres, the corresponding withdrawn activity was diluted in a vial with $200\,ml$ of water. The spheres were then filled one by one using a syringe, taking care to avoid the formation of air bubbles inside the spheres. The syringe used to transfer the activity to the $200\,ml$ water vial was rinsed repeatedly with the vial's water to minimise residual activity in the syringe.

The background compartment was filled with water almost to the top of the phantom, after which the activity prepared for this region was injected, and the phantom was then topped off with water. The previously described rinsing procedure was also applied to the syringe used to transfer the activity to the background compartment. The NEMA phantom was vigorously shaken to ensure a homogeneous distribution of activity within the phantom's background.

During the preparation of the ^{177}Lu-filled NEMA phantom, after the injection of the activities into the vial and the background compartment, each syringe was once again placed in the dose calibrator to measure its residual activity. This was done because ^{177}Lu has a tendency to precipitate and adhere to surfaces [23]. The time-corrected residual activity was then subtracted from the also time-corrected withdrawn activity to obtain the total prepared activity for each compartment.

3.2.2 Jaszczak Phantom

The Jaszczak phantom consists of a main PMMA cylinder, with a nominal volume of approximately $6900\,ml$ when empty. It includes an insert with cold rods and an insert with six fillable hollow spheres [71]. For the purposes of this study, the phantom was used without any inserts.

The phantom was filled with an ^{123}I solution at an initial activity concentration of $0.0083\ MBq/ml$. It was subsequently acquired three separate times on the StarGuide SPECT/CT system during 5, 10, and 15 minutes, respectively, on 24/03/2026. As the acquisitions did not immediately follow the phantom filling, the correction described by equation 3.1 was also applied to determine the activity concentration at the time of each acquisition. Accordingly, the activity concentrations at the time of acquisition were 0.0066, 0.0065, and $0.0064\ MBq/ml$, respectively. The filling process was identical to that used for the background compartment of the NEMA phantom. These acquisitions were used to, as further detailed in section 3.5, determine calibration factors following the EANM guidelines.

3.3. Image Acquisition

The NEMA phantom was acquired on both the StarGuide SPECT/CT and Symbia Pro.specta SPECT/CT systems. The Jaszczak phantom was acquired exclusively on StarGuide, in accordance with the objectives of this study. The StarGuide SPECT/CT system has been described in detail in section 2.1 of chapter 2. The Symbia Pro.specta SPECT/CT is a conventional dual-head crystal-based SPECT/CT system, equipped with a scintillation crystal with a thickness of $3/8''$. The data collection setup for the NEMA phantom on both systems is presented in figures 3.2, 3.3 and 3.4.

The acquisition process differs considerably between the two SPECT/CT systems considered, owing to the differences in their acquisition geometry. In StarGuide, a scout scan using infrared diodes is first conducted. Using the data from this optical scout, the detectors' radial position is adjusted to be as close as possible to the phantom (figure 3.3) in order to maximise photon detection efficiency. Once this optimal position is achieved, data acquisition begins. During this process, the tip of each detector performs a sweeping motion, acquiring data in $2°$ sweep steps, in a process defined by the system as *continuous sweep mode*. This procedure is repeated for a predefined number of gantry positions/rotations. In this study, six gantry rotations were used for all acquisitions, regardless of the scan duration, according to the acquisition protocols established at IPO Porto. Between gantry positions, the twelve detectors collectively recoil, rotate $5°$ in the clockwise direction and then move radially inward again toward the phantom to continue acquisition. These transitions are scheduled by the system based on the total acquisition time defined by the user. Consequently, the raw acquisition dataset consists of twelve sub-datasets, each containing the data from all gantry positions and sweep steps for each detector.

Figure 3.2: StarGuide setup for the acquisition of the NEMA phantom (left) and a close-up view of the NEMA phantom positioned inside the scanner bore (right).

Figure 3.3: Positioning of the StarGuide detectors during data acquisition.

In Symbia Pro.specta, a topogram is first acquired using lower tube voltage and current than those used for the CT scan. Each detector covers a 180° arc around the phantom in the counter-clockwise direction and acquires a predefined number of views for each angular position. In this study, continuous acquisition mode was selected, and a non-circular orbit was followed by the detector heads. For both systems, the CT scans are conducted prior to the SPECT scans.

Figure 3.4: Symbia Pro.specta setup for the acquisition of the NEMA phantom.

3.3.1 StarGuide SPECT/CT

The energy window settings used for each acquisition are summarised in table 3.2. As already stated, the StarGuide SPECT/CT system is equipped with dual-channel LEHR collimators, enabling the imaging of both ^{177}Lu photopeaks. Consequently, for the ^{177}Lu acquisitions, two main photopeak energy windows were defined - one for each photopeak -, enabling the generation of, in addition to the individual $113\,keV$ and to the $208\,keV$ images, a third image corresponding to the voxel-wise arithmetic sum of the images reconstructed from the both energy windows [21]. In the StarGuide system, the SPECT reconstruction

Radionuclide	Window Center [keV]	Window Width
^{123}I	159.00	10%
^{99m}Tc	140.51	7.5%
^{177}Lu	113.00	10%
	208.00	6%

Table 3.2: Energy window settings used for acquisitions on the StarGuide system.

image matrix size is automatically defined by the system, whereas the voxel size is defined by the user, with two available options: $2.46 \times 2.46 \times 2.46\,mm^3$ and $4.92 \times 4.92 \times 4.92\,mm^3$. In this study, this parameter was kept constant at $2.46 \times 2.46 \times 2.46\,mm^3$ for all acquisitions. For acquisition ^{123}I_StarGuide_1, a image matrix of size 124×124 was considered, whereas the remaining ^{123}I acquisitions were reconstructed using a 252×252 matrix. All ^{99m}Tc acquisitions were reconstructed using a 252×252 matrix. A reconstruction matrix of size 268×268 was used for acquisitions ^{177}Lu_StarGuide_1 and ^{177}Lu_StarGuide_2, whereas a matrix of size 258×258 was used for acquisition ^{177}Lu_StarGuide_3.

Regarding the CT scans, a tube voltage of $120\,kV$ and a tube current of $60\,mA$ were used for all acquisitions except ^{123}I_StarGuide_1. For acquisition ^{123}I_StarGuide_1, a tube voltage of $80\,kV$ and a tube current of $70\,mA$ were used. The lower tube voltage employed for this acquisition reflects the use of a paediatric MIBG imaging protocol, as described in section 3.1.

The ^{123}I-filled Jaszczak phantom was acquired using the same energy window settings as those defined in table 3.2 for the NEMA phantom acquisitions. The image matrix size used was 238×238 and the reconstructed voxel size used was $2.46 \times 2.46 \times 2.46\,mm^3$. For the CT scan, a tube voltage of $120\,kV$ and a tube current of $60\,mA$ were used. These acquisition settings were identical to those used for acquisitions ^{123}I_StarGuide_2 to ^{123}I_StarGuide_4, as these scans were performed to compare two methods for determining calibration factors, as previously stated.

3.3.2 Symbia Pro.specta SPECT/CT

The ^{123}I and ^{99m}Tc NEMA phantom acquisitions were performed using LEHR collimators on each detector head of the Symbia Pro.specta SPECT/CT system. For ^{177}Lu, a MELP* collimator was used, as recommended by the MIRD/EANM guidelines for imaging the $208\,keV$ photopeak, due to the lower septal penetration of the MELP collimator [66]. The energy window settings used for each acquisition are summarised in table 3.3. The number of views per detector head and the time per view used for each acquisition are summarised in table 3.4.

Radionuclide	Window Center [keV]	Window Width
^{123}I	159.00	15%
^{99m}Tc	140.51	15%
^{177}Lu	208.00	20%

Table 3.3: Energy window settings used for acquisitions on the Symbia Pro.specta system.

For both ^{99m}Tc and ^{177}Lu acquisitions, an image matrix size of 128×128 and a voxel size of $4.80 \times 4.80 \times 3.00\,mm^3$ were used. For the ^{123}I acquisitions, the same matrix size was

*Medium Energy Low Penetration.

ID	Number of Views	Time per View [s]	Acquisition Time [s]
^{123}I_Symbia_1	60	15	900
^{99m}Tc_Symbia_1	60	15	900
^{99m}Tc_Symbia_2	60	5	300
^{177}Lu_Symbia_1	60	15	900
^{177}Lu_Symbia_2	60	5	300

Table 3.4: Symbia Pro.specta - acquisition settings used for each acquisition.

used, while the reconstructed voxel size was $2.34 \times 2.34 \times 3.00\,mm^3$. Regarding the CT scans, a $110\,kV$ tube voltage and tube currents of 50, 60, and $13\,mA$ were used for the $^{99m}\mathrm{Tc}$, $^{177}\mathrm{Lu}$ and $^{123}\mathrm{I}$ acquisitions, respectively, following the application of the acquisition protocols currently used at IPO Porto for each radionuclide.

3.4. Image Reconstruction

3.4.1 StarGuide SPECT/CT

The StarGuide SPECT/CT system features an integrated web-based reconstruction platform, SmartConsole, which supports two reconstruction algorithms: OSEM and Q.Clear. In this study, StarGuide images were reconstructed using Q.Clear with RDP regularisation. When Q.Clear is selected as the reconstruction algorithm in SmartConsole, a panel displaying all available reconstruction settings is presented to the user. Through this panel, the user can control:

- The number of iterations.
- The number of subsets.
- The values of the regularisation parameters, β and γ.
- The implementation of corrections for image-degrading phenomena. In this case, attenuation correction and scatter correction can be selected.
- The use of tail photons in the reconstruction process by activating the *Use Tail* option.
- The application of post-reconstruction filters.
- The use of the By Sens tool and Clarify DL.

Regarding post-reconstruction processing, SmartConsole supports the application of Butterworth, Hann, and Gaussian smoothing filters. Filters such as those mentioned above are applied in the frequency domain of the data [72]. Butterworth and Hann filters are low-pass filters that suppress high-frequency components while preserving low-frequency information. The Butterworth filter is characterised by two parameters: the critical frequency, above which the filter response begins to decrease towards zero, and the power, which determines the steepness of this roll-off. The Hann filter defines a frequency window in which low frequencies are preserved with minimal attenuation, while the response gradually decreases towards zero as the cut-off frequency is approached. The Gaussian filter uses a Gaussian kernel to smooth the image and is characterised by the FWHM in the transverse and axial directions [25, 72].

Additionally, SmartConsole allows the application of GE Healthcare's edge-preservation filter, known as Clarity 3D (C3D). This filter is described by GE Healthcare as an edge-preserving filter with noise adaptation. The user can select the filter's power and may also activate a contrast enhancement option, which was not used in this study [25].

SmartConsole also allows the activation of the By Sens tool. When this tool is used, the value of β is weighted according to a sensitivity map derived from the CT-based attenuation map of the examination being performed [23, 25].

Attenuation correction is applied using the CT-derived attenuation map. Scatter correction, when selected, is performed using either the DEW or the TEW method. For the radionuclides considered in this study, the defined scatter windows are presented in table 3.5.

Radionuclide	Lower Scatter Window [keV]	Upper Scatter Window [keV]
^{123}I	$131.00 \pm 9\%$	-
^{99m}Tc	$114.00 \pm 10\%$	-
^{177}Lu - $113\,keV$	$93.50 \pm 11\%$	$133.00 \pm 8\%$
^{177}Lu - $208\,keV$	$182.70 \pm 10\%$	-

Table 3.5: StarGuide - scatter energy windows used for scatter correction.

Although not explored in this study, SmartConsole includes a deep-learning reconstruction tool for bone SPECT imaging named Clarify DL. Clarify DL is a deep learning-based reconstruction method that is available in SmartConsole in addition to the existing reconstruction algorithm (in this case, Q.Clear). The model is applied to reconstructed images at fixed intervals between image updates, with the interval defined by the user. At each interval, the model generates a noise-reduced image, which is then blended with the current reconstructed image. The blended image is subsequently used to continue the iterative reconstruction process [73].

SmartConsole also allows the user to visualise acquisition data in list-mode. In list-mode, the attributes of individual events, such as the energy deposited in the detectors, detector position and angle, and other event-specific information, are stored together with the time at which each event was recorded [74]. This enables post-acquisition reframing of the acquired data, allowing multiple datasets with different acquisition durations to be generated from a single acquisition.

In the following sections, the optimisation procedures performed for each radionuclide on the StarGuide system are detailed.

3.4.1.1 ^{123}I

Due to the availability of NEMA phantom data for ^{123}I at IPO Porto at the beginning of this study (acquisition dataset ^{123}I_StarGuide_1), this radionuclide was chosen for the first optimisation approach. As, at the time, there were no reconstruction parameters reported in the literature for this radionuclide, this optimisation process was based on the reconstructions already available in the IPO Porto database. As the novelty of Q.Clear, relative to OSEM, lies precisely in the regularisation parameters β and γ, it was decided that all other reconstruction parameters would be kept constant in order to evaluate the impact of regularisation on quantitative accuracy, noise, and overall image quality. The number of iterations was kept at 40 and the number of subsets at 10, as these were the values typically used in the reconstruction protocols currently employed at IPO Porto for ^{123}I imaging. The β values considered were 0.01, 0.05, 0.1, 0.5, and 1, while the γ values considered were 0.1, 0.5, 1, and 3, resulting in a total of 20 distinct combinations of reconstruction parameters (table 3.6). All images were subjected to attenuation and scatter correction,

	$\beta = 0.01$	$\beta = 0.05$	$\beta = 0.1$	$\beta = 0.5$	$\beta = 1$
$\gamma = 0.1$	$^{123}I\_R1$	$^{123}I\_R2$	$^{123}I\_R3$	$^{123}I\_R4$	$^{123}I\_R5$
$\gamma = 0.5$	$^{123}I\_R6$	$^{123}I\_R7$	$^{123}I\_R8$	$^{123}I\_R9$	$^{123}I\_R10$
$\gamma = 1$	$^{123}I\_R11$	$^{123}I\_R12$	$^{123}I\_R13$	$^{123}I\_R14$	$^{123}I\_R15$
$\gamma = 3$	$^{123}I\_R16$	$^{123}I\_R17$	$^{123}I\_R18$	$^{123}I\_R19$	$^{123}I\_R20$

Table 3.6: Combinations of β and γ used for the reconstruction of the ^{123}I images.

and tail photons were included in the reconstruction process. The edge-preservation filter Clarity 3D was applied with a power of 0.01. The By Sens tool was also used. These parameters were employed because they were used in the basis reconstruction protocol for which β and γ were varied, which corresponded to the reconstruction protocol currently used at IPO Porto for MIBG examinations.

It is relevant to note that this first optimisation study allowed informed decisions to be made during the optimisation of Q.Clear for ^{99m}Tc and ^{177}Lu, as the impact of varying β and γ was already known. As such, the procedure followed for these radionuclides was as follows: first, protocols used at IPO Porto and protocols reported in the literature were tested. The resulting images were then analysed using the tools and procedures described in section 3.5. Based on this analysis, the optimal reconstruction protocol was identified, and efforts were made to improve the analysed image quality metrics through the fine-tuning of the optimal protocol parameters, resulting in the development of additional reconstruction protocols.

3.4.1.2 ^{99m}Tc

The reconstruction protocols tested are summarised in table 3.7. The protocols are organised in chronological order of their application and/or conception. First, four reconstruction protocols ($^{99m}Tc\_R1$ to $^{99m}Tc\_R4$) were tested. Protocols $^{99m}Tc\_R1$ and $^{99m}Tc_R2$ are presets available on SmartConsole and defined by GE Healthcare, known respectively as *NEMA Resolution* and *Bone Torso*. The first set of reconstruction settings corresponds to a manufacturer protocol that can be used for the reconstruction of images involving point sources for the calculation of spatial resolution [22]. The second set of reconstruction settings is also a manufacturer protocol that had been used at IPO Porto for bone SPECT scans. As this protocol does not include scatter correction, a third protocol with identical parameters but including scatter correction was also tested. This protocol was also used by Zorz et al. [22] for the reconstruction of images of a similar NEMA phantom filled with ^{99m}Tc. Finally, another reconstruction protocol used at IPO Porto was tested, protocol $^{99m}Tc\_R4$, known as *General Tomo*.

At this stage, to evaluate whether reframing the 15-minute acquisition into a 5-minute dataset using list-mode resulted in performance comparable to that of a true 5-minute acquisition, the *Lister* menu in SmartConsole was accessed for acquisition $^{99m}Tc\_StarGuide\_1$, and a reframe into a 5-minute dataset was performed for reconstruction protocols $^{99m}Tc\_R2$ and $^{99m}Tc\_R3$.

Following the quantitative analysis, protocol $^{99m}Tc\_R4$ was selected for further fine-tuning, as it generally presented higher recovery coefficients. At this stage, two actions were considered. First, two additional β values, 0.05 and 0.1, were tested while keeping all other reconstruction parameters unchanged. The choice of higher β values was based on the analysis previously conducted for ^{123}I, which demonstrated that increasing this parameter leads to an improvement in image signal-to-noise ratio, a desirable outcome in this case (protocols $^{99m}Tc\_R5$ and $^{99m}Tc\_R6$).

Additionally, the impact of the By Sens tool was evaluated, as this tool had not been investigated previously* and was included in protocol $^{99m}Tc\_R4$, which was currently used at IPO Porto. For this purpose, protocols $^{99m}Tc\_R4$ to $^{99m}Tc\_R6$ were repeated with identical reconstruction parameters but with the By Sens tool disabled, resulting in protocols $^{99m}Tc\_R7$ to $^{99m}Tc\_R9$. Attenuation correction was always applied and no post-reconstruction filters were used.

Protocol	Iterations	Subsets	γ	β	C3D	SC†	By Sens
$^{99m}Tc\_R1$	10	8	2	0.0125	0.01	No	OFF
$^{99m}Tc\_R2$	10	10	2	1	No	No	OFF
$^{99m}Tc\_R3$	10	10	2	1	No	Yes	OFF
$^{99m}Tc\_R4$	10	10	1.5	0.02	0.01	No	ON
$^{99m}Tc\_R5$	10	10	1.5	0.05	0.01	No	ON
$^{99m}Tc\_R6$	10	10	1.5	0.1	0.01	No	ON
$^{99m}Tc\_R7$	10	10	1.5	0.02	0.01	No	OFF
$^{99m}Tc\_R8$	10	10	1.5	0.05	0.01	No	OFF
$^{99m}Tc\_R9$	10	10	1.5	0.1	0.01	No	OFF

Table 3.7: ^{99m}Tc StarGuide reconstruction protocols.

3.4.1.3 ^{177}Lu

The reconstruction protocols tested are presented in table 3.8. Using the acquisition datasets ^{177}Lu_StarGuide_1 and ^{177}Lu_StarGuide_2, four reconstruction protocols were initially put to test (protocols $^{177}Lu\_R1$ to $^{177}Lu\_R4$). The first one corresponded to the optimised reconstruction protocol obtained by Danieli et al. in their ^{177}Lu quantitative

*Although the tool was used for ^{123}I reconstructions, no comparison between its use and non-use was performed; ^{99m}Tc was therefore used for this evaluation.

†Scatter Correction.

imaging study using a NEMA phantom [23]. In this same study, the authors used a factory-recommended protocol for comparison purposes, which was recreated in protocol $^{177}Lu\_R2$. Protocol $^{177}Lu\_R3$ recreated the parameters used by Hoog et al. [21] for ^{177}Lu imaging on StarGuide, in their performance study of this equipment, using a customised NEMA phantom. Finally, protocol $^{177}Lu\_R4$ is the one used at IPO Porto for ^{177}Lu patient examinations. As shown in table 3.8, these reconstruction protocols establish parameters for two energy windows: one centred on the $113\,keV$ peak and the other on the $208\,keV$ peak. Both images can be reconstructed on the SmartConsole with a third image, corresponding to voxel-wise average of these two also being created. In the first stage of this optimisation procedure, only the averaged image was considered for quantitative analysis.

From the quantitative analysis, it was noticed that protocol $^{177}Lu\_R2$ presented, overall, the highest recovery coefficients for the four smaller spheres, while protocol $^{177}Lu\_R4$ presented the highest recovery coefficients for the two biggest spheres (15-minute dataset). Consequently, a closer look was taken upon this protocols, with the $113\,keV$ and $208\,keV$ images being analysed for each protocol. From this analysis, it was noticed that, for the mentioned spheres for each protocol, images $113\,keV$ and $208\,keV$ performed better, in terms of recovery coefficients, for protocols $^{177}Lu\_R2$ and $^{177}Lu\_R4$, respectively. As such, a combined protocol was proposed - $^{177}Lu\_R5$ - using the settings of protocol $^{177}Lu\_R2$ for the $113\,keV$ energy window and the settings of protocol $^{177}Lu\_R4$ for the $208\,keV$ energy window. This combined protocol was applied to the acquisition dataset ^{177}Lu_StarGuide_3.

As this combined protocol presented the best performance in terms of recovery coefficients but low signal-to-noise ratio values, an attempt to improve this last metric was conducted, focusing on the $113\,keV$ energy window, as this was the energy window for which this metric was the lowest. Consequently, four additional protocols were tested, considering the following alterations to the $113\,keV$ window: two other higher β values were considered - 0.2 and 0.3, as, at the time, it was known that increases in β would improve this metric (protocols $^{177}Lu\_R6$ and $^{177}Lu\_R7$). Additionally, another protocol (protocol $^{177}Lu\_R8$), with a reduced number of iterations (10), was also tested, as reducing the number of iterations in a iterative reconstruction method should, by nature, lead to a decrease in image noise [36, 37]. For these protocols, the edge-preservation filter Clarity 3D was used with a power of 0.01, to match the $208\,keV$ energy window. Additionally, to see the influence of Clarity 3D, the combined protocol was repeated with equal parameters

Protocol	Peak	Iterations	Subsets	γ	β	C3D	By SENS
$^{177}Lu\_R1$	113 keV	12	16	1	0.005	No	OFF
	208 keV	12	16	1	0.005	No	OFF
$^{177}Lu\_R2$	113 keV	20	10	1	0.08	No	ON
	208 keV	20	10	1	0.08	No	ON
$^{177}Lu\_R3$	113 keV	30	10	1	0.3	0.01	OFF
	208 keV	20	10	1	0.008	0.01	OFF
$^{177}Lu\_R4$	113 keV	8	10	1	0.3	0.01	ON
	208 keV	8	10	1	0.02	0.01	ON
$^{177}Lu\_R5$	113 keV	20	10	1	0.08	No	ON
	208 keV	8	10	1	0.02	0.01	ON
$^{177}Lu\_R6$	113 keV	20	10	1	0.2	0.01	ON
	208 keV	8	10	1	0.02	0.01	ON
$^{177}Lu\_R7$	113 keV	20	10	1	0.3	0.01	ON
	208 keV	8	10	1	0.02	0.01	ON
$^{177}Lu\_R8$	113 keV	10	10	1	0.08	0.01	ON
	208 keV	8	10	1	0.02	0.01	ON
$^{177}Lu\_R9$	113 keV	20	10	1	0.08	0.01	ON
	208 keV	8	10	1	0.02	0.01	ON

Table 3.8: ^{177}Lu StarGuide reconstruction protocols.

but using Clarity 3D with a power of 0.01 for the $113\,keV$ energy window ($^{177}Lu\_R9$).

All protocols considered attenuation and scatter correction.

3.4.1.4 Jaszczak Phantom

The Jaszczak phantom acquisition data were reconstructed using protocol $^{123}I\_R13$, similarly to the NEMA phantom data (acquisitions ^{123}I_StarGuide_2 to ^{123}I_StarGuide_4) acquired for the calibration factor study. This protocol was chosen because the quantitative analysis deemed it to be one of the optimal reconstruction protocols for ^{123}I imaging.

3.4.2 Symbia Pro.specta SPECT/CT

In the Symbia Pro.specta reconstruction station, the user can define the number of iterations, the number of subsets, the corrections for image-degrading phenomena, and the application of post-processing filters. Attenuation and scatter correction were applied using the same methods as in the StarGuide system. The scatter windows used for each radionuclide are presented in table 3.9.

Radionuclide	Lower Scatter Window [keV]	Upper Scatter Window [keV]
^{123}I	$123.125 \pm 15\%$	$182.816 \pm 15\%$
^{99m}Tc	$119.434 \pm 15\%$	-
^{177}Lu	$177.111 \pm 10\%$	$239.621 \pm 10\%$

Table 3.9: Symbia Pro.specta - scatter energy windows used for scatter correction.

For Symbia Pro.specta images, the manufacturer's OSEM reconstruction algorithm was used and the reconstruction settings were the ones routinely used at IPO Porto for each given radionuclide (table 3.10). All images were subjected to a Gaussian smoothing filter, as defined in IPO Porto clinical reconstruction protocols, characterised by the FWHM. All images were subjected to attenuation correction based on the attenuation map derived from the CT scans and to scatter correction, using the scatter energy windows presented in table 3.9, was also applied.

Radionuclide	Iterations	Subsets	FWHM [mm]
^{123}I	18	4	10
^{99m}Tc	24	4	10
^{177}Lu	12	8	4

Table 3.10: Reconstruction parameters used for Symbia Pro.specta images for every radionuclide.

3.5. Image Analysis

Image analysis was performed using MIM Software (GE Healthcare, version 7.3.4) and Python (version 3.14). First, two quantitative analysis workflows were developed in MIM: one to facilitate and accelerate the quantification of NEMA phantom images, and another to enable rapid determination of background variability across different VOI volumes. Second, using the data generated by these workflows, Python was used to determine recovery coefficients, background variability, signal-to-noise ratio and percentage contrast recovery coefficients of the NEMA images. These metrics were used to quantitively assess all reconstructed images during the optimisation procedures and to compare the quantitative performance of the SPECT systems under study. Finally, Jaszczak phantom images were used in MIM to establish calibration factors, which were then compared with those obtained from NEMA phantom images using an alternative method.

3.5.1 MIM Software

3.5.1.1 NEMA Phantom

The *QC - NEMA Phantom* workflow, available in MIM Software, was developed to accelerate the analysis of reconstructed images of the NEMA phantom. To use this workflow, the user must select a CT scan and a SPECT scan of the phantom. After selecting the corresponding images and launching the workflow, the user is prompted to place a VOI template on the SPECT scan. This template consists of a contour of the body of the NEMA phantom (i.e. the main cylinder), six spheres corresponding to the spherical inserts of the phantom, and twelve additional spheres to be placed in the phantom's background. For simplicity, the first group of spheres will, subsequently, be referred to as the NEMA spheres. After confirming the placement of the VOI template, the user can individually adjust each sphere to better match the SPECT scan. Once the placement of all structures is finalised and confirmed, the software generates six additional VOIs, corresponding to the application of a 50% count threshold to each NEMA sphere VOI. When this process is completed, a table containing statistical information on the counts of each VOI is displayed. In this study, the described workflow was adapted to enable conversion from counts to activity concentration $\left(Bq/Ml\right)$, allowing statistical data to be presented and stored in this format without the need for a separate software tool.

Two new VOI templates were created to replace the original workflow template: the NEMA spheres template and the background spheres template. The NEMA spheres template consists of a contour of the main cylinder, which facilitates template positioning, and six spheres matching the spherical inserts (figure 3.5A). These spheres were drawn to match the internal diameters of the NEMA spheres using the CT axial slice where they appeared to be the widest. The vertical positioning of the spheres within the phantom was further verified using the coronal and sagittal views. The background template consists of a contour of the main cylinder, ten spheres with a volume of $51.0\,ml$, and six additional spheres identical to the NEMA spheres. The ten spheres were evenly distributed within the background region of the phantom, using the CT scan for guidance, and positioned away from both the spherical inserts and the phantom walls (figure 3.5C). The remaining six spheres were placed adjacent to each corresponding NEMA sphere, in the same plane used to define the NEMA spheres (figure 3.5B). For simplicity the ten spheres are hereafter referred to as the background spheres, while the remaining spheres in the background template are referred to as the clone spheres. The clone spheres, matching the volume of the NEMA spheres, were placed in the background region to estimate the background contribution within an equivalent volume for each NEMA sphere.

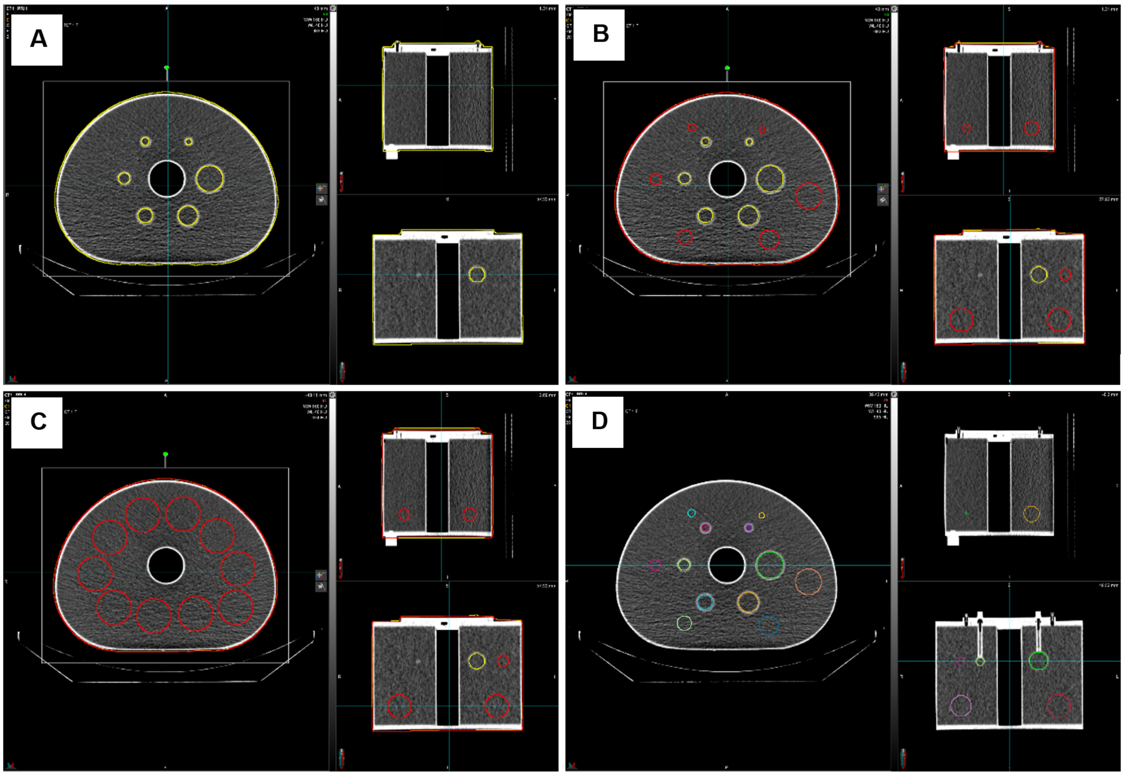

Figure 3.5: VOI templates used in the developed workflow: NEMA spheres template (A), background spheres template composed of the clone spheres (B), and the ten spheres used to determine the calibration factor (C). Panel (D) shows both templates after confirming sphere positioning and making individual adjustments to better match the CT scan.

As two SPECT/CT systems were studied and three radionuclides were used, the procedure described above was repeated for each system-radionuclide combination, since the CT scan differs for each case. Consequently, six separate workflows were generated.

The replacement of the original VOI template with the two new ones allowed more information to be extracted from the same SPECT scan, in counts. To convert the SPECT scan units from counts to activity concentration (Bq/ml), MIM's conversion algorithm, *Z-Launch Convert to Bq/ml*, was integrated into the workflow. The unit conversation operation, from counts, C, to activity concentration, AC, is given by:

$$AC = \frac{C}{T \times V \times CF} \tag{3.2}$$

where T is the acquisition time, V is the reconstructed voxel volume and CF is the calibration factor. V is automatically retrieved by MIM from the DICOM header of the SPECT scan. The acquisition time can also be automatically extracted from the DICOM header and is computed as:

$$T = N_{FR} \times T_F \times N_D \tag{3.3}$$

where N_{FR} is the number of frames in rotation, T_F is the actual frame duration and N_D is the number of detectors. This expression is only valid for Symbia Pro.specta acquisitions, as tests with the StarGuide system showed that equation 3.3 leads to an incorrect estimation of the acquisition time for this system. Therefore, for StarGuide's workflows the acquisition time used in equation 3.2 is provided as a user input (figure 3.6A). Consequently, after confirming the placement of the VOI templates, the user is prompted via an input window to enter the acquisition time. In MIM's conversion algorithm, the calibration factor is also provided as a user input. To eliminate this step, the determination of the calibration factor was integrated into the workflow, with the resulting value being automatically fed into MIM's conversion algorithm. To determine the calibration factor, the background spheres were used. The calibration factor was calculated as:

$$CF = \frac{\overline{C}_{BG}}{\overline{V}_{BG} \times c_{BG} \times T} \tag{3.4}$$

where c_{BG} is the activity concentration within the phantom background, $\overline{C}_{BG}$ is the average total counts over the ten background spheres, and $\overline{V}_{BG}$ is the average volume of the background spheres. The background spheres were drawn with identical volumes on the CT scan using MIM's 3D contouring tool. However, as the relevant information is contained in the SPECT images, the contours are transferred by the software to the SPECT scan. Due to the difference in resolution between the CT and SPECT scans, MIM software automatically adapts the spheres diameter to better match the SPECT images, sightly changing their volume in the process. Consequently, the average volume of the ten background spheres was used to calculate the calibration factor. The background activity concentration was implemented as a user input for both SPECT/CT systems, in the same manner as the acquisition time for the StarGuide system. For Symbia Pro.specta, an additional step was included in the developed workflows. The system automatically retrieves the pixel size factor from the DICOM header and divides the image counts by this factor. In contrast to the StarGuide system, where the pixel size factor is defined by the user prior to acquisition, and was set to 1 for all acquisitions considered in this study, the Symbia Pro.specta system automatically defines this factor to compensate, for example, for low statistics. Therefore, it is necessary to correct the image counts by dividing them by this factor prior to quantification.

When the placement of the VOI templates is confirmed and all user inputs are completed,

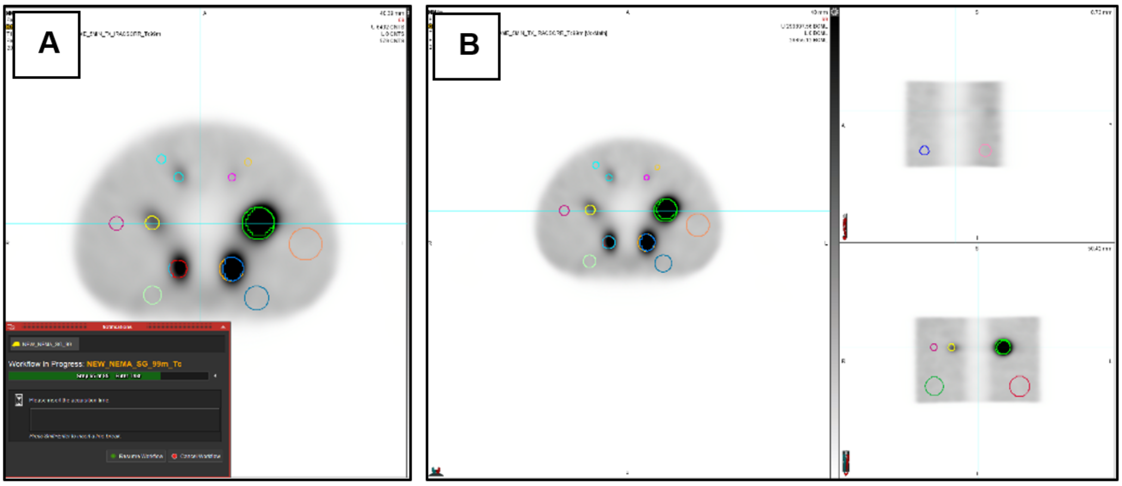

Figure 3.6: Final disposition of the VOI templates after transfer to the SPECT images. Panel A shows the window used to input the acquisition time for StarGuide workflows. A similar window appears for inputting the background activity concentration. Panel B shows the quantitative reconstruction obtained after all confirmations and inputs have been completed.

MIM generates a SPECT reconstruction in units of activity concentration (Bq/ml), including the six additional threshold VOIs described above. The software automatically saves a CSV file to a user-defined location containing the following information: total activity within each VOI (Bq), maximum and mean activity concentration within each VOI (Bq/ml), the standard deviation of the mean activity concentration within each VOI (Bq/ml), and the volume of each VOI (ml). A PDF report is also automatically saved to the selected folder, containing the calibration factor and the parameters used for its determination, defined in equation 3.4. Two tables are included: one reporting the total number of counts within the NEMA spheres and other reporting the total number of counts within the clone spheres are also presented. Finally, graphs showing the average number of counts for the background spheres and for the NEMA spheres are also included.

3.5.1.2 Retrieval of Background Variability Data

The background variability (BV) measures the variation of VOI means over multiple VOIs [75]. In this study, it was used as a measure of image noise and was computed, in percentage, as:

$$BV = \frac{\sqrt{\frac{1}{K-1}\sum_{k=1}^{K}(c_k - \bar{c})^2}}{\bar{c}} \times 100\% \tag{3.5}$$

where K is a predefined number of VOIs, $\bar{c}$ is the average of the mean activity concentration across all considered VOIs, and c_k is the mean activity concentration of VOI k [75]. In this study, the background variability was determined for five sets of 25 identical spherical

VOIs, with each set corresponding to a different VOI volume. The VOI volumes considered were 100, 50, 26.5, 2.6, and $0.5\,ml$, with the last three corresponding to the volumes of the largest, third smallest and smallest NEMA spheres, respectively. To accelerate the data retrieval for each VOI set, the previously described workflow VOI templates were changed to a VOI template containing the 25 spherical VOIs for each volume considered. The VOIs were evenly distributed near the bottom of the phantom, in the central background region of the phantom, and above the NEMA spheres (figure 3.7). In total, since five VOI sets were considered, five BV workflows were defined, thereby simplifying data acquisition for this calculation.

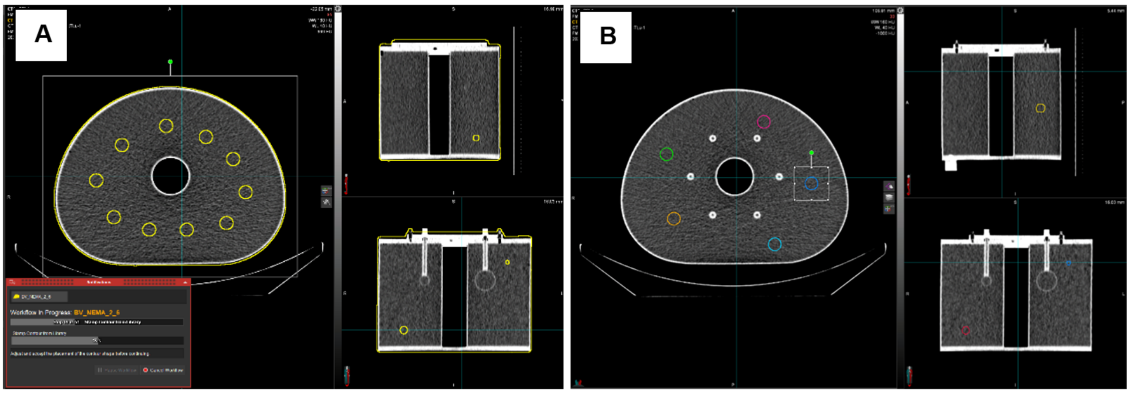

Figure 3.7: VOI template used for retrieving the data needed to compute background variability for the $2.6\,ml$ volume VOI set. The configuration shown in panel A is repeated at the bottom and in the middle of the phantom, accounting for 20 of the VOIs considered. Panel B shows the placement of the remaining VOIs, located above the NEMA spheres.

3.5.2 Quantitative Analysis

The images were quantitatively assessed using the following metrics: recovery coefficients, background variability, signal-to-noise ratio, and contrast recovery coefficients.

3.5.2.1 Recovery Coefficients

For a given NEMA sphere, the associated recovery coefficient (RC) was computed as [53]:

$$RC = \frac{A_{measured}}{A_{true}} \tag{3.6}$$

where $A_{measured}$ is the activity within the considered VOI estimated from the SPECT image, and A_{true} represents the known activity in the considered spherical insert, obtained by multiplying the VOI volume by the NEMA spheres' activity concentration at the time of image acquisition. For a given NEMA sphere, $A_{measured}$ was obtained by subtracting the total activity estimated in the corresponding clone sphere, A_{clone}, from the total activity estimated in the NEMA sphere, A_{NEMA}: $A_{measured} = A_{NEMA} - A_{clone}$. This approach was used to reduce background contributions.

3.5.2.2 Background Variability

The background variability was determined using equation 3.5 for all sets of VOIs defined.

3.5.2.3 Signal-to-Noise Ratio

For each NEMA sphere, the signal-to-noise ratio (SNR) was computed as the difference between the mean activity concentration in that sphere, $\bar{c}_{sphere}$, and the mean activity concentration in the corresponding clone sphere, $\bar{c}_{clone}$, relative to the standard deviation of background clone sphere VOI, SD_{clone} [76]:

$$SNR = \frac{\bar{c}_{sphere} - \bar{c}_{clone}}{SD_{clone}} \tag{3.7}$$

3.5.2.4 Contrast Recovery Coefficients

For each NEMA sphere, the contrast percentage recovery, Q_H, was determined as:

$$Q_H = \frac{\frac{c_{sphere}}{c_{clone}} - 1}{\frac{a_{sphere}}{a_{clone}} - 1} \times 100\% \tag{3.8}$$

where c_{sphere} and c_{clone} correspond to the mean activity concentrations* in the NEMA sphere and the corresponding background sphere, respectively, and a_{sphere} and a_{clone} are the activity concentrations in those spheres (i.e. the ones used to fill the NEMA spheres and the background, respectively) [77].

3.5.2.5 Calibration Factor

The analysis described previously was performed using quantitative reconstructions based on the calibration factor determined by the developed workflow using equation 3.3. This calibration factor was obtained using ten spherical VOIs evenly distributed throughout the background region of the NEMA phantom. The procedure recommended by the EANM quantitative SPECT guidelines involves acquiring a large, uniformly filled phantom, such

*Typically, mean counts within the VOIs are used. However, the developed workflow provides mean activity concentration within each VOI instead. Since conversion from mean activity concentration to mean counts would require multiplying both terms by the same factor ($CF \times V_{VOI} \times T$), this factor cancels out. Therefore, mean activity concentrations were used.

as the Jaszczak phantom, reconstructing and correcting the images using the same parameters applied to patient or NEMA phantom acquisitions, and performing volumetric measures [48]. The approach used in this study accelerated the quantification process, as no additional acquisitions were required to determine the calibration factor, which was computed directly from the NEMA phantom data. Consequently, multiple reconstruction parameters could be evaluated, as there was no need to acquire and reconstruct a separate phantom dataset under the same conditions as the NEMA phantom. To compare these two methods, as described in section 3.2, three acquisitions of 5, 10, and 15 minutes using a ^{123}I-filled Jasckzack phantom were performed and compared to three corresponding NEMA phantom acquisitions, with identical acquisition times. For the NEMA phantom, the calibration factor was computed by the quantification workflow, using equation 3.3. For the Jasckzack phantom, a large spherical VOI, defined on the CT scan with a volume of $2560\,ml$, was positioned inside the phantom (figure 3.8). The calibration factor was then determined as:

$$CF = \frac{C}{A \times T} \tag{3.9}$$

where C is the number of counts within the VOI, A is the activity within the VOI, calculated as the product of the VOI volume and the activity concentration that filled the phantom at the time of image acquisition, and T is the acquisition time.

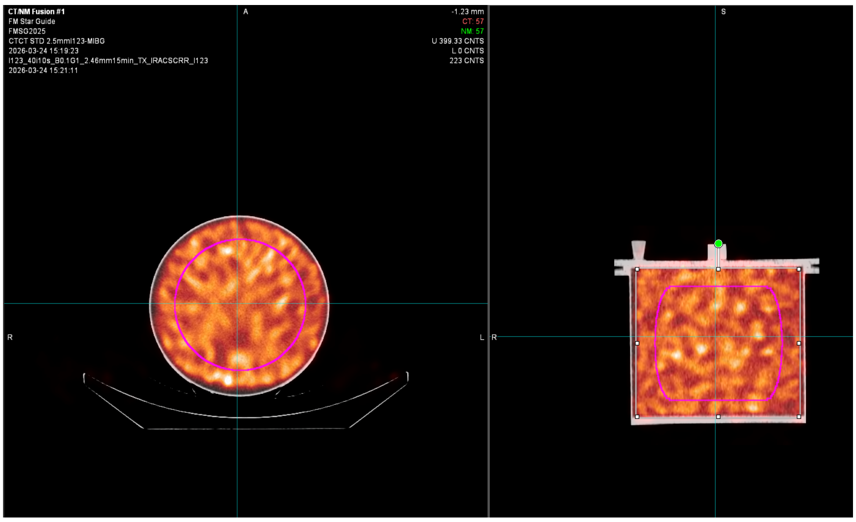

Figure 3.8: Fusion image of the Jaszczak phantom showing the VOI used to determine the calibration factor in MIM Software.

4. Results and Discussion

Following the optimisation strategy detailed in chapter 3, the findings of this study will be presented in the following manner: the first three sections of this chapter are dedicated to the results obtained for each radionuclide studied and corresponding Q.Clear parameters and tools used, in the chronological order in which they were obtained. Accordingly, the results for ^{123}I will be presented and discussed first, followed by ^{99m}Tc and finally by ^{177}Lu. In the last section, a comparison between the results for each isotope is established and a global overview of this study is conducted. Unless stated otherwise, all data analysis was conducted using Python.

4.1. ^{123}I

4.1.1 Optimisation of Q.Clear Reconstruction Parameters

As stated previously, the ^{123}I_StarGuide_1 dataset was reconstructed 20 different times, using the Q.Clear algorithm with RDP regularisation, considering 40 iterations, 10 subsets and all possible combinations of the following values for β and γ: $\beta = 0.01, 0.05, 0.1, 0.5, 1$ and $\gamma = 0.1, 0.5, 1, 3$. For each reconstruction protocol, the RC, BV, SNR and Q_H values were determined. The values obtained were grouped into two major datasets per metric: one containing the values obtained when fixing γ and varying β and the other containing the values obtained when fixing β and varying γ. Consequently, figures 4.1, 4.2, 4.3 and 4.5 present the relationship between β and the corresponding metrics (panel A) and the relationship between γ and the same metrics (panel B). In figure 4.6, a grid containing the NEMA phantom slices corresponding to each reconstruction protocol is presented.

In figure 4.1A, it is possible to see that the RC values decrease as β increases, regardless of the volume of the NEMA spheres. This is consistent with the expected behaviour of a penalised-likelihood reconstruction algorithm such as Q.Clear. As the penalty strength increases, image noise is reduced and the image becomes smoother, since differences between neighbouring voxels are more strongly penalised. Consequently, regions with high activity concentrations are suppressed, and the boundaries between the spheres (regions of high activity concentration) and the background (a region of low activity concentration) become progressively smoother as the algorithm seeks a reconstruction with less abrupt transitions between neighbouring regions. This effect is observable in figure

4.6, where it is clear that, as β increases, the sphere boundaries become less well defined due to the redistribution of activity across the edges. As a result, the area surrounding each sphere becomes more blurred and darker as one moves down each column of the slice grid. Consequently, because the VOI positions are fixed, the total activity contained within each VOI decreases, leading to lower recovery coefficients.

This same principle underlies the decrease in the contrast recovery coefficients as β increases, as observed in figure 4.5A. As the image becomes smoother, the spheres and the background become less distinguishable. This effect is most pronounced for the smallest sphere ($0.5\,ml$), as it is more susceptible to boundary smoothing and spill-out effects due to occupying a smaller number of voxels in the image. As shown in figure 4.6, for $\beta \geq 0.5$, this sphere becomes almost completely blended into the background. Hence, to achieve a recovery of at least 0.2 and a contrast recovery percentage of at least 10% for the smallest sphere, ensuring its detectability and visibility in the images, β values between 0.01 and 0.1 should be considered.

For the smallest spherical VOI sets used to assess image noise ($0.5\,ml$ and $2.6\,ml$), the BV decreases as β increases, as expected due to the increased noise suppression inherent to the reconstruction algorithm (figure 4.2A). In contrast, for VOI sets with volumes greater than or equal to $26.5\,ml$, the background variability remained relatively constant for each β value, at approximately 10%. As these VOIs contain a larger number of voxels, voxel-to-voxel variations tend to average out, making the mean activity concentration and the associated standard deviation less sensitive to changes in the reconstruction parameters, which could explain this behaviour. To reduce noise potentially affecting the smallest VOIs ($0.5\,ml$ and $2.6\,ml$), β should be kept above 0.01 to avoid BV values exceeding 20%.

Excluding the $0.5\,ml$ sphere, the SNR generally increases as β increases, although different behaviours are observed for $\beta > 0.5$, depending on the volume of the sphere analysed (figure 4.3A). The SNR of the $26.5\,ml$ sphere increases with β, reaching its maximum value at $\beta = 1$. This suggests that, despite the loss of signal due to smoothing (as reflected by the decreases in the RC and Q_H values), this effect is not dominant, and the reduction in background noise leads to an overall increase in SNR. For the 2.6 ml and 5.6 ml spheres, a similar increasing trend is observed, although it is less pronounced for the latter. For the $11.5\,ml$ ml sphere, the same general trend is observed, except for a decrease at $\beta = 1$. The $1.2\,ml$ sphere presents the highest SNR values across all volumes for $\beta \leq 0.1$, with SNR further increasing at $\beta = 0.5$ and decreasing again at $\beta = 1$. The reduction at

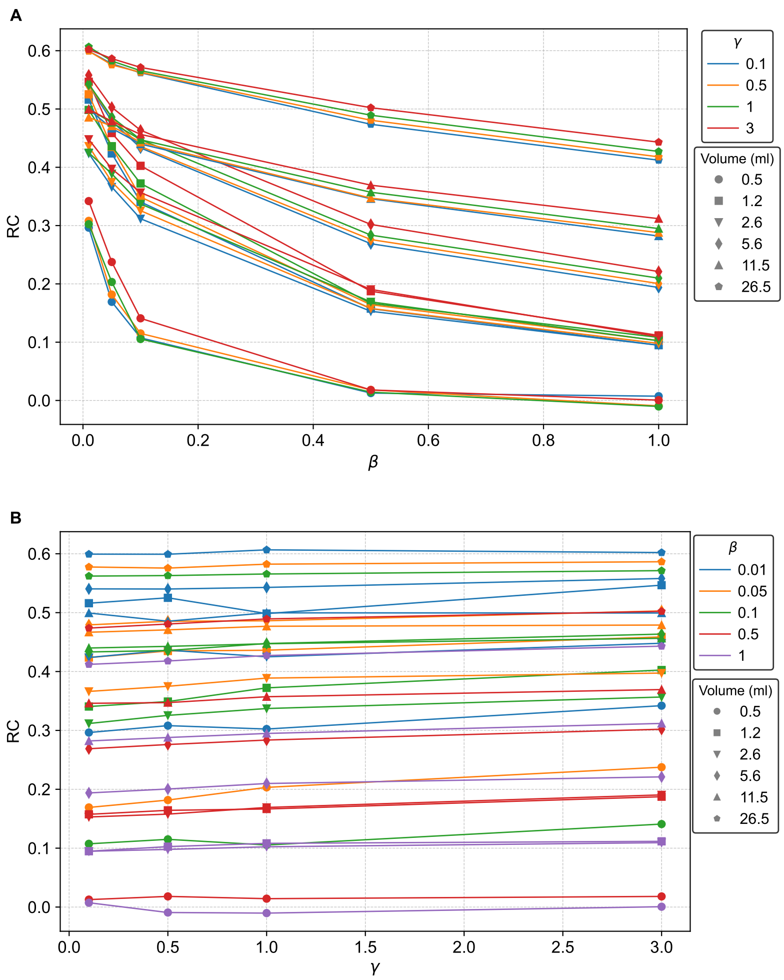

Figure 4.1: Relationship between β and recovery coefficients (A) and between γ and recovery coefficients (B) for all six NEMA spheres for ^{123}I.

$\beta = 1$ is consistent with the observations in figure 4.6, where this sphere (top one) becomes less distinguishable from the background, indicating that at higher β values, noise reduction in the background is no longer sufficient to compensate for signal loss in this volume. The $0.5\,ml$ sphere becomes increasingly blended into the background as β increases, reaching the lowest SNR values observed. As the behaviour of this metric does not follow a consistent trend across sphere sizes, further investigation using intermediate β values could be useful to determine whether Q.Clear preferentially optimises certain lesion sizes. Additionally, the position of the clone spheres (figure 4.4), used to estimate background mean activity concentration and standard deviation, may have biased the results, as some background regions may systematically present higher or lower values. Repeating the analysis with alternative background VOI placements could therefore alter the observed trends. For optimisation purposes, the β value should be kept below 0.5 to avoid the effects observed at higher values in some spheres and to achieve SNR values

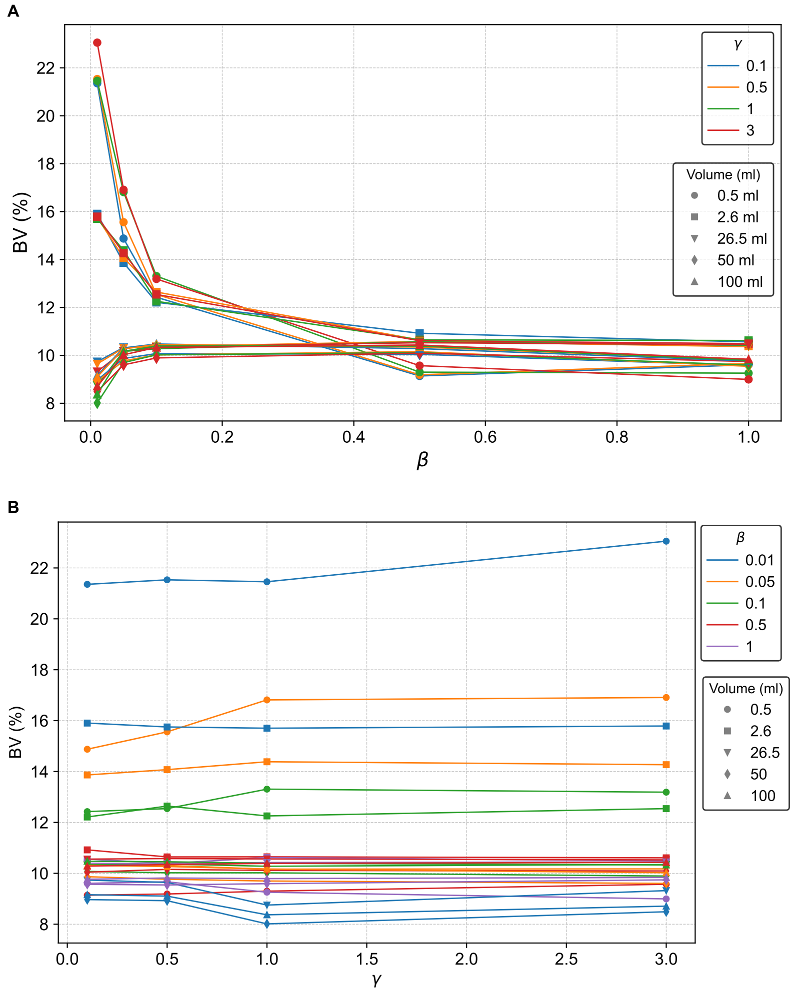

Figure 4.2: Relationship between β and background variability (A) and between γ and background variability (B) for ^{123}I for all VOI sets considered.

above 10 for the smallest sphere.

Choosing the optimal β parameter relies on achieving a balance between quantitative accuracy and noise. Considering primarily the detectability of the smallest sphere, β values below 0.5 ensure the highest RC and Q_H values, whilst still offering acceptable values for the other volumes - always above 0.4 and 30%, respectively. Visually, this also ensures that all spheres can be easily distinguished in the SPECT images. As the lowest SNR and the highest BV values were typically obtained for $\beta = 0.01$, this value should also be avoided. Consequently, the optimal β range can be considered between 0.05 and 1.

Regarding the edge-preservation parameter, γ, it can be observed that the evaluated metrics remain practically unchanged as γ varies (figures 4.1B, 4.2B, 4.3B and 4.5B). Visually, no significant differences could be found between reconstructions with the same β value when moving along each row of the slice grid in figure 4.6. It is relevant, however,

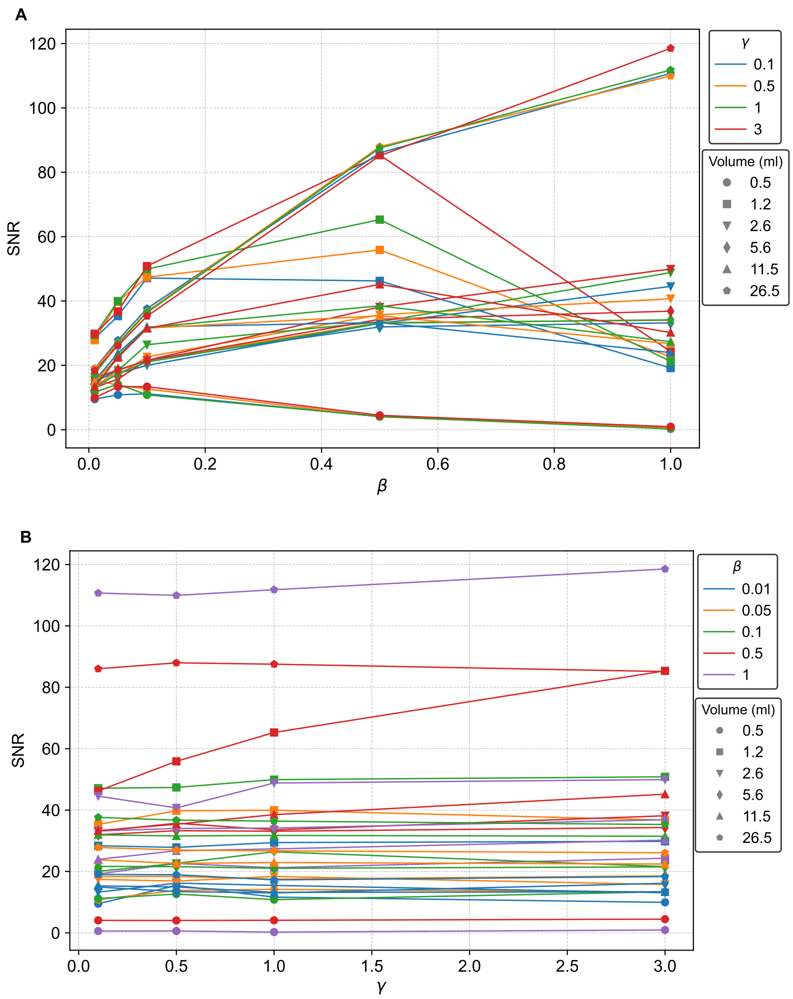

Figure 4.3: Relationship between β and signal-to-noise ratio (A) and between γ and signal-to-noise ratio (B) for all six NEMA spheres for ^{123}I.

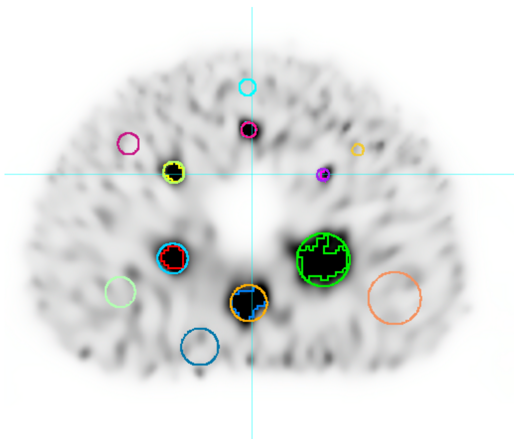

Figure 4.4: Position of the clone spheres relative to the NEMA spheres in MIM Software.

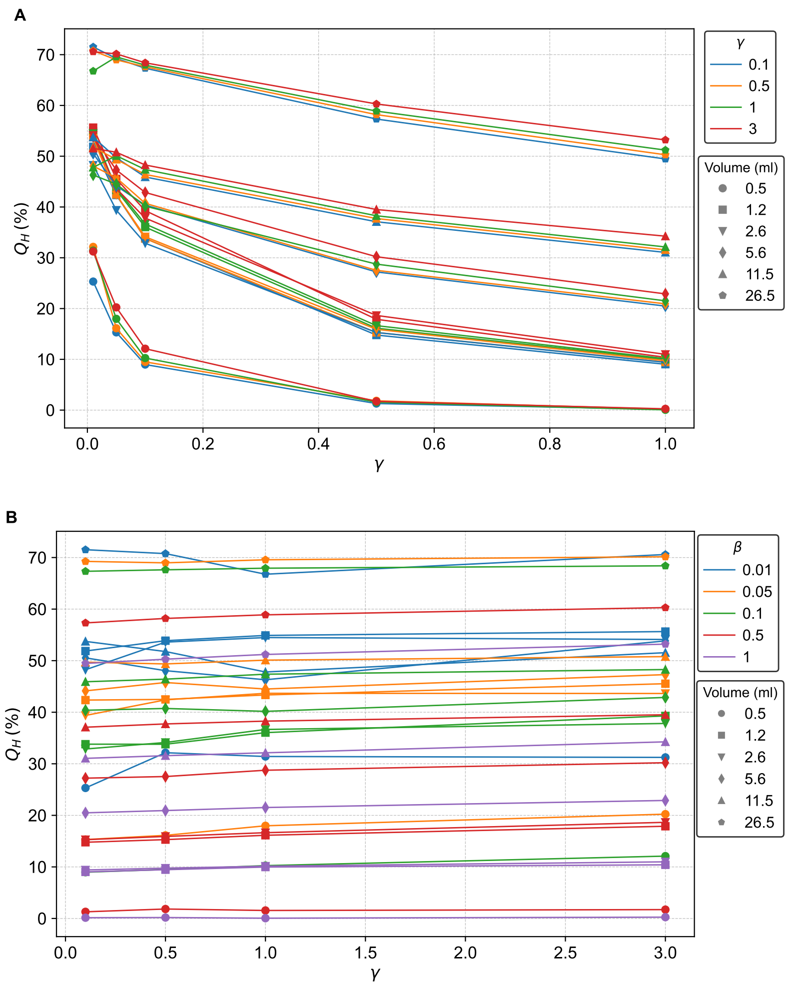

Figure 4.5: Relationship between β and contrast recovery coefficients (A) and between γ and contrast recovery coefficients (B) for all six NEMA spheres for ^{123}I.

to note that for the same β, the highest RC and Q_H values were generally obtained for $\gamma = 3$, which is consistent with a higher degree of edge-preservation in the images, reducing blurring at the boundaries of the spheres and preserving more of the true activity within the VOI borders (red curves in figures 4.1A and 4.5A). Conversely, the lowest values were observed for $\gamma = 0.1$, as seen in the blue curves in the same figures. A slight increase in BV was observed for the smallest spheres when transitioning from $\gamma = 1$ to $\gamma = 3$, while the lowest value of this metric was obtained for $\gamma = 1$ (figure 4.2B). In figure 4.3B, an increasing tendency is observed for the 1.2 ml sphere when fixing $\beta = 0.5$. As this behaviour is only observed for this sphere-β combination, further investigation involving additional γ values could help determine its cause.

Considering the previous analysis, a reasonable compromise between quantification accuracy and image noise can be achieved using intermediate γ values between 0.5 and 1, thereby excluding the γ values leading to the lowest RC and Q_H values ($\gamma = 0.01$) and to

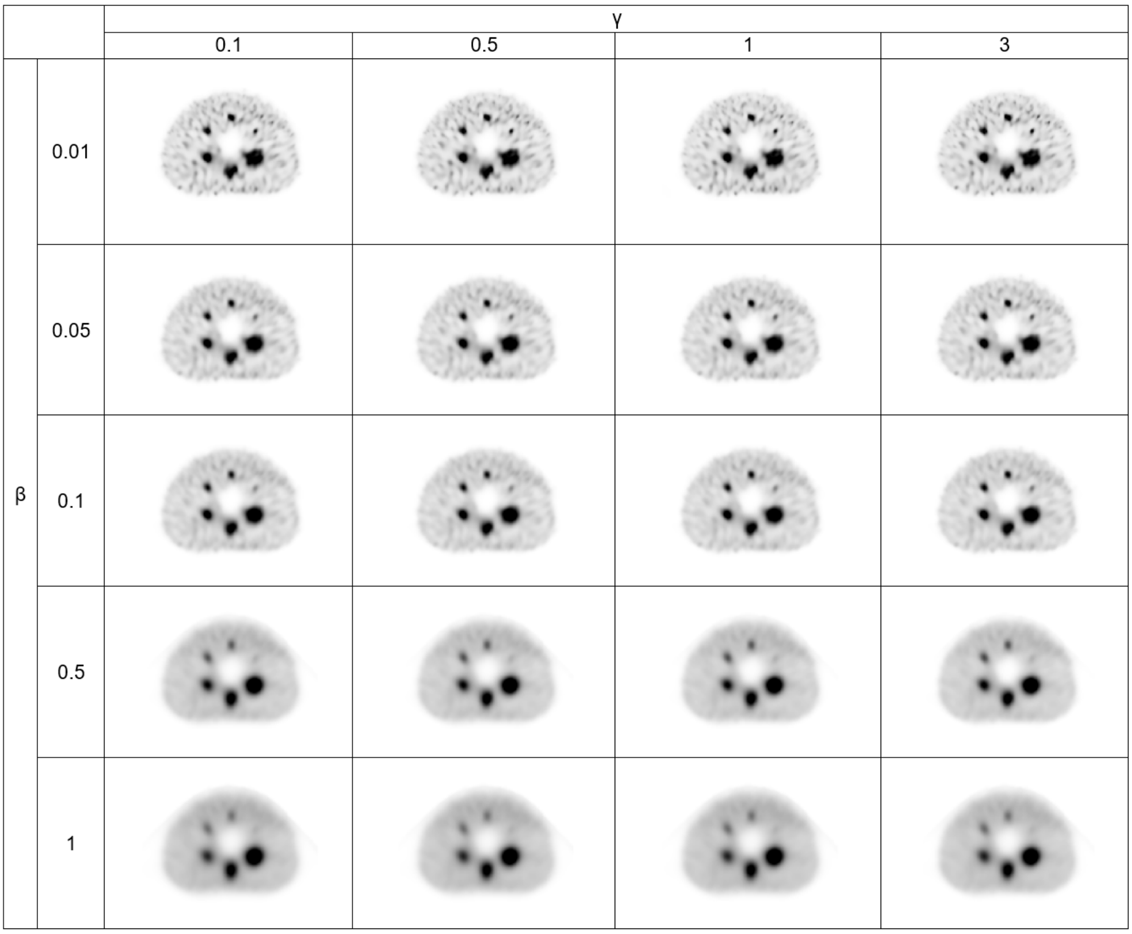

Figure 4.6: Axial views of the NEMA phantom reconstructed using Q.Clear and using the different γ and β combinations.

punctual increases ($\gamma = 3$) in noise, while limiting γ to the value at which the lowest BV was observed ($\gamma = 1$).

Hence, the optimal β and γ combination was defined as β between 0.05 and 0.1, and γ between 0.5 and 1, for the best possible agreement between noise control and quantification accuracy. The reconstruction protocols corresponding to the combinations of the optimal regularisation parameters - $^{123}I\_R7$ ($\beta = 0.05$; $\gamma = 0.5$), $^{123}I\_R8$ ($\beta = 0.1$; $\gamma = 0.5$), $^{123}I\_R12$ ($\beta = 0.05$; $\gamma = 1$) and $^{123}I\_R13$ ($\beta = 0.1$; $\gamma = 1$) - were consequently compared with the OSEM reconstruction obtained for Symbia Pro.specta, thereby comparing the quantitative performance of both systems and reconstruction algorithms. The results of this comparison are presented next.

4.1.2 Quantitative Performance - StarGuide and Symbia Pro.specta

Figure 4.7 presents axial slices of the NEMA phantom reconstructed using the optimal β and γ combinations, compared with the Symbia Pro.specta OSEM reconstruction. Figure

4.8 compares RC, BV, SNR and Q_H across the different reconstruction settings*.

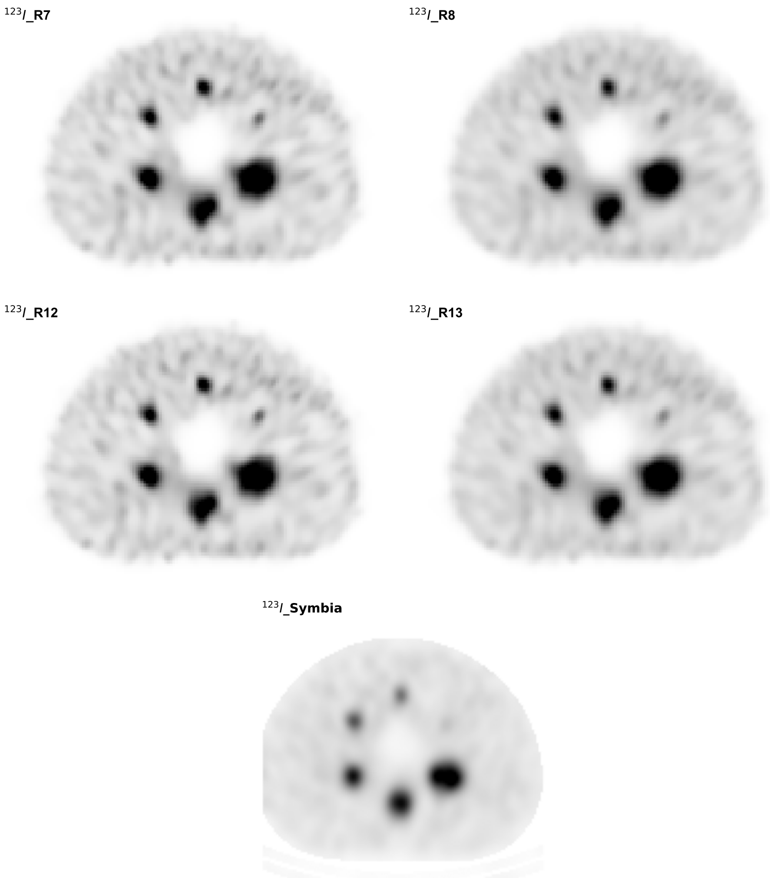

Figure 4.7: Axial views of the NEMA phantom reconstructed using the four optimal Q.Clear settings and using OSEM (Symbia Pro.specta) for ^{123}I.

Regarding figure 4.7, it is visible that the phantom background is smoother and more uniform for the OSEM reconstruction. Comparing the StarGuide reconstructions, it is also possible to observe that, although only slightly, the background appears smoother and less grainy for protocols $^{123}I\_R8$ and $^{123}I\_R13$, which is consistent with the higher β value (0.1) and, consequently, a higher degree of smoothing. The smallest NEMA sphere $(0.5\,ml)$ is identifiable in all StarGuide protocols, while it is barely visible in the OSEM reconstruction. These findings are consistent with the obtained metrics. In fact, all StarGuide reconstructions showed an RC above 0.1 and a Q_H of at least 10% for the $0.5\,ml$ sphere, whereas the Symbia protocol achieved values of 0.07 and 4%, respectively. As a

*It can be seen in this figure, as well as in similar figures throughout this section, that some data points do not have exactly the same x-coordinates, despite these corresponding to the NEMA sphere volumes. This is because, as described in section 3.5 of chapter 3, MIM Software slightly adjusts the VOI boundaries when transferring the VOIs from the CT images to the SPECT images due to the different voxel sizes and image matrix sizes of the two modalities, resulting in small variations in the reported VOI volumes. Consequently, although identical VOI templates were defined for each radionuclide, the effective volumes measured in the SPECT images differ slightly. As minor differences in VOI positioning between datasets are also unavoidable, these volume variations are not identical across acquisitions, leading to the small differences in the x-coordinates observed in the figures.

result, with regard to the detectability of the smallest sphere, the StarGuide protocols are preferred.

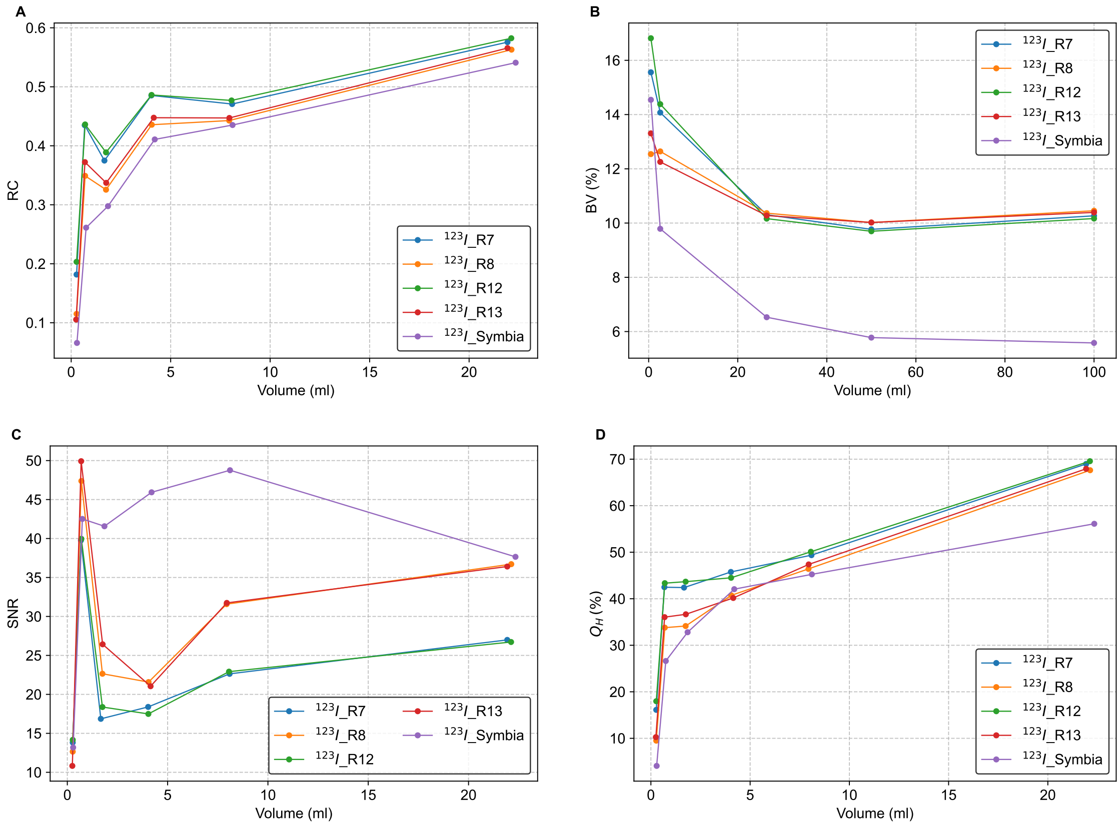

Figure 4.8: Comparison of the recovery coefficients (A), background variability (B), signal-to-noise ratio (C), and contrast recovery coefficients (D) obtained using the optimal reconstruction parameters on the StarGuide system and those obtained on the Symbia Pro.specta system for ^{123}I.

Regarding the noise-related metrics, the OSEM reconstruction generally outperformed the StarGuide reconstructions, with BV stabilizing below 6% for the larger sphere volumes (whereas for StarGuide it stabilizes around 10%) and SNR consistently exceeding 35 for all spheres except the $0.5\,ml$ sphere. Consequently, while StarGuide offered better quantification accuracy as measured by RC and Q_H, the results indicate that further improvements in noise control are still needed.

Observing figure 4.8A, it is possible to see a drop in the RC values from the $1.2\,ml$ sphere to the $2.6\,ml$ sphere. This was unexpected, as RC values typically increase with sphere volume due to the mitigation of partial volume effects that occurs as volume increases. Additionally, all StarGuide protocols showed a peak in SNR for the $1.2\,ml$ sphere, indicating an unexpectedly high signal. Looking at panel B of figure 4.8, it is possible to see that the level of noise in the images is similar, making this behaviour difficult to attribute to differences in image noise. To investigate the possible causes of this behaviour, which was observed for all StarGuide reconstructions, an additional image was reconstructed from the ^{123}I_StarGuide_2 acquisition dataset using protocol $^{123}I\_R13$ - reconstruction $^{123}I\_R13\_1$. The RC and SNR results obtained for this dataset are presented in figure 4.9. Although the same reconstruction protocol was used, lower RC values were obtained. However, neither the drop in RC values observed in the previous results nor the peak in SNR was present. Although no definitive explanation for these observations could be identified, it is possible that the high-energy photon emissions of ^{123}I compromised the quantitative accuracy of the images. In particular, septal penetration and scatter may not have been fully accounted for by the reconstruction algorithm, potentially contributing to the observed effects.

Nevertheless, the general behaviour of the findings is consistent with the previous analysis of the β effects on the image metrics. In fact, it is possible to see that the StarGuide results are organised into two pairs consistently across all graphs: the $\beta = 0.05$ pair (blue and green curves) and the $\beta = 0.1$ pair (orange and red curves). The $\beta = 0.05$ group shows higher RC and Q_H values, consistent with less regularisation and smoothing. The $\beta = 0.1$ group shows, in general, higher SNR values and, for the smallest spheres, lower BV values, in accordance with more effective noise suppression. The exception is the SNR value for the $0.5\,ml$ sphere, which is the lowest for $\beta = 0.1$, consistent with increased sensitivity of small volumes to smoothing effects, as they occupy fewer voxels and are more affected by partial volume effects.

The reconstruction protocol $^{123}I\_R13$* was selected for further comparison with the Symbia reconstruction by attempting to model the RC values using the model proposed by [78], in an EANM guidelines paper: a two-parameter (b_1 and b_2, to be determined by the fit) logistic function, given by:

$$RC\,(v) = 1 - \frac{1}{1 + \left(\frac{v}{b_1}\right)^{b_2}} \tag{4.1}$$

The coefficients of determination (R^2) were calculated to compare the proximity of each reconstruction to the model, with the OSEM reconstruction showing a better fit ($R^2 = 0.919$) compared to the StarGuide reconstruction ($R^2 = 0.820$), primarily due to the unexpected oscillatory behaviour exhibited by the StarGuide RC data.

*This protocol was chosen as it presented, in general, higher SNR values compared to the other StarGuide reconstructions, while still providing, in general, higher quantification accuracy than the OSEM reconstruction.

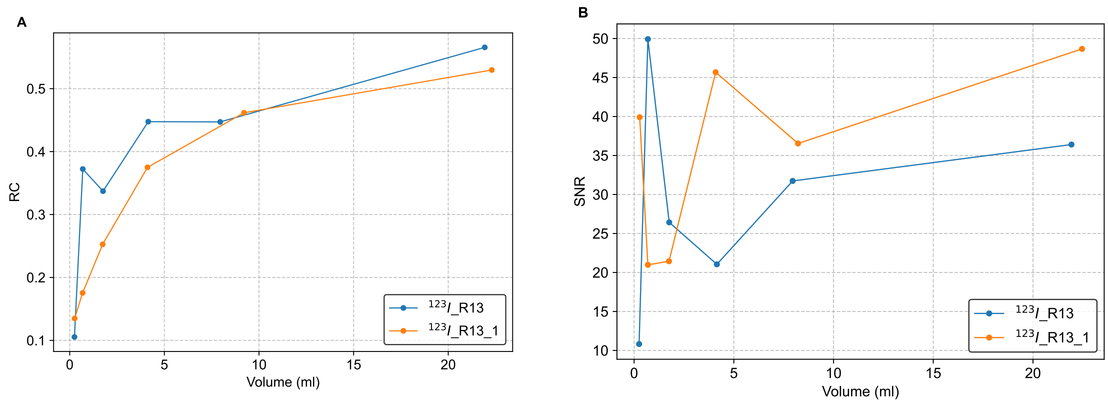

Figure 4.9: Recovery coefficients (A) and signal-to-noise ratio (B) obtained for protocol $^{123}I\_R13$ and for the repetition of this protocol applied to acquisition dataset ^{123}I_StarGuide_2.

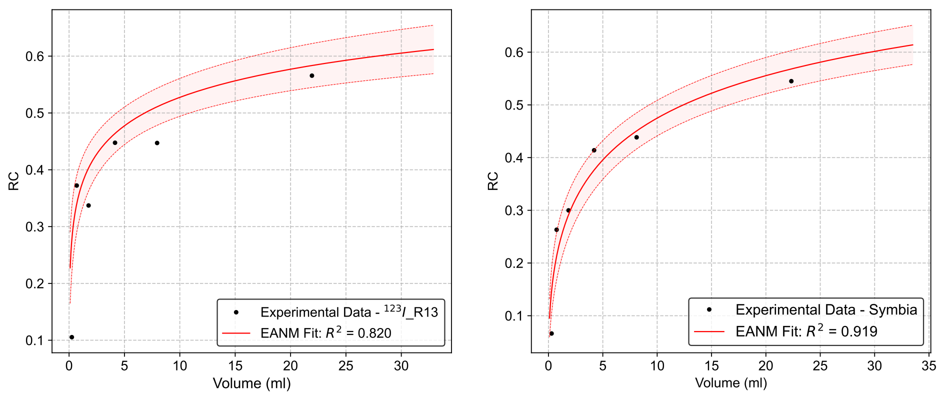

Figure 4.10: Recovery coefficient curves obtained by fitting the EANM model to the StarGuide $^{123}I\_R13$ data (A) and the Symbia Pro.specta data (B). The dotted red lines represent the lower and upper limits of the 95% confidence band for the fitted function.

Finally, an analysis of the cross-sectional activity profile for the $26.5\,ml$ NEMA sphere was conducted for both reconstructions (figure 4.12). As seen in this figure, all profiles appear to converge to a non-zero activity concentration value, reflecting the fact that the background of the NEMA phantom was also filled with activity. Regarding the shape of the profiles, the StarGuide reconstructions are again paired according to β values. At the centre of the sphere, the shape of the $\beta = 0.05$ pair profiles reflects a reconstruction artefact observed for these reconstructions, in which the activity concentration was reduced at the centre of the sphere. This is consistent with the appearance of a spherical shell, known as a Gibbs-like artefact, where the activity is pushed towards the edges of the sphere, forming a spherical shell [23] (figure 4.11). All StarGuide profiles are broader than the Symbia profile, and the transition between the sphere edges and the background is generally smooth, reflecting the effects of smoothing at the edges and activity spill-out.

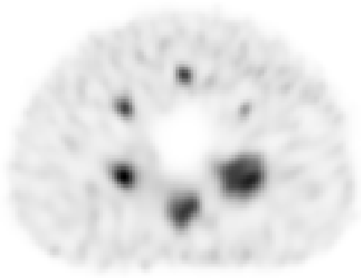

Figure 4.11: Reconstruction $^{123}I\_R7$ displayed with a different colour scale to highlight the artefact observed in the largest sphere.

The profiles were fitted to a Gaussian function, and the FWHM* was computed for each profile. The results are presented in table 4.1. The FWHM obtained is lower for the OSEM reconstruction, reflecting the narrower profile observed in figure 4.12.

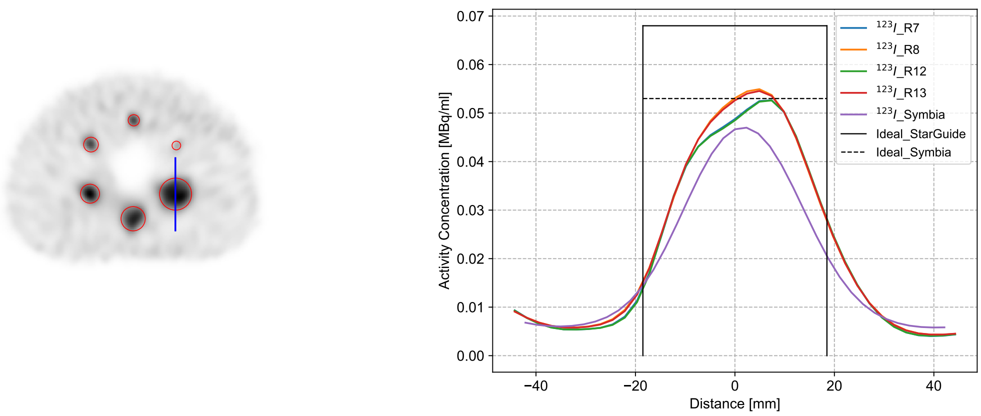

Figure 4.12: Cross-sections through the largest sphere obtained using the optimal reconstruction parameters for the StarGuide and Symbia Pro.specta systems (right). The black step function represents the ideal activity concentration profile for StarGuide and the dashed black line represents the ideal profile for Symbia. On the left, the red circles indicate the physical boundaries of the spheres according to the phantom datasheet, while the blue line indicates the location of the cross-section. The $^{123}I\_R13$ StarGuide image was used as the reference image for the illustration.

*The Gaussian function is given by $f(x) = A\exp\left(-\frac{(x-\mu)^2}{2\sigma^2}\right) + C$. The FWHM was computed as $2\sqrt{2\ln 2}\sigma$, and the associated uncertainty was obtained through uncertainty propagation as $2\sqrt{2\ln 2}\Delta\sigma$, where $\Delta\sigma$ is the uncertainty associated with σ given by the fit parameters [3].

Protocol	FWHM [mm]
$^{123}I\_R7$	29.90 ± 0.96
$^{123}I\_R8$	29.12 ± 0.65
$^{123}I\_R12$	29.98 ± 1.00
$^{123}I\_R13$	29.28 ± 0.70
$^{123}I\_Symbia$	27.27 ± 0.12

Table 4.1: FWHM obtained for the ^{123}I profiles.

4.1.3 Calibration Factor

Figure 4.15 compares the calibration factors obtained using the two methods described in section 3.5.2 of chapter 3, for the three acquisition times considered. The Jaszczak phantom method (orange bars - Jaszczak_1) systematically yielded higher calibration factors than the NEMA phantom method (blue bars). The maximum absolute relative difference between these methods was 9.2% for the 5-minute acquisitions, followed by 7.6% for the 10-minute acquisitions and, finally, by 7.0% for the 15-minute acquisitions. This parameter was computed as $\left|\frac{CF_{NEMA}-CF_{Jaszczak}}{CF_{Jaszczak}}\right| \times 100\%$ for each acquisition time. The Jaszczak calibration factors were used as the reference values as they were obtained using the method suggested by EANM guidelines for quantitative SPECT [48].

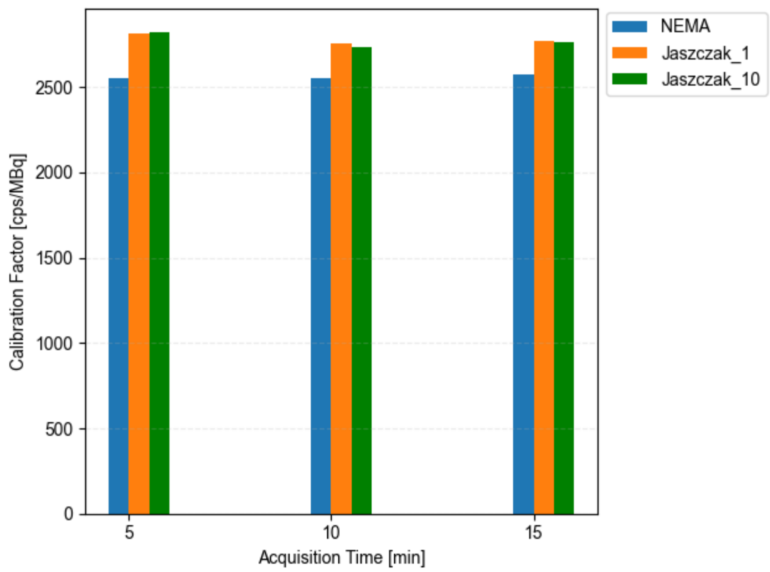

Figure 4.13: Comparison of calibration factors across acquisition times for the NEMA and Jaszczak phantoms.

To explore the tendency for systematically higher calibration factors in the Jaszczak phantom, the NEMA method was replicated on the cylindrical phantom. 10 spherical VOIs with a volume of $51\,ml$ were evenly distributed throughout the Jaszczak phantom, and the calibration factor was computed using equation 3.4. The results (green bars - Jaszczak_10) show that, while there is high consistency between the values obtained for the Jaszczak phantom, the calibration factors remain systematically higher than those obtained using the NEMA method (5 minutes: 9.4%; 10 minutes: 6.8%; 15 minutes: 6.9%). Consequently, to investigate whether the position of the background spheres used to determine the calibration factor for the NEMA phantom influenced the obtained values, the calibration factors were once again determined using the NEMA workflow for the 15-minute acquisition, considering six different positions for the background spheres template (figure 4.14). Positions 1 to 3 are presented in figure 4.14. Positions 4 to 6 correspond, respectively, to the same configurations, but with the spheres placed in a plane above, closer to the NEMA spheres.

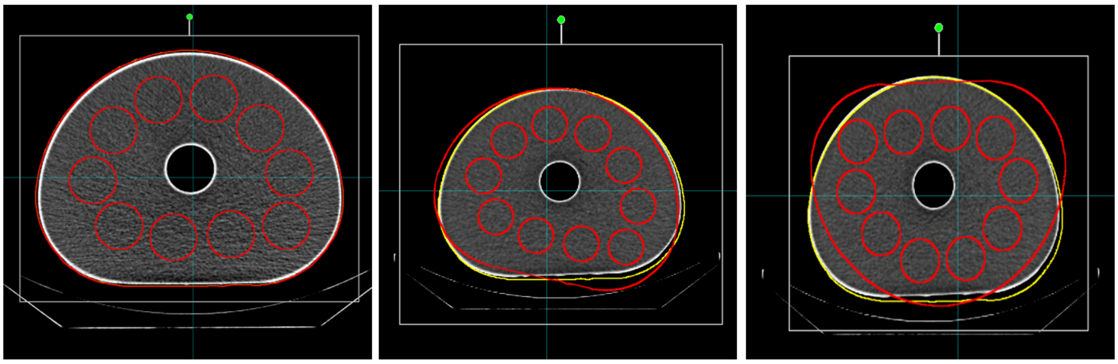

Figure 4.14: From the left to the right, positions 1, 2 and 3 used for the calibration factor determination, using the NEMA workflow. Positions 4, 5 and 6 have the same sphere placement but are vertically closer to the NEMA spheres.

The results show that reducing the distance between the background spheres and the NEMA spheres increased the calibration factor value and reduced the difference between methods to a minimum of 2.3% (position 6). Considering all six positions, the average calibration factor was $2637.5 \pm 46.5\,cps/MBq$, and the absolute relative difference with respect to the Jaszczak phantom was 4.7%.

By placing the background spheres closer to the NEMA spheres, it is possible that more counts are contained within the background VOIs, primarily due to scattered photons originating from the NEMA spheres, which could increase the measured background contribution and, consequently, the calibration factor. These findings reveal that, although the original method did not exceed a 10% difference relative to the Jaszczak approach (15-minute acquisition), the position of the background spheres has a non-negligible influence on the calibration factor calculation and may partially explain the systematic differences

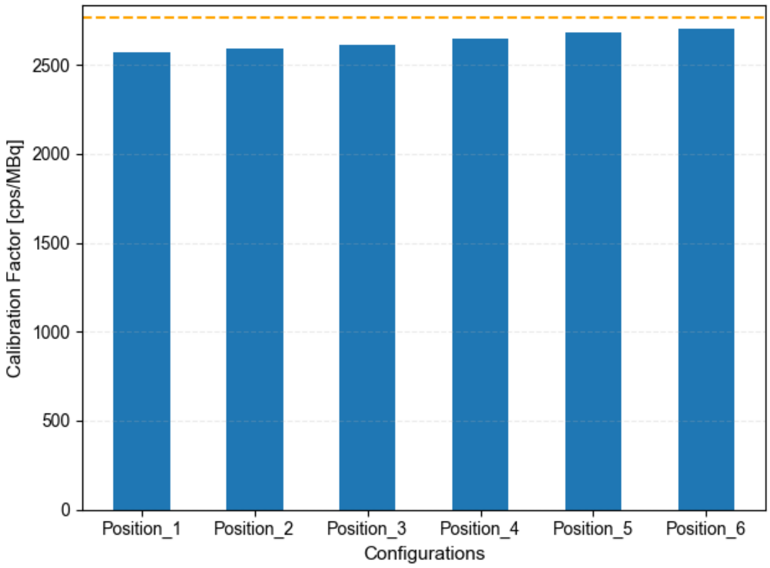

Figure 4.15: Comparison of calibration factors for the six background spheres attempted using the NEMA workflow. The orange dashed line represents the calibration factor obtained for the 10 VOI method using the Jaszczak phantom.

observed between methods. Therefore, several sphere configurations, or a larger number of VOIs, should be considered to obtain a more representative description of the background activity distribution.

For the NEMA method, considering the 15-minute acquisition as reference, an absolute relative difference of 3.3% and of 2.4% was obtained for the 5-minute and 10-minute acquisition, respectively. For the Jaszczak phantom, considering the Jaszczak_1 data, these differences were 1.7% and 0.2%, respectively. The low absolute relative differences, all below 4% regardless of the calculation method, suggest that the calibration factor is largely insensitive to variations in acquisition time, with the Jaszczak approach further reducing this dependence.

4.2. ^{99m}Tc

4.2.1 Optimisation of Q.Clear Reconstruction Parameters

In figure 4.16, the results obtained for RC, BV, SNR and Q_H values are presented for the first four protocols tested. While the same colour represents the same reconstruction settings, the solid lines represent the data obtained for the 15-minute acquisition and the dashed lines the 5-minute acquisition. As stated previously, the reconstruction protocols $^{99m}Tc\_R1$, $^{99m}Tc\_R2$, $^{99m}Tc\_R3$ and $^{99m}Tc\_R4$ were assessed to select the protocol that would undergo fine-tuning. During this stage of the optimisation procedure, the main goal was to maximise the RC values. Consequently, even though all metrics were determined and assessed, the protocol chosen for the next optimisation stage was protocol $^{99m}Tc\_R4$, as it guaranteed the highest RC values of the tested group. In particular, when applied to the 5-minute acquisition dataset, this protocol surpassed the 15-minute values obtained for the other settings.

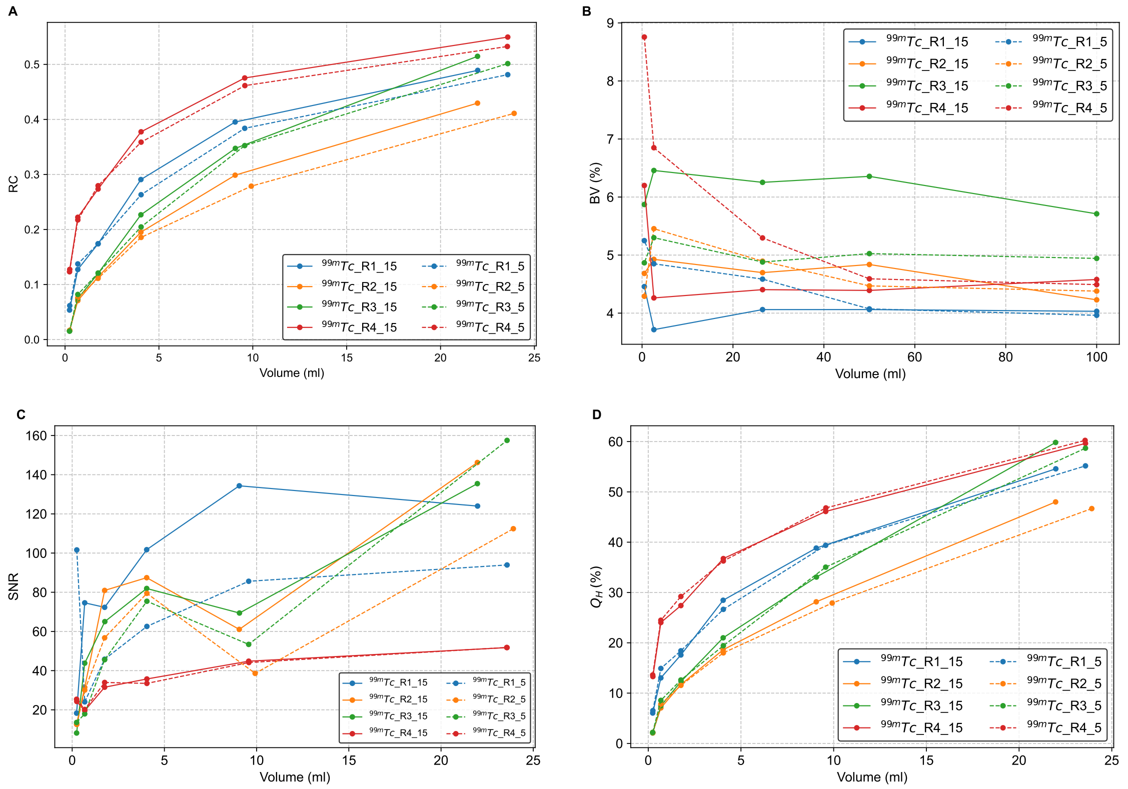

Figure 4.16: Comparison of the recovery coefficients (A), background variability (B), signal-to-noise ratio (C), and contrast recovery coefficients (D) obtained using the first four reconstruction protocols tested on StarGuide between the 15-minute acquisition (solid lines) and the 5-minute acquisition (dashed lines) for ^{99m}Tc.

Regarding the differences in acquisition time, for the same protocol, it is noticeable that the 15-minute acquisition generally yields higher recovery coefficients and signal-to-noise ratio. The Q_H values were similar for both acquisition times. Regarding BV, protocols $^{99m}Tc\_R1$ and $^{99m}Tc\_R4$ exhibited higher values for the 5-minute acquisition. This is in line with what is expected from Poisson count statistics, as 5-minute acquisitions acquire fewer counts (N), and Poisson relative image noise is approximately proportional to $\frac{1}{\sqrt{N}}$ [3]. Protocols $^{99m}Tc\_2$ and $^{99m}Tc\_R4$, which only differed in the use of scatter correction, do not follow this trend. However, as only protocol $^{99m}Tc\_R4$ was further evaluated, further investigation would be required to fully characterise the behaviour of the remaining settings. Based on this results, and considering protocol $^{99m}Tc\_R4$ was the one selected for fine-tuning, the following analysis focus on the 15-minute acquisition dataset.

As shown in figure 4.16C, protocol $^{99m}Tc\_R4$ exhibited low SNR values. Consequently, the primary objective of the fine-tuning phase was to improve this metric. This was achieved by increasing the β parameter, based on the insights gained from the ^{123}I study. Figure 4.17 presents the results for the two tested β values (0.05 and 0.1). As observed in panels A and D, increasing β generally results in lower RC and Q_H values, consistent with increased regularisation strength and image smoothing. Regarding noise metrics, BV was lowest and SNR was highest for $\beta = 0.1$, indicating improved noise suppression.

Considering the above analysis, protocol $^{99m}Tc\_R5$ was chosen as the optimal protocol, as it substantially increased the SNR (58% increase for the largest sphere) when compared to $^{99m}Tc\_R4$, while presenting intermediate values for the recovery and contrast recovery coefficients.

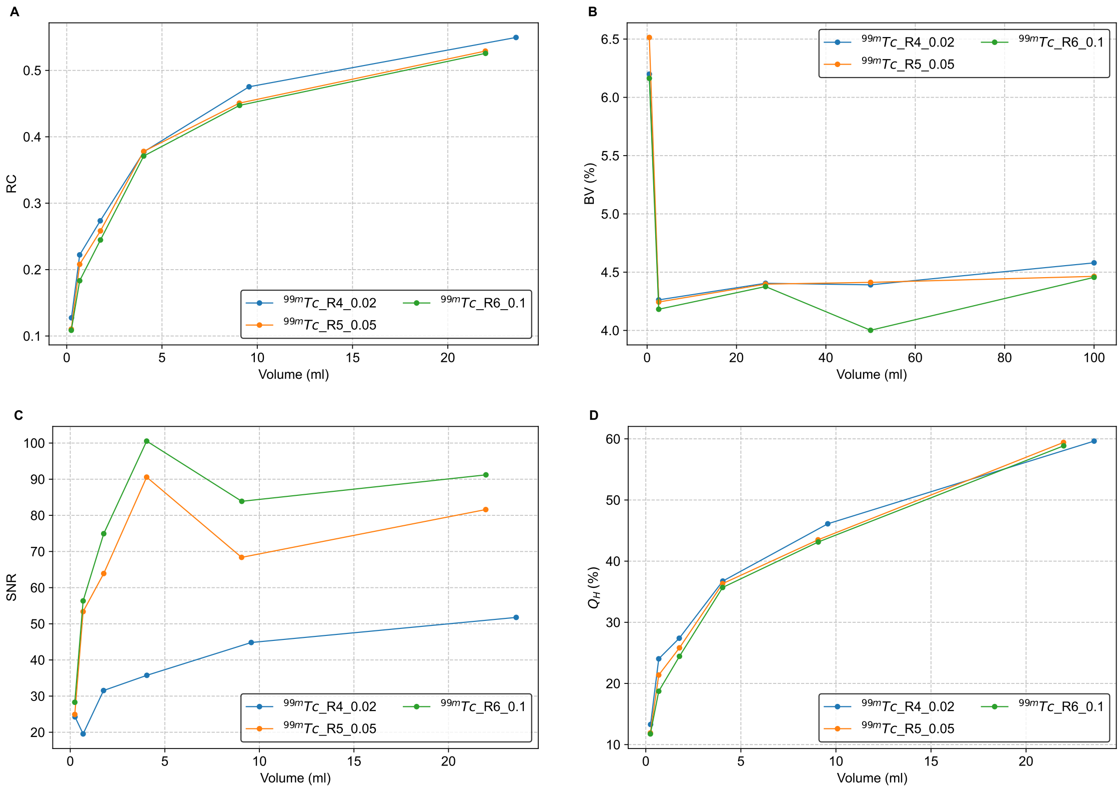

Figure 4.17: Comparison of the recovery coefficients (A), background variability (B), signal-to-noise ratio (C), and contrast recovery coefficients (D) obtained using three different β values: 0.02 ($^{99m}Tc\_R4$), 0.05 ($^{99m}Tc\_R5$) and 0.1 ($^{99m}Tc\_R6$)).

4.2.2 Quantitative Performance - StarGuide and Symbia Pro.specta

Figure 4.18 presents the comparison between StarGuide's optimal protocol and Symbia's reconstruction for all considered metrics for the 15-minute acquisitions. The corresponding axial slices for each protocol are shown in figure 4.20. Visually, both reconstructions are similar.

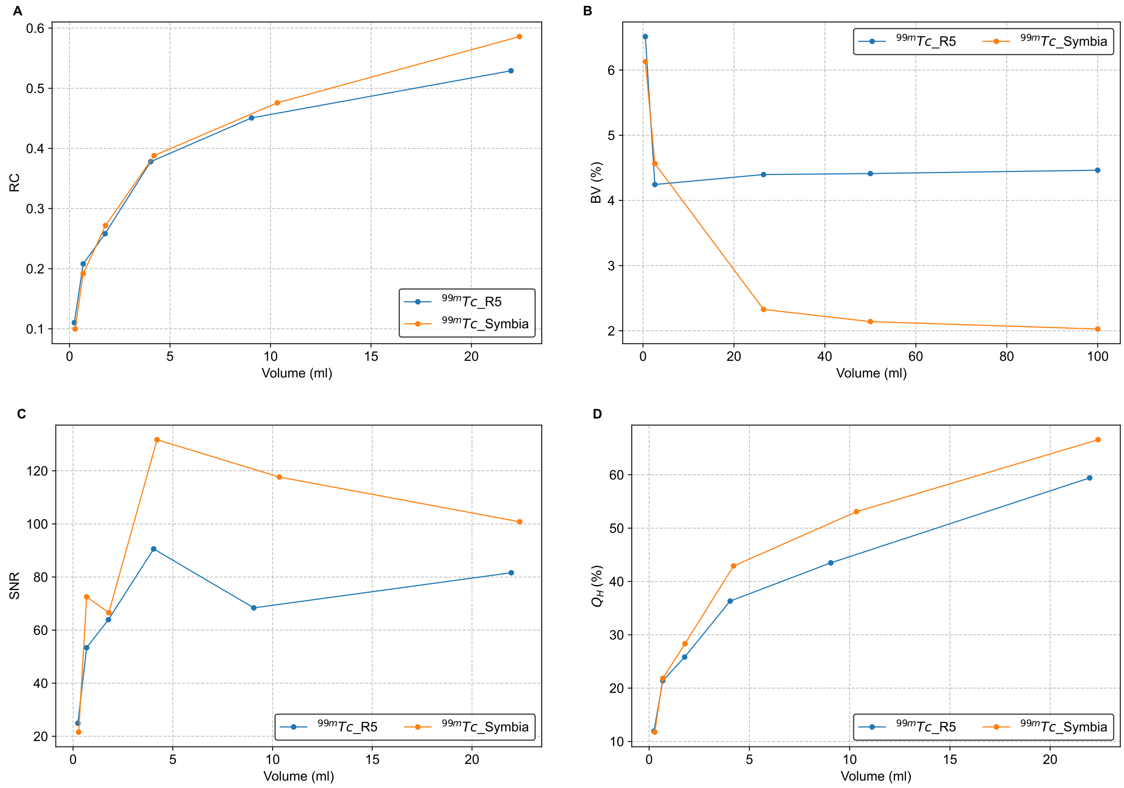

Figure 4.18: Comparison of the recovery coefficients (A), background variability (B), signal-to-noise ratio (C), and contrast recovery coefficients (D) obtained using the optimal reconstruction settings and Symbia Pro.specta for ^{99m}Tc - 15-minute dataset.

Globally, the results obtained for each metric are in line with expectations and are similar to those obtained in the ^{123}I study. Both the RC and Q_H values increase with sphere volume, as partial volume effects and spill-out phenomena are reduced for larger volumes. BV initially decreases with VOI volume, stabilising at approximately 2% for Symbia and between 4% and 4.5% for StarGuide in the larger spheres. Regarding SNR, the general trend observed is an increase with volume up to the fourth sphere, followed by a stabilisation or decrease for the remaining spheres.

Except for the RC values obtained for the first five NEMA spheres, which were similar between algorithms, Symbia Pro.specta generally outperformed StarGuide across all remaining metrics, as shown in figure 4.18. During the optimisation stage, greater emphasis was placed on the RC values, and the optimisation process was halted once recovery coefficients comparable to those of Symbia had been achieved, particularly for the first five spheres, with the aim of obtaining similar quantification performance (figure 4.20A). Consequently, as a result of the study design, no further effort was made to optimise metrics other than SNR during the fine-tuning stage. Accordingly, only the β parameter was explored during the fine-tuning stage, and it is therefore reasonable to suggest that further optimisation of additional reconstruction parameters could improve the performance of the StarGuide system. Although the selected reconstruction settings were optimal with respect to the protocol previously implemented at IPO Porto, they should not be interpreted as representing the global optimum of the StarGuide system in terms of reconstruction performance. Nevertheless, similarly to what was observed for the previous radionuclide, the OSEM reconstructions performed better in terms of noise-related metrics, generally presenting higher SNR values (peaking above 120 for Symbia, whereas the maximum value achieved by StarGuide was approximately 100 for the same sphere) and lower BV values.

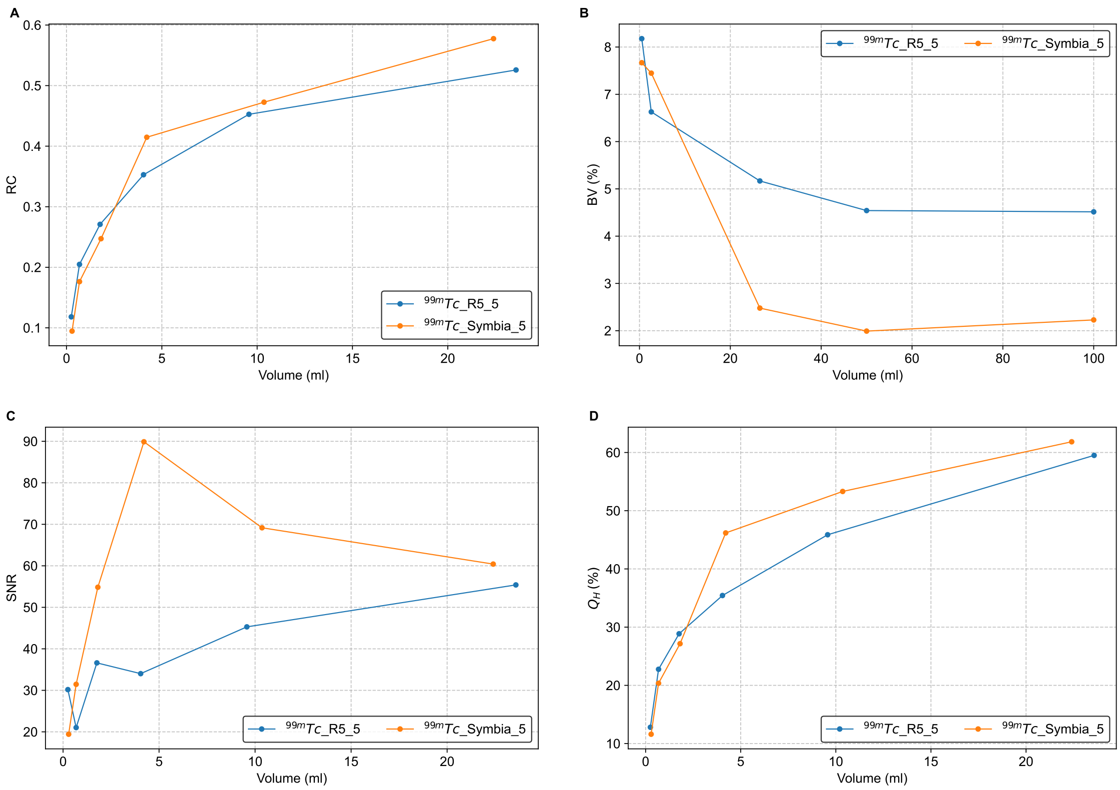

Figure 4.19: Comparison of the recovery coefficients (A), background variability (B), signal-to-noise ratio (C), and contrast recovery coefficients (D) obtained using the optimal reconstruction settings and Symbia Pro.specta for ^{99m}Tc - 5-minute dataset.

In figure 4.19, the results obtained with the optimal StarGuide protocol for the 5-minute acquisition are compared with those obtained using the OSEM reconstruction applied to the 5-minute Symbia Pro.specta dataset. It is possible to see that the behaviour described above is also observed for the noise-related metrics. In terms of RC and Q_H, StarGuide presented higher values for the three smallest NEMA spheres, whereas Symbia outperformed StarGuide for the largest spheres. Consequently, it can be seen that increasing the acquisition time to 15 minutes improved recovery for Symbia, enhancing the detectability of the three smallest spheres while, overall, reducing the performance gap between the two systems. Regarding Q_H, the same trend observed for the 15-minute data is evident, with the systems performing similarly for the three smallest NEMA spheres and Symbia outperforming StarGuide for the remaining spheres.

The RC data obtained with both $^{99m}Tc\_R5$ and $^{99m}Tc\_Symbia$ (for the 15-minute datasets) were fitted using equation 4.1, and the corresponding R^2 values were determined. Both reconstructions showed a good fit to the chosen model, although the fit was slightly better for the Symbia reconstruction ($R^2 = 0.994$).

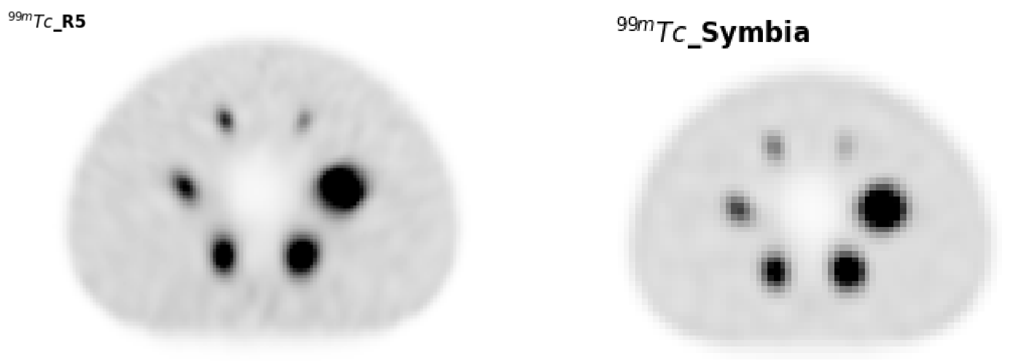

Figure 4.20: Axial views of the NEMA phantom reconstructed with the optimal Q.Clear protocol (left) and with OSEM on the Symbia Pro.specta system (right) for ^{99m}Tc.

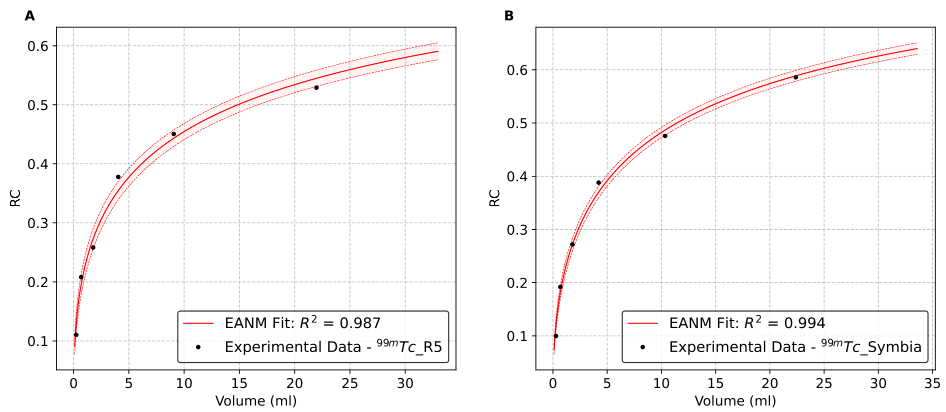

Figure 4.21: Recovery coefficient curves obtained by fitting the EANM model to the StarGuide $^{99m}T\_R5$ data (A) and the Symbia Pro.specta data (B).

The same cross-section analysis done for ^{123}I was repeated for this dataset (figure 4.22). Similarly to what was observed for the previous radionuclide, the StarGuide profile is broader than the OSEM one and both profiles present smooth transitions at the spheres borders, revealing activity spill-out effects, which lower RC values. The maximum peak activity was achieved for the OSEM reconstruction and is closer to the ideal value, which is consistent with the higher RC value for this sphere for this system. The FWHM results are presented in table 4.2 and are consistent with a more gradual fall-out of the peak activity concentration for Q.Clear, as this algorithm prioritizes smoother transitions due to the regularisation penalty, reflecting in a broader profile.

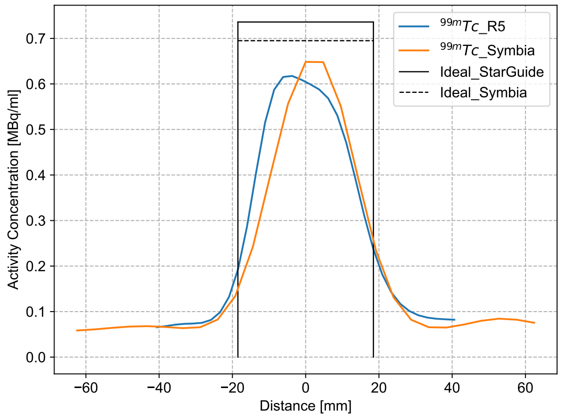

Figure 4.22: Cross-sections through the largest sphere obtained using the optimal reconstruction parameters for the StarGuide and Symbia Pro.specta systems for ^{99m}Tc.

Protocol	FWHM [mm]
$^{99m}Tc\_R5$	28.18 ± 1.03
$^{99m}Tc\_Symbia$	24.94 ± 0.31

Table 4.2: FWHM values obtained for the ^{99m}Tc profiles.

4.2.3 Acquisition Data Reframe

In figure 4.23, the results obtained for the considered metrics for the 5-minute acquisition and the reframed dataset (generated by reframing the 15-minute acquisition dataset to a 5-minute duration) are presented. From figure 4.23, it is apparent that, for the same protocol, the reframed dataset generally performs better than the 5-minute acquisition in terms of RC and Q_H values. Regarding the noise-related metrics, while SNR exhibits a variable behaviour for both protocols, BV increases for the reframed dataset, particularly for the largest spheres. Although the origin of these differences was not investigated further, the results indicate that reframing may be a suitable approach for approximating shorter acquisitions for quantification studies.

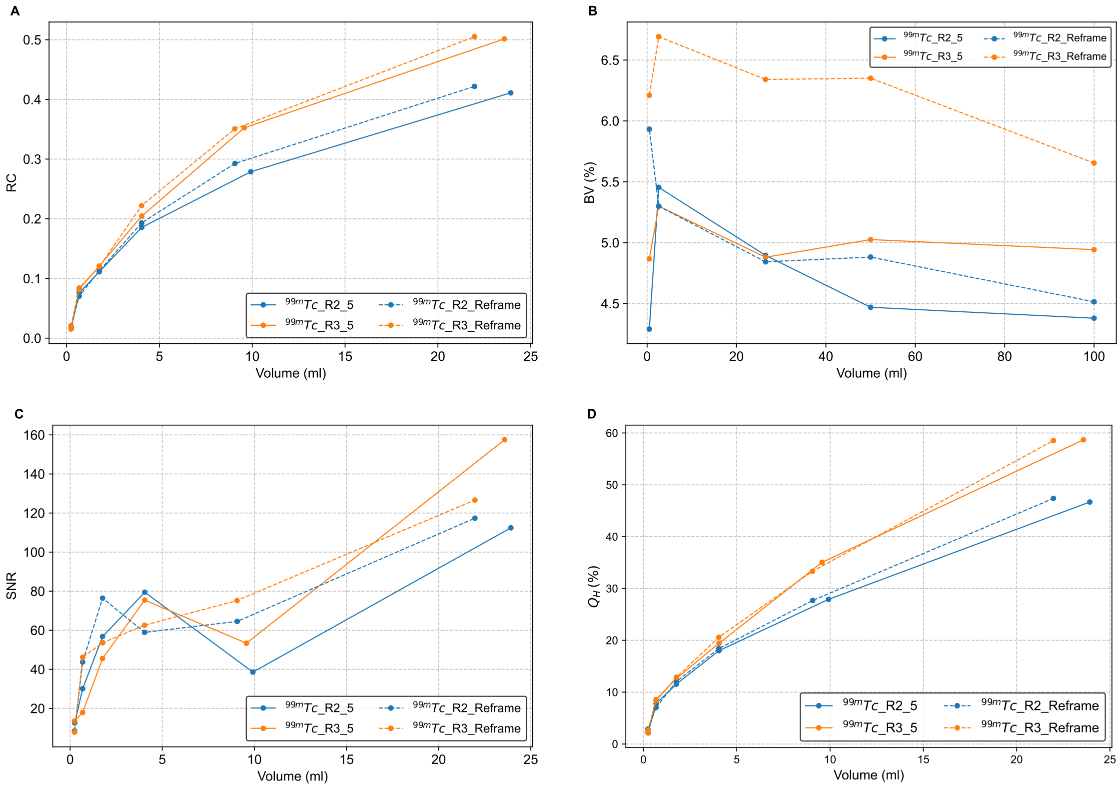

Figure 4.23: Comparison of the recovery coefficients (A), background variability (B), signal-to-noise ratio (C), and contrast recovery coefficients (D) obtained for the true 5-minute acquisition (solid lines) and for the reframed data (dashed lines).

4.2.4 By Sens Tool

The By Sens tool was activated for the ^{123}I optimisation study and for the $^{99m}Tc\_R4$ to $^{99m}Tc\_R6$ reconstruction protocols. As stated previously, the latter protocols were repeated with the By Sens tool deactivated to assess its impact on the image quality metrics. When this tool is deactivated, the β parameter is constant, as the CT-derived sensitivity map is no longer taken into account. Consequently, the regularisation penalty strenght is equal throughout the image. In figure 4.25, the results obtained using the By Sens tool (solid lines) are compared with those obtained using the same protocols (same colours) with this option deactivated (dashed lines). Figure 4.24 presents the corresponding axial views of the NEMA phantom reconstructions for each scenario. The top row corresponds to the images reconstructed using the By Sens tool, whereas the bottom row corresponds to those reconstructed without it.

Visually, the main difference between the reconstructions obtained with and without the By Sens tool is observed in the phantom background, which becomes noticeably more uniform and darker when the tool is deactivated, losing the grainy texture visible in the top row of figure 4.24. Additionally, within each row, an increase in image blur can be

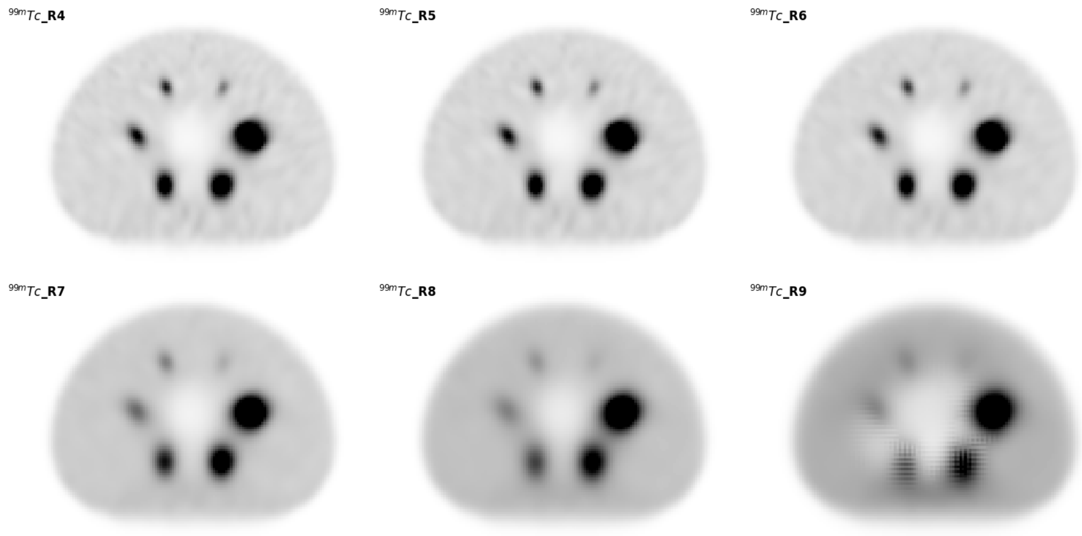

Figure 4.24: Axial views of the NEMA phantom reconstructed using the By Sens tool for $\beta = 0.02, 0.05, 0.1$ (top) and not using the By Sens tool for the same β values (bottom).

observed with increasing β, consistent with the stronger regularisation and smoothing associated with higher β values. Regarding figures 4.25A and 4.25D, deactivating the By Sens tool leads to a clearer differentiation between the tested β values, as evidenced by the increased separation between the curves and the generally lower values obtained. Nevertheless, the highest RC and Q_H values are still observed for $\beta = 0.02$.

Contrary to what was previously observed, when the By Sens tool was deactivated, SNR decreased with increasing β and BV was the highest for $\beta = 0.1$. These findings contradict the previous results, as it was expected that higher β values, associated with a stronger regularisation and smoothing, would favour the noise-related metrics. To date, no studies have been found reporting on the influence of the By Sens tool on image quality metrics. The observed differences in behaviour suggest that, when the tool is enabled, its effect may partially compensate for changes in the β parameter. Consequently, further investigation would be required to assess the influence of β on image quality in the absence of this tool, as the impact of regularisation appears to depend on whether By Sens is applied.

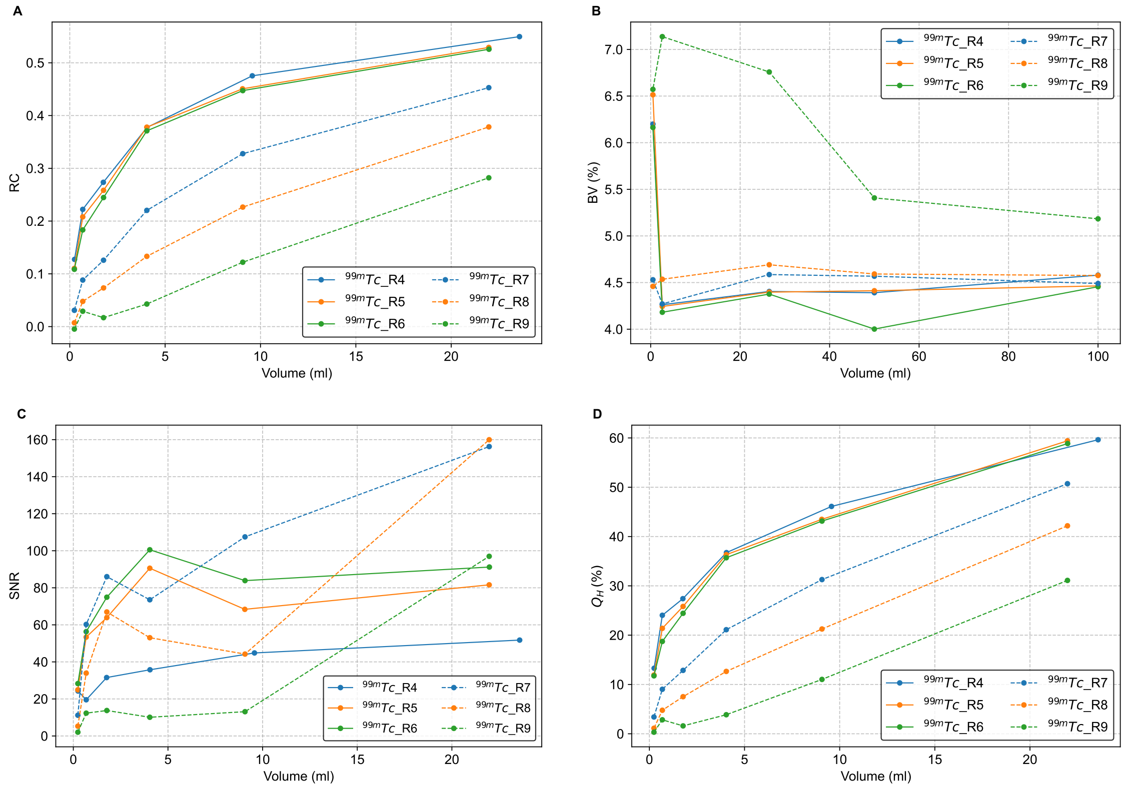

Figure 4.25: Comparison of the recovery coefficients (A), background variability (B), signal-to-noise ratio (C), and contrast recovery coefficients (D) obtained for the protocols using the By Sens tool (solid lines) and not using the By Sens tool (dashed lines).

4.3. ^{177}Lu

4.3.1 Optimisation of Q.Clear Reconstruction Parameters

The results obtained for the RC, BV, SNR and Q_H values for the first four tested protocols are presented in figure 4.26. Due to the strong overlap of data points, the results for each metric were divided into two panels: the right panel shows the 5-minute acquisition data, and the left panel shows the 15-minute acquisition data. The graphs for each metric share the same y-axis to ensure comparability between acquisition times. For ^{177}Lu, as stated in section 3.4.1.3 of chapter 3, two reconstruction settings are defined: one for the $113\,keV$ image and another for the $208\,keV$ image. The results presented here correspond to the voxel-wise average of the peak images, which, for simplicity, will be referred to as the averaged image.

Regarding differences in acquisition time, the most noticeable change occurs in the BV metric. The BV values determined for spheres with volumes $\leq 2.6\,ml$ decrease for all protocols when acquisition time is increased, reflecting a higher-count regime. Globally, SNR values also increase with longer acquisition time, consistent with the lower background noise expected for longer acquisitions. Regarding the quantitative accuracy metrics, with the exception of protocol $^{177}Lu\_R4$, the 5-minute acquisition generally performed better, yielding higher recovery and contrast recovery values. However, since this trend is not observed for all protocols, it cannot be attributed solely to acquisition time and is most likely due to the combination between the complex StarGuide reconstruction parameters and the acquisition time differences. Therefore, a more detailed analysis of the individual characteristics of each protocol would be required to further investigate the observed behaviour.

In order to choose a protocol to fine-tune, the criterion used was once again the maximum value of the RC. In this case, as it was possible to use different settings for each peak, two protocols were further investigated. Protocol $^{177}Lu\_R2$ was selected due to achieving, overall, the highest RC values for the 0.5*, 1.2, 2.6, and $5.6\,ml$ spheres, and protocol $^{177}Lu\_R4$ for achieving the highest RC values for the 11.5 and $26.5\,ml$ spheres, for the 15-minute acquisition. The RC values obtained for the $113\,keV$ and $208\,keV$ images of each protocol are presented in figure 4.27. The settings used for the $113\,keV$ peak in protocol $^{177}Lu\_R2$ yielded RC values of approximately 0.1 for the $0.5\,ml$ sphere and above 0.3 for all other spheres, outperforming the corresponding settings used for the same energy window in the other protocol. Simultaneously, for the two largest spheres, the settings used by protocol $^{177}Lu\_R4$ for the $208\,keV$ energy window lead to the highest RC values.

Consequently, it was hypothesised that, by combining the settings of protocols $^{177}Lu\_R2$ and $^{177}Lu\_R4$ for the reconstruction of the $113\,keV$ and $208\,keV$ images, respectively, improved overall recovery could be achieved. This combined protocol ($^{177}Lu\_R5$) was then evaluated and compared across all metrics with the baseline protocols. The results are presented in figure 4.28.

Overall, the combined protocol showed a strong improvement in recovery when compared with both baseline protocols, with the smallest sphere achieving improvements of 16% and 83% relative to protocols $^{177}Lu\_R2$ and $^{177}Lu\_R4$, respectively, and improvements of 30% and 4%, respectively, for the largest sphere. With the exception of the $1.2\,ml$ and $2.6\,ml$ spheres, this protocol also presented the best Q_H values. Acceptable BV values, compared to the baseline protocols, were also achieved. However, a substantial reduction in SNR was observed, with decreases of 43% and 60% for the smallest sphere and of 9% and 63% for the largest NEMA sphere when compared with $^{177}Lu\_R2$ and to

*Only surpassed by protocol $^{177}Lu\_R3$.

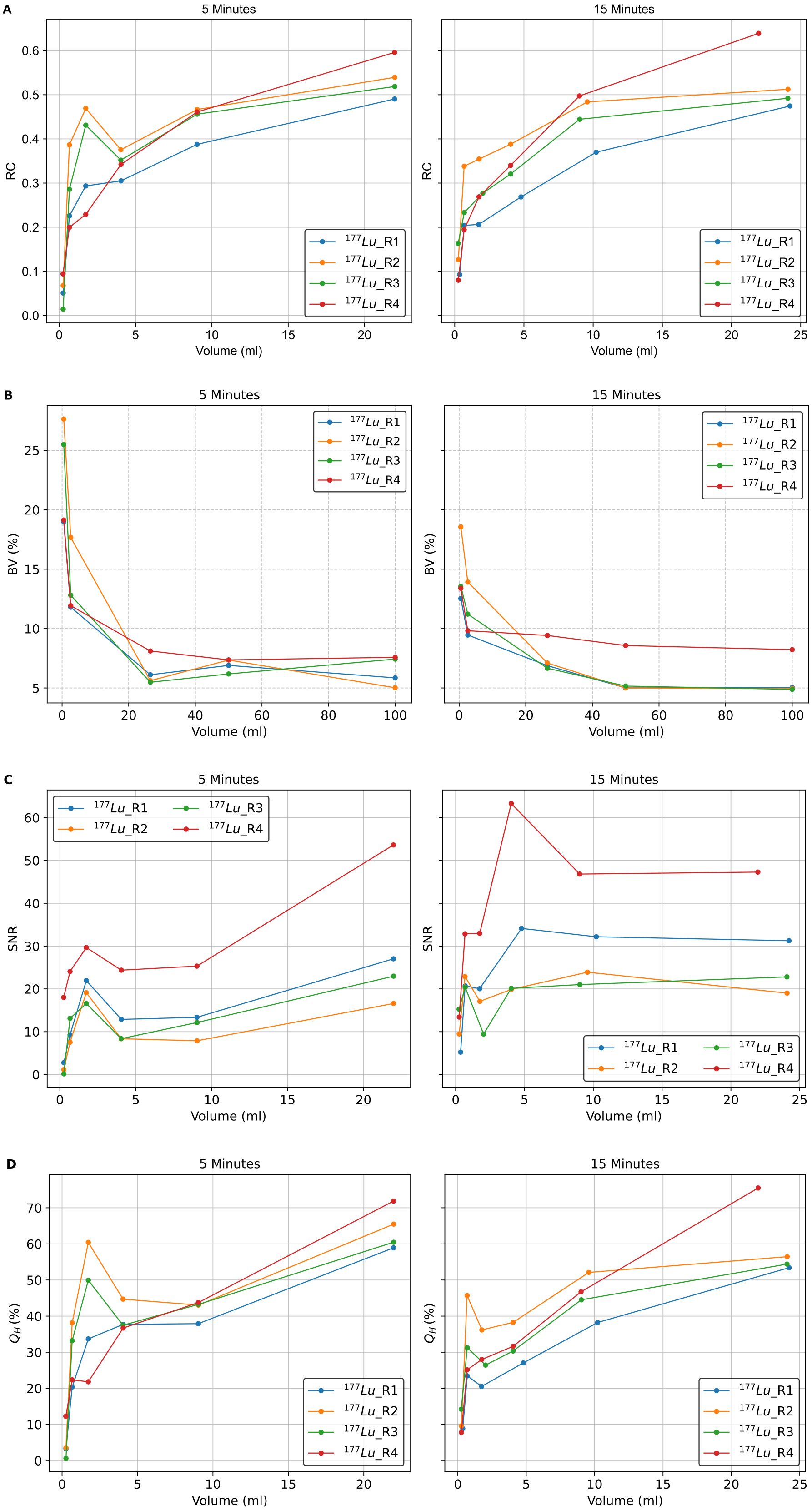

Figure 4.26: Comparison of the recovery coefficients (A), background variability (B), signal-to-noise ratio (C) and contrast recovery coefficients (D) obtained using the first four reconstruction protocols tested on StarGuide between the 15-minute acquisition (left panel) and the 5-minute acquisition (right panel) for ^{177}Lu.

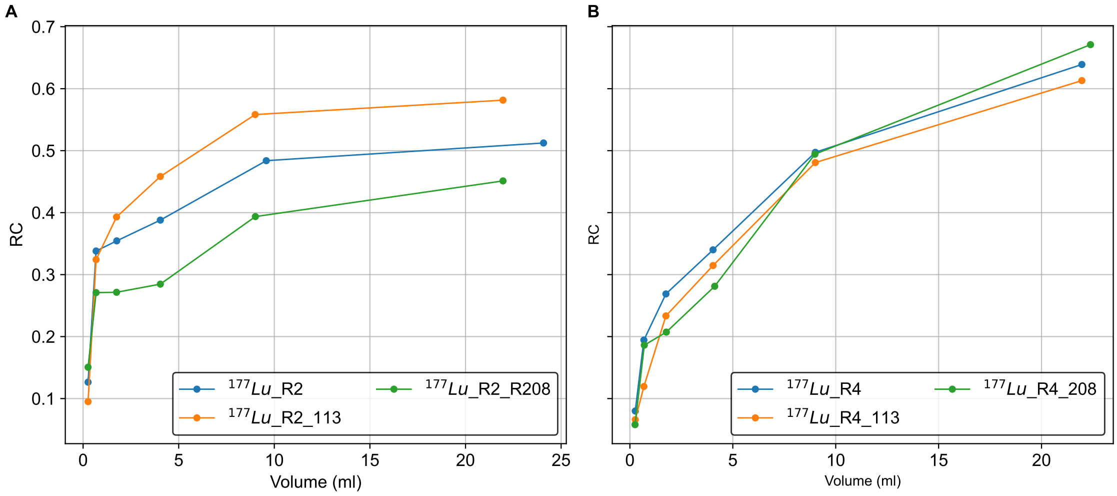

Figure 4.27: Recovery coefficients obtained for the $113\,keV$ and $208\,keV$ images compared to the ones obtained for the averaged image for protocols $^{177}Lu\_R2$ (A) and $^{177}Lu\_R4$ (B).

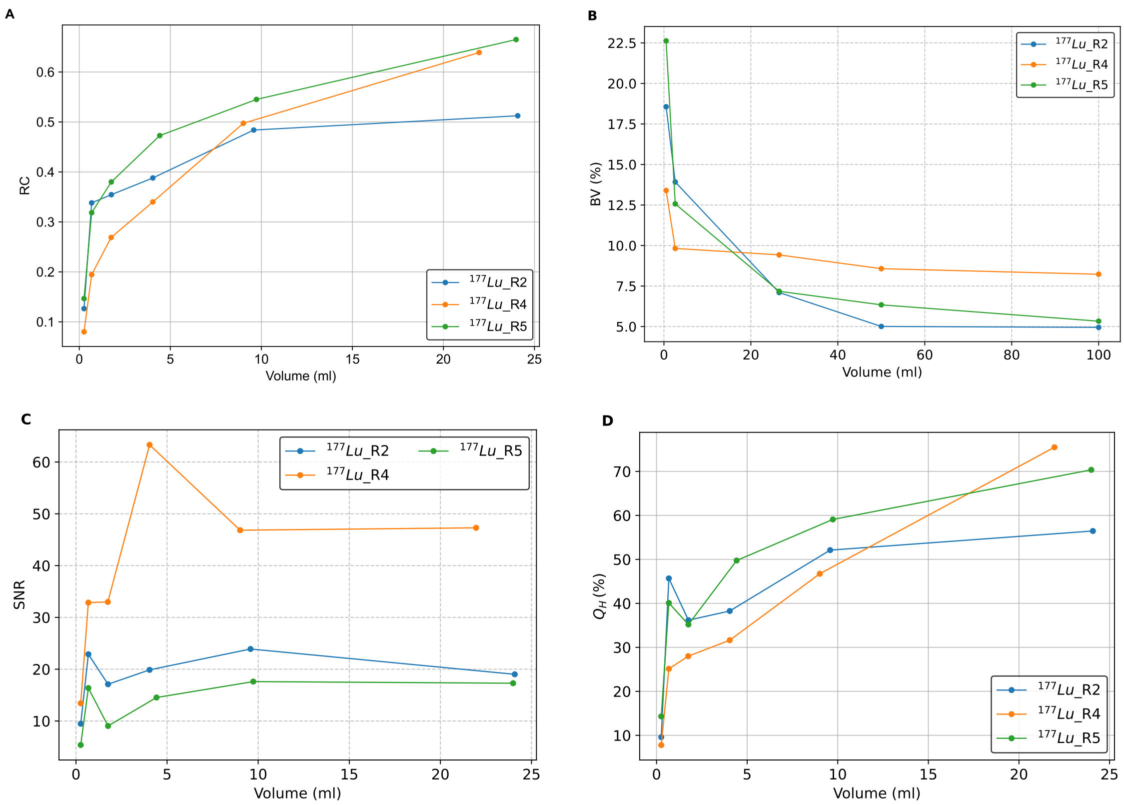

Figure 4.28: Comparison of the recovery coefficients (A), background variability (B), signal-to-noise ratio (C), and contrast recovery coefficients (D) obtained for protocols $^{177}Lu\_R2$, $^{177}Lu\_R4$ and $^{177}Lu\_R5$.

$^{177}Lu\_R4$, respectively. Consequently, in the following optimisation stage, an attempt was made to improve this parameter. Since protocol $^{177}Lu\_R2$ presented the second-lowest SNR, modifications to the combined protocol were applied to the 113 keV energy window, resulting in protocols $^{177}Lu\_R6$ (β increased to 0.2), $^{177}Lu\_R7$ (β increased to 0.3), $^{177}Lu\_R8$ (iterations reduced to 10) and $^{177}Lu\_R9$ (Clarity 3D used with a power of 0.01) (table 3.8).

The results for these protocols, compared to the original combined protocol for the averaged image, are presented in figure 4.29.

As expected, based on the observations previously discussed, increasing β from 0.08 to 0.2 and subsequently to 0.3 in the $113\,keV$ energy window led to a progressive decrease in the RC, Q_H, and BV* values, while the SNR increased accordingly. Similarly, reducing the number of iterations from 20 to 10 resulted in lower BV and higher SNR values. This is in line with the behaviour of iterative reconstruction algorithms, for which image background noise generally increases as the number of iterations rises. Although the penalty term in PL algorithms is intended to mitigate this effect, the regularisation strength used in the original reconstruction for this energy window was relatively low ($\beta = 0.08$), which may explain the observed sensitivity to the number of iterations. Furthermore, the use of the Clarity 3D edge-preservation filter had only a minor impact on the quantitative accuracy metrics, while providing an increase in SNR. For all evaluated protocols, BV remained within a relatively narrow range of approximately 5% to 7.5% for spheres larger than $2.6\,ml$.

For protocols $^{177}Lu\_R6$, $^{177}Lu\_R8$, and $^{177}Lu\_R9$, a pronounced increase in SNR was observed for the $1.2\,ml$ sphere, similar to that previously observed for the StarGuide protocols for ^{123}I (figure 4.8C). The similarity in the shape of the SNR curves raises the possibility that this behaviour may be associated with the behaviour of the reconstruction algorithm itself for objects of this size, rather than representing an isolated occurrence arising from the inherent statistical fluctuations of SPECT imaging.

Protocol $^{177}Lu\_R6$ was selected for further comparative analysis with the OSEM reconstruction, as the increase in SNR was considered to compensate for the reduction in the RC values. Given the previously observed behaviour in ^{123}I and ^{99m}Tc images, it was expected that OSEM would perform better in noise-related metrics. Consequently,

*For spheres with volumes $\leq 26.5\,ml$, with BV stabilizing around the same value for all protocols for larger VOI volumes.

a protocol that could potentially rival this advantage while maintaining acceptable quantitative accuracy was chosen. Nevertheless, protocol $^{177}Lu\_R9$ also yielded an increase in SNR, albeit smaller, while largely preserving quantitative accuracy metrics. Therefore, the choice of optimal protocol should consider the specific application context and the relative importance assigned to each metric.

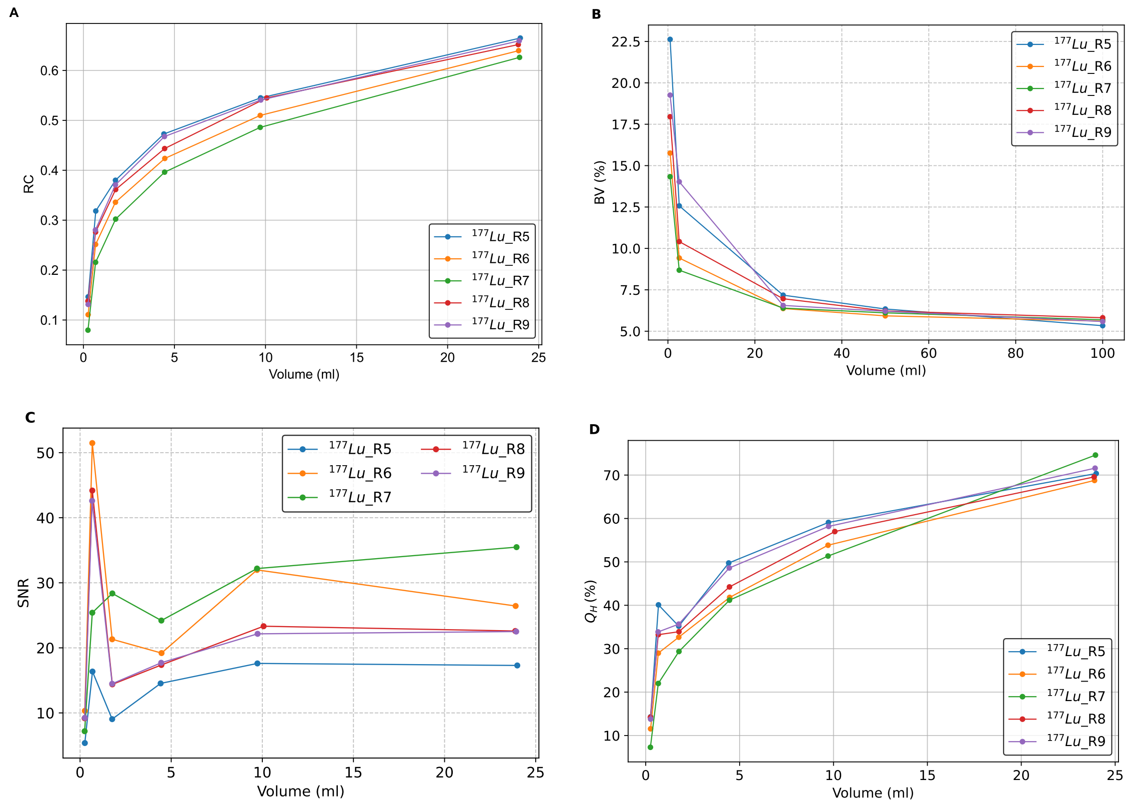

Figure 4.29: Comparison of the recovery coefficients (A), background variability (B), signal-to-noise ratio (C), and contrast recovery coefficients (D) obtained for protocols $^{177}Lu\_R5$, $^{177}Lu\_R6$, $^{177}Lu\_R7$, $^{177}Lu\_R8$ and $^{177}Lu\_R9$.

4.3.2 Quantitative Performance - StarGuide and Symbia Pro.specta

In figure 4.32, the RC, BV, SNR and Q_H values are compared between the optimal reconstruction protocol chosen for StarGuide and the Symbia OSEM reconstruction*. Both the RC and Q_H values increase with sphere volume, in line with what was observed for both systems for ^{99m}Tc and, more generally, for ^{123}I. The BV decreases sharply with volume up to $26.5\,ml$, stabilising at approximately 4% for Symbia and 6% for StarGuide.

The optimal StarGuide protocol outperformed Symbia in terms of RC for all NEMA spheres except the largest ($26.5\,ml$). Regarding the detectability of the smallest sphere, while it

*As the optimised reconstruction protocol was only applied to the 15-minute ^{177}Lu_StarGuide_3 dataset, the 5-minute Symbia acquisition was not used for comparison purposes in this analysis.

is visually significantly blended into the background for both images (figure 4.30), the Q.Clear protocol increased the RC value from 0.07 (OSEM) to 0.11, corresponding to an increase of 57%. The StarGuide protocol also presented higher Q_H for the first four NEMA spheres, ensuring a contrast recovery above 10% for the smallest sphere, representing an increase of 94% compared to the conventional system. In general, and consistent with what was observed for the other radionuclides, Symbia outperformed StarGuide in the noise-related metrics, achieving a maximum SNR of almost 140, compared with just above 20 for the largest sphere in StarGuide, and achieving the lowest BV values. This is consistent with figure 4.30, where clear differences in texture are observed between the Q.Clear reconstruction - noisier and grainier - and the OSEM reconstruction - more uniform - in the phantom's background.

In figure 4.31, the images obtained for the $113\,keV$ and $208\,keV$ peaks for the optimal protocol settings are presented. While the background of the $113\,keV$ window appears noisier, the two smallest spheres are not visible in the $208\,keV$ peak image. Combining these images into an averaged image mitigated these limitations, resulting in a smoother background and improved visibility of the smaller spheres (figure 4.30).

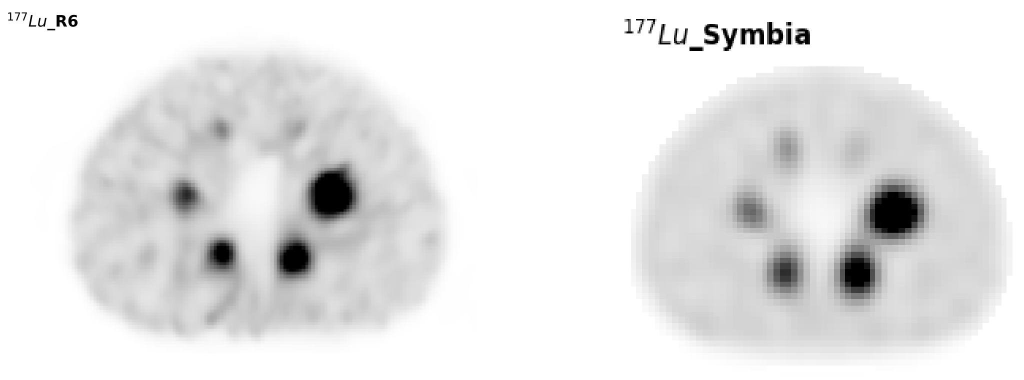

Figure 4.30: Axial views of the NEMA phantom reconstructed with the optimal Q.Clear protocol (left) and with OSEM on the Symbia Pro.specta system (right) for ^{177}Lu.

Both datasets were fitted to the EANM model and were accurately described by it, following the expected trend, as confirmed by the R^2 values: 0.983 for StarGuide and 0.984 for Symbia (figure 4.33).

The cross-section of the largest sphere was also analysed (4.34), with the FWHM values being presented in table. The profile obtained for StarGuide is consistent in shape and

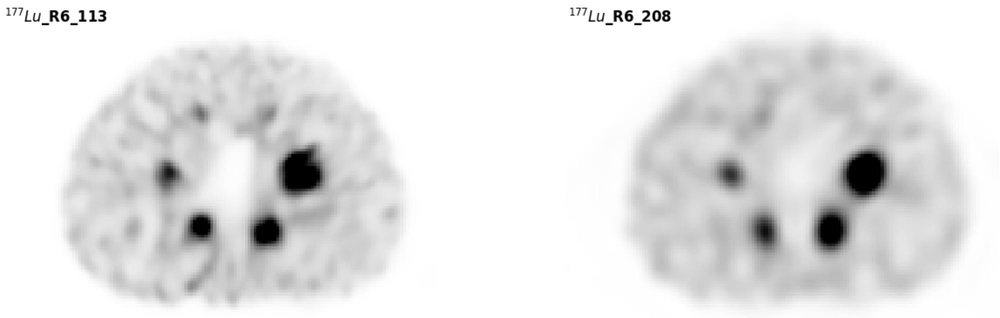

Figure 4.31: Axial views of the NEMA phantom reconstructions using the optimal reconstruction settings for the $113\,keV$ energy window (left) and for the $208\,keV$ energy window (right).

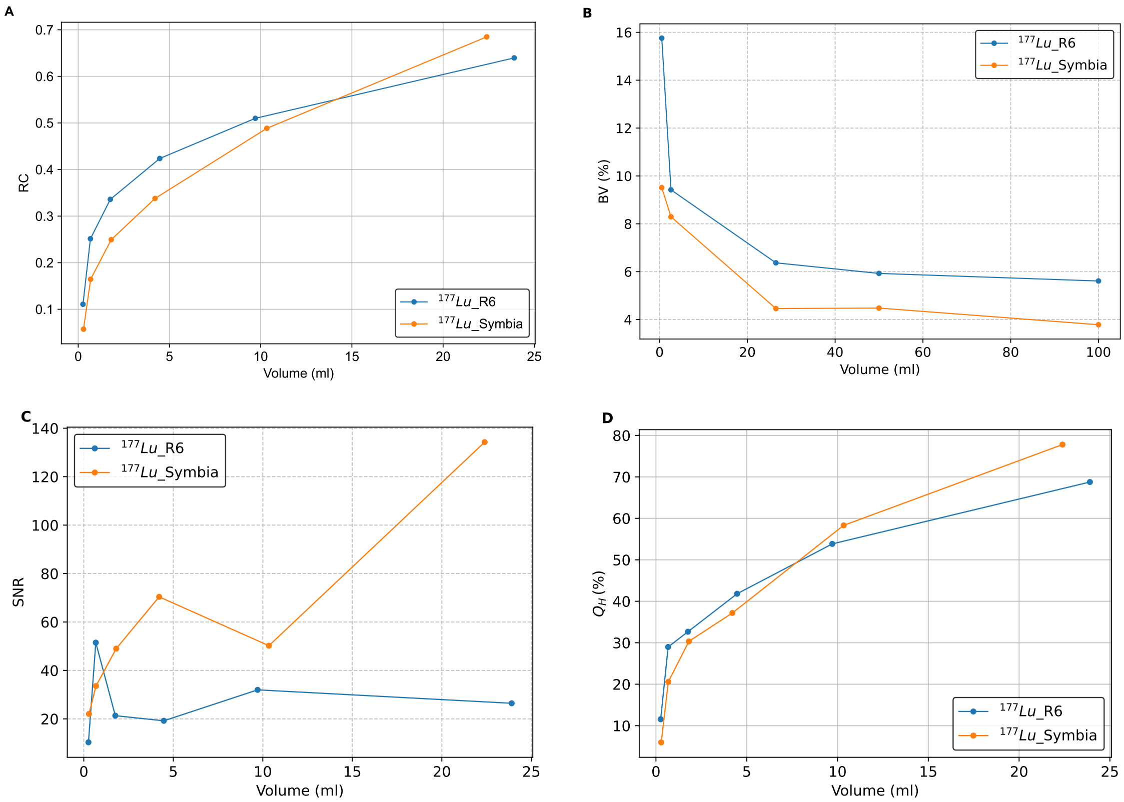

Figure 4.32: Comparison of the recovery coefficients (A), background variability (B), signal-to-noise ratio (C), and contrast recovery coefficients (D) obtained using the optimal reconstruction settings and Symbia Pro.specta for ^{177}Lu.

behaviour with those reported by Danieli et al. when performing the same analysis with Q.Clear and RDP regularisation [23]. Once again, StarGuide produced broader profiles, whereas the OSEM reconstruction exhibited a steeper decay from peak concentration at the centre of the sphere toward the edges.

Considering figures 4.12 and 4.22, the differences between Q.Clear and OSEM are consistent across radionuclides. StarGuide profiles are systematically broader and show a more gradual reduction in activity concentration from the centre toward the sphere boundaries. In both cases, activity spill-out is observed, as the profiles decrease smoothly across the sphere boundaries.

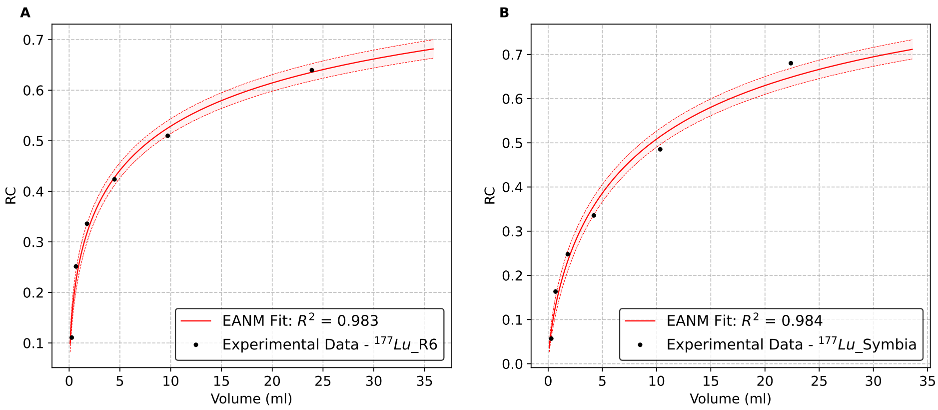

Figure 4.33: Recovery coefficient curves obtained by fitting the EANM model to the StarGuide $^{177}Lu\_R6$ data (A) and the Symbia Pro.specta data (B) for ^{177}Lu.

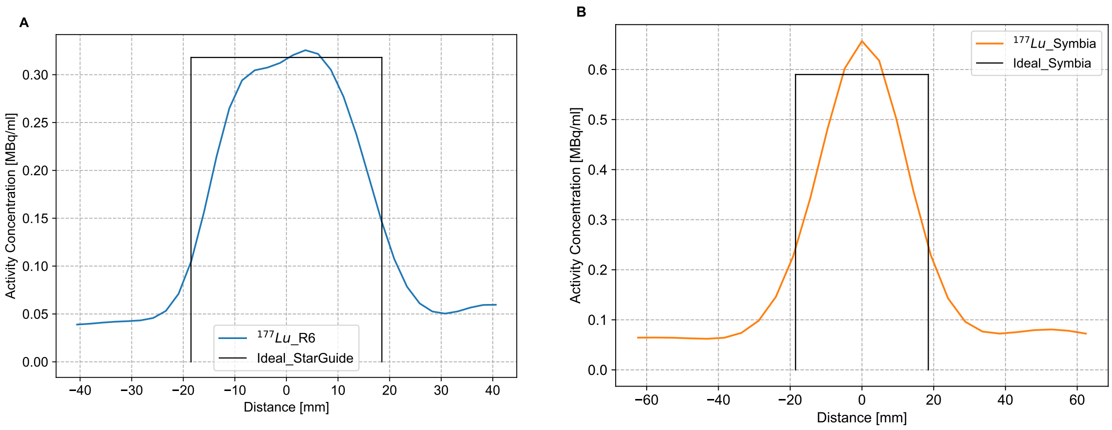

Figure 4.34: Cross-sections through the largest sphere obtained using the optimal reconstruction parameters for the StarGuide (A) and Symbia Pro.specta systems (B) for ^{177}Lu.

Protocol	FWHM [mm]
$^{177}Lu\_R6$	29.11 ± 1.19
$^{177}Lu\_Symbia$	27.84 ± 0.21

Table 4.3: FWHM values obtained for the ^{177}Lu profiles.

4.4. Overview of Q.Clear's Performance

The Q.Clear reconstruction algorithm is a complex reconstruction platform, mainly due to the variety of available settings and their interdependence. From the analysis conducted using the ^{123}I datasets, it was possible to define expectations regarding the behaviour of the image metrics when varying the regularisation parameters, β and γ. While γ had little impact on the analysed metrics, the penalty strength parameter consistently affected the image quality metrics across radionuclides. As a result, even though a radionuclide-specific optimisation was performed, the results indicate that the influence of β on image quality metrics is largely preserved across radionuclides, despite their inherently different emission characteristics.

It was observed that increasing β consistently led to lower RC and Q_H values for all radionuclides. This behaviour has also been reported in the literature in similar optimisation studies - although in the PET domain, as the application of Q.Clear in SPECT is relatively recent [79, 80] - and is consistent with the expected behaviour of penalised likelihood reconstruction. Increasing β also led to reduced BV in smaller spheres and, in general, to higher SNR values. However, an inversion of this trend was observed when the By Sens tool was deactivated, highlighting the need for further investigation of the full Q.Clear parameter space, as additional reconstruction settings can significantly influence the evaluated metrics.

As the main motivation of the optimisation study was to improve RC values, which are essential for applications in personalised dosimetry and theranostics, in order to achieve similar values to those obtained on the Symbia Pro.specta system, the selected optimal protocols were those that achieved comparable (^{99m}Tc) or substantially improved RC values when compared with the conventional system (^{123}I and ^{177}Lu). This approach favoured high recovery, potentially at the expense of the noise control performance. Therefore, several unexplored parameter combinations could further optimise Q.Clear and, consequently, the StarGuide system.

In particular, although good results were obtained in terms of quantification accuracy, there is still room for improvement in noise control. Even basic parameters such as iterations and subsets should be investigated jointly with the regularisation parameters to fully exploit the capabilities of penalised likelihood algorithms such as BSREM.

This study focused primarily on regularisation parameters, as they represent a relatively novel aspect in the SPECT domain, and it contributed to improving the reconstruction protocols currently used at IPO Porto, particularly in terms of quantification accuracy. Future studies should include validation on patient datasets, further optimising these parameters with respect to lesion detectability and clinical interpretation. The visual comparison of the NEMA phantom images also indicates that Q.Clear produces a different background texture compared with OSEM, particularly in uniform regions. As OSEM remains the most established reconstruction workflow, the adoption of Q.Clear will require adaptation from nuclear medicine physicians, and their input should be incorporated into future optimisation studies.

Overall, there are still several nuances in the Q.Clear algorithm, as multiple reconstruction settings can be adjusted and interact with each other. Therefore, using IPO Porto or literature-reported protocols as a starting point does not account for all parameter interactions that may influence image quality metrics.

5. Conclusion

This study investigated the influence of Q.Clear reconstruction parameters on the quantitative performance of ^{123}I, ^{99m}Tc, and ^{177}Lu images. Specifically, it aimed to characterise the impact of the regularisation parameters on image quality and quantification metrics (RC, BV, SNR, and Q_H), and to determine reconstruction settings that achieve an optimal balance between quantification accuracy and image noise for each radionuclide.

The initial phase of this study focused on the optimisation of β and γ combinations for ^{123}I images of the NEMA phantom, with image quality being assessed using the RC, BV, SNR, and Q_H metrics. It was found that $\beta = 0.05{-}0.1$ and $\gamma = 0.5{-}1$ combinations offered the most favourable trade-off between quantification accuracy, contrast recovery, and image noise. Furthermore, the analysis revealed that increasing β generally resulted in lower RC, Q_H and BV values, and higher SNR values. In contrast, variations in γ had only a limited influence on the evaluated metrics within the investigated range.

A MIM workflow for quantitative NEMA phantom analysis was successfully developed. This workflow enabled the systematic analysis of NEMA phantom images, which proved essential for the optimisation procedures, while simultaneously establishing a quantitative workflow that may be implemented in the future at IPO Porto, thereby reducing workload. However, the position of the VOIs used to determine the calibration factor was shown to influence the obtained value, indicating that further work is required to improve the methodology and better approximate the results obtained with the Jaszczak phantom. Overall, averaging six different VOI placements, the calibration factor obtained using the NEMA method presented a relative difference of 4.7% compared with the value obtained using the same number of VOIs evenly distributed throughout the Jaszczak phantom.

In the second phase of this study, Q.Clear reconstruction parameters were optimised for ^{99m}Tc and ^{177}Lu NEMA phantom images. For ^{99m}Tc, it was possible to improve SNR and BV while largely maintaining the RC and Q_H values of the protocol used at IPO Porto. For ^{177}Lu, an optimal protocol was identified that achieved greater recovery than both the protocol previously used at IPO Porto and literature-reported settings. Overall, the optimisation procedure was successful for both radionuclides, yielding the most favourable balance between quantification accuracy, contrast recovery, and image noise among all evaluated settings.

The optimal protocols were subsequently compared with OSEM reconstructions obtained on the Symbia Pro.specta system. For the 15-minute acquisition datasets, Q.Clear achieved similar performance for ^{99m}Tc and superior performance for ^{123}I and ^{177}Lu in terms of RC. Improvements were also observed, particularly for smaller spheres, in Q_H for ^{123}I and ^{177}Lu. Nevertheless, OSEM reconstructions consistently outperformed those of the StarGuide system in noise-related metrics. This behaviour may be partially explained by the emphasis placed on maximising RC during the optimisation process, potentially at the expense of noise performance. Furthermore, given the complexity of Q.Clear and the large number of adjustable parameters, it is reasonable to assume that additional parameter combinations remain unexplored and may further reduce the performance gap between both reconstruction approaches.

Future research should therefore focus on exploring the remaining Q.Clear settings, deepening the understanding of the influence of tools such as By Sens and parameters such as γ, the number of iterations, and the number of subsets, the latter two of which were not investigated in this work. Nevertheless, the present study successfully characterised the influence of β on image quality and quantification metrics, providing a foundation for future optimisation studies. Moreover, as this work was limited to NEMA phantom datasets, future investigations should extend the analysis to patient studies to evaluate the clinical impact of the optimised reconstruction protocols.

In conclusion, this dissertation provided a comprehensive investigation of Q.Clear reconstruction settings for quantitative SPECT imaging. The results demonstrated that careful optimisation of reconstruction parameters can improve the quantitative performance of the StarGuide system and, in several cases, outperform the reconstruction settings currently employed at IPO Porto. Although the complexity of Q.Clear means that additional optimisation opportunities remain unexplored, this work contributes to a deeper understanding of the behaviour of the algorithm in the SPECT domain and establishes a framework for future optimisation studies. Ultimately, the findings presented herein contribute to the ongoing development of quantitative SPECT imaging and support future theranostic and personalised dosimetry applications using the StarGuide system.

References

[1] Y. Bouchareb, A. AlSaadi, J. Zabah, A. Jain, A. Al-Jabri, P. Phiri, J. Shi, G. Delanerolle, and S. R. Sirasanagandla, "Technological Advances in SPECT and SPECT/CT Imaging," *Diagnostics*, vol. 14, no. 13, p. 1431, 2024. [Online]. Available: https://doi.org/10.3390/diagnostics14131431 [Cited on pages xi, 1, 4, 6, 7, and 26.]

[2] S. Yandrapalli and Y. Puckett. (2026) SPECT Imaging. Last updated: October 3, 2022. [Online]. Available: https://www.ncbi.nlm.nih.gov/books/NBK564426/ [Cited on page 3.]

[3] S. R. Cherry, J. A. Sorenson, and M. E. Phelps, *Physics in Nuclear Medicine*, 4th ed. Elsevier, 2012. [Cited on pages 3, 4, 5, 6, 7, 8, 10, 12, 13, 22, 23, 24, 26, 61, and 65.]

[4] J. T. Bushberg, J. A. Seibert, E. M. L. Jr., and J. M. Boone, *The Essential Physics of Medical Imaging*, 3rd ed. Lippincott Williams & Wilkins, 2012. [Cited on pages 4 and 5.]

[5] P. Ritt, "Recent Developments in SPECT/CT," *Seminars in Nuclear Medicine*, vol. 52, no. 3, pp. 276–285, 2022. [Online]. Available: https://doi.org/10.1053/j.semnuclmed.2022.01.004 [Cited on pages 4, 5, 6, and 14.]

[6] H. O. Anger, "Scintillation Camera," *Review of Scientific Instruments*, vol. 29, no. 1, pp. 27–33, 1958. [Online]. Available: https://doi.org/10.1063/1.1710367 [Cited on pages 4 and 5.]

[7] T. E. Peterson and L. R. Furenlid, "SPECT detectors: the Anger Camera and beyond," *Physics in Medicine and Biology*, vol. 56, no. 17, pp. R145–R182, 2011, epub 2011 Aug 9. [Online]. Available: https://doi.org/10.1088/0031-9155/56/17/R01 [Cited on pages 4 and 5.]

[8] G. B. Saha, *Physics and Radiobiology of Nuclear Medicine*, 3rd ed. Springer, 2010. [Cited on pages 5, 6, 7, and 14.]

[9] H. O. Anger, "Scintillation Camera with Multichannel Collimators," *Journal of Nuclear Medicine*, vol. 5, no. 7, pp. 515–531, 1964. [Cited on page 6.]

[10] R. Taillefer, “Scintillation cameras: A new clinical era has come,” *Journal of Nuclear Cardiology*, vol. 29, no. 4, pp. 1942–1945, 2022. [Online]. Available: https://doi.org/10.1007/s12350-021-02660-4 [Cited on pages 6, 8, and 9.]

[11] M. T. Madsen, “Recent Advances in SPECT Imaging,” *Journal of Nuclear Medicine*, vol. 48, no. 4, pp. 661–673, 2007. [Online]. Available: https://doi.org/10.2967/jnumed.106.032680 [Cited on pages 6, 7, and 8.]

[12] E. Enlow and S. Abbaszadeh, “State-of-the-art challenges and emerging technologies in radiation detection for nuclear medicine imaging: A review,” *Frontiers in Physics*, vol. 11, p. 1106546, 2023. [Online]. Available: https://doi.org/10.3389/fphy.2023.1106546 [Cited on pages 6 and 7.]

[13] B. F. Hutton, K. Erlandsson, and K. Thielemans, “Advances in clinical molecular imaging instrumentation,” *Clinical and Translational Imaging*, vol. 6, no. 1, pp. 31–45, 2018. [Online]. Available: https://doi.org/10.1007/s40336-018-0264-0 [Cited on pages xi, 6, 7, and 8.]

[14] H. Zaidi, “Recent developments and future trends in nuclear medicine instrumentation,” *Zeitschrift für Medizinische Physik*, vol. 16, no. 1, pp. 5–17, 2006. [Online]. Available: https://doi.org/10.1078/0939-3889-00288 [Cited on pages 6, 7, and 8.]

[15] S. Xu, G. Liu, Q. Wei, H. Liu, J. Wu, Y. Liu, and Z. He, “Recent advances in radionuclide medical imaging techniques,” *Frontiers in Medicine*, vol. 12, p. 1662020, 2025. [Online]. Available: https://doi.org/10.3389/fmed.2025.1662020 [Cited on page 7.]

[16] M. Noori-Asl and P. Sayyah-Koohi, “Investigation of Response of the Pixelated CZT SPECT Imaging System and Comparison with the Conventional SPECT System,” *Journal of Medical Physics*, vol. 47, no. 4, pp. 374–380, 2022. [Online]. Available: https://doi.org/10.4103/jmp.jmp_41_22 [Cited on pages 7 and 8.]

[17] V. Bora, H. H. Barrett, A. K. Jha, and E. Clarkson, “Impact of the Fano Factor on Position and Energy Estimation in Scintillation Detectors,” *IEEE Transactions on Nuclear Science*, vol. 62, no. 1, pp. 42–56, 2015. [Online]. Available: https://doi.org/10.1109/TNS.2014.2379620 [Cited on page 7.]

[18] A. Lindvall, “Activity quantification of 177Lu using a 360° CZT gamma camera - comparison with a dual-head Anger camera,” Master’s Thesis, Lund University,

2023. [Online]. Available: https://lup.lub.lu.se/student-papers/search/publication/9138749 [Cited on pages 7, 8, 14, and 22.]

[19] G. F. Knoll, *Radiation Detection and Measurement*, 4th ed. John Wiley & Sons, 2010. [Cited on page 8.]

[20] K. Erlandsson, K. Kacperski, D. van Gramberg, and B. F. Hutton, "Performance evaluation of D-SPECT: a novel SPECT system for nuclear cardiology," *Physics in Medicine and Biology*, vol. 54, no. 9, pp. 2635–2649, 2009. [Online]. Available: https://doi.org/10.1088/0031-9155/54/9/003 [Cited on page 8.]

[21] C. Hoog, P. M. Koulibaly, N. Sas, L. Imbert, G. L. Rouzic, R. Popoff, J. N. Badel, and L. Ferrer, "360° CZT-SPECT/CT cameras: 99mTc- and 177Lu-phantom-based evaluation under clinical conditions," *EJNMMI Physics*, vol. 11, no. 1, p. 89, 2024. [Online]. Available: https://doi.org/10.1186/s40658-024-00684-6 [Cited on pages 9, 10, 11, 19, 33, and 40.]

[22] A. Zorz, C. Hoog, P. M. Koulibaly, N. Sas, L. Imbert, G. L. Rouzic, R. Popoff, J. N. Badel, and L. Ferrer, "Performance evaluation of the 3D-ring cadmium-zinc-telluride (CZT) StarGuide system according to the NEMA NU 1-2018 standard," *EJNMMI Physics*, vol. 10, no. 1, p. 70, 2023. [Online]. Available: https://doi.org/10.1186/s40658-024-00671-x [Cited on pages xi, 9, 10, 11, 19, and 38.]

[23] R. Danieli, M. Stella, J. Leube, J. Tran-Gia, C. Marin, C. F. Uribe, B. Vanderlinden, N. Reynaert, P. Flamen, and H. Levillain, "Quantitative 177Lu SPECT/CT imaging for personalized dosimetry using a ring-shaped CZT-based camera," *EJNMMI Phys*, vol. 10, no. 1, p. 64, Oct. 2023. [Online]. Available: https://ejnmmiphys.springeropen.com/articles/10.1186/s40658-023-00586-z [Cited on pages 9, 10, 19, 26, 30, 36, 40, 60, and 81.]

[24] A. Stenvall, I. Ceric Andelius, E. Nilsson, A. Lindvall, E. Larsson, and J. Gustafsson, "Bias and precision of SPECT-based 177Lu activity-concentration estimation using a ring-configured solid-state versus a dual-headed anger system," *EJNMMI Phys*, vol. 11, no. 1, p. 91, Nov. 2024. [Online]. Available: https://ejnmmiphys.springeropen.com/articles/10.1186/s40658-024-00693-5 [Cited on pages 10, 11, 19, and 27.]

[25] *StarGuide Operator Manual*, GE Healthcare. [Cited on pages 9, 10, and 36.]

[26] H. Song, V. Ferri, H. Duan, C. M. Aparici, G. Davidzon, B. L. Franc, F. Moradi, J. Nguyen, J. Shah, and A. Iagaru, “SPECT at the speed of PET: a feasibility study of CZT-based whole-body SPECT/CT in the post 177Lu-DOTATATE and 177Lu-PSMA617 setting,” *Eur. J. Nucl. Med. Mol. Imaging*, vol. 50, no. 8, pp. 2250–2257, Jul. 2023. [Online]. Available: https://doi.org/10.1007/s00259-023-06176-6 [Cited on pages 10 and 19.]

[27] I. Cerić Andelius, D. Minarik, E. Persson, H. Mosén, K. Valind, E. Trägårdh, and J. Oddstig, “First clinical experience of a ring-configured cadmium zinc telluride camera: A comparative study versus conventional gamma camera systems,” *Clin Physio Funct Imaging*, vol. 44, no. 1, pp. 79–88, Jan. 2024. [Online]. Available: https://onlinelibrary.wiley.com/doi/10.1111/cpf.12853 [Cited on pages 10, 11, and 19.]

[28] A. Seret and C. Bernard, “Quantitative capabilities of commercial CZT SPECT-CT cameras with 99mtc,” *EJNMMI Phys.*, vol. 12, no. 1, p. 44, May 2025. [Online]. Available: https://doi.org/10.1186/s40658-025-00754-3 [Cited on pages 11 and 19.]

[29] P. P. Bruyant, “Analytic and Iterative Reconstruction Algorithms in SPECT,” *Journal of Nuclear Medicine*, vol. 43, no. 10, pp. 1343–1358, 2002. [Online]. Available: https://jnm.snmjournals.org/content/43/10/1343 [Cited on pages 11, 12, and 13.]

[30] P. E. Kinahan, M. Defrise, and R. Clackdoyle, “Analytic Image Reconstruction Methods,” in *Emission Tomography: The Fundamentals of PET and SPECT*, M. N. Wernick and J. N. Aarsvold, Eds. Elsevier Academic Press, 2004, pp. 221–245. [Cited on pages xi, 11, 12, and 13.]

[31] J. Qi and R. M. Leahy, “Iterative reconstruction techniques in emission computed tomography,” *Physics in Medicine & Biology*, vol. 51, no. 15, p. R541, jul 2006. [Online]. Available: https://doi.org/10.1088/0031-9155/51/15/R01 [Cited on pages 13, 14, 15, 16, 17, and 18.]

[32] D. S. Lalush and M. N. Wernick, “Iterative Image Reconstruction,” in *Emission Tomography: The Fundamentals of PET and SPECT*, M. N. Wernick and J. N. Aarsvold, Eds. Elsevier Academic Press, 2004, pp. 247–278. [Cited on pages 14, 15, 16, and 17.]

[33] P. J. Green, “Bayesian reconstructions from emission tomography data using a modified EM algorithm,” *IEEE Transactions on Medical Imaging*, vol. 9, no. 1,

pp. 84–93, 1990. [Online]. Available: https://doi.org/10.1109/42.52985 [Cited on page 15.]

[34] L. A. Shepp and Y. Vardi, “Maximum Likelihood Reconstruction for Emission Tomography,” *IEEE Transactions on Medical Imaging*, vol. 1, no. 2, pp. 113–122, 1982. [Online]. Available: https://doi.org/10.1109/TMI.1982.4307559 [Cited on page 15.]

[35] H. M. Hudson and R. S. Larkin, “Accelerated image reconstruction using ordered subsets of projection data,” *IEEE Transactions on Medical Imaging*, vol. 13, no. 4, pp. 601–609, 1994. [Online]. Available: https://doi.org/10.1109/42.363108 [Cited on pages 15 and 16.]

[36] J. Browne and A. R. D. Pierro, “A Row-Action Alternative to the EM Algorithm for Maximizing Likelihoods in Emission Tomography,” *IEEE Transactions on Medical Imaging*, vol. 15, no. 5, pp. 687–699, 1996. [Online]. Available: https://doi.org/10.1109/42.508981 [Cited on pages 16, 18, and 40.]

[37] K. Miwa, T. Yamao, F. Hashimoto, N. Miyaji, Y. Kamitaka, M. Masubuchi, T. Murata, T. Yoshii, R. Kobayashi, S. Fukuda, N. Akiya, K. Wachi, and K. Wagatsuma, “Innovations in clinical PET image reconstruction: advances in Bayesian penalized likelihood algorithm and deep learning,” *Annals of Nuclear Medicine*, vol. 39, no. 9, pp. 875–898, 2025. [Online]. Available: https://doi.org/10.1007/s12149-025-02088-7 [Cited on pages 16, 17, 19, and 40.]

[38] K. M. Hanson, “Introduction to Bayesian image analysis,” in *Medical Imaging: Image Processing, Proceedings of SPIE*, M. H. Loew, Ed., vol. 1898. SPIE – The International Society for Optical Engineering, 1993, pp. 716–731. [Online]. Available: https://doi.org/10.1117/12.154577 [Cited on pages 16 and 17.]

[39] K. Wagatsuma, K. Miwa, Y. Kamitaka, E. Koike, T. Yamao, T. Yoshii, R. Kobayashi, S. Nezu, Y. Sugamata, N. Miyaji, E. Imabayashi, K. Ishibashi, J. Toyohara, and K. Ishii, “Determination of optimal regularization factor in bayesian penalized likelihood reconstruction of brain PET images using [18 F]FDG and [11 C]PiB,” *Med. Phys.*, vol. 49, no. 5, pp. 2995–3005, May 2022. [Online]. Available: https://doi.org/10.1002/mp.15593 [Cited on page 17.]

[40] J. Nuyts, D. Bequé, P. Dupont, and L. Mortelmans, "A Concave Prior Penalizing Relative Differences for Maximum-a-Posteriori Reconstruction in Emission Tomography," *IEEE Transactions on Nuclear Science*, vol. 45, no. 2, pp. 692–699, 1998. [Online]. Available: https://doi.org/10.1109/23.668341 [Cited on page 17.]

[41] E. Asmal, S. Ahn, S. G. Ross, A. Chen, and R. M. Manjeshwar, "Accurate and consistent lesion quantitation with clinically acceptable penalized likelihood images," in *2012 IEEE Nuclear Science Symposium and Medical Imaging Conference Record (NSS/MIC)*, 2012, pp. 4062–4066. [Online]. Available: https://doi.org/10.1109/NSSMIC.2012.6551928 [Cited on page 17.]

[42] S. Ahn, S. G. Ross, E. Asma, J. Miao, X. Jin, L. Cheng, S. D. Wollenweber, and R. M. Manjeshwar, "Quantitative comparison of OSEM and penalized likelihood image reconstruction using relative difference penalties for clinical PET," *Phys. Med. Biol.*, vol. 60, no. 15, pp. 5733–5751, Aug. 2015. [Online]. Available: https://doi.org/10.1088/0031-9155/60/15/5733 [Cited on page 17.]

[43] S. Alenius and U. Ruotsalainen, "Bayesian image reconstruction for emission tomography based on median root prior," *European Journal of Nuclear Medicine*, vol. 24, no. 3, pp. 259–265, 1997. [Online]. Available: https://doi.org/10.1007/BF01728761 [Cited on page 18.]

[44] S. Ahn and J. A. Fessler, "Globally Convergent Image Reconstruction for Emission Tomography Using Relaxed Ordered Subsets Algorithms," *IEEE Transactions on Medical Imaging*, vol. 22, no. 5, pp. 613–626, 2003. [Online]. Available: https://doi.org/10.1109/TMI.2003.810897 [Cited on page 18.]

[45] A. R. de Pierro and M. E. Beleza Yamagishi, "Fast EM-like methods for maximum "a posteriori" estimates in emission tomography," *IEEE Trans. Med. Imaging*, vol. 20, no. 4, pp. 280–288, Apr. 2001. [Online]. Available: https://doi.org/110.1109/42.921477 [Cited on page 18.]

[46] N. Yamaguchi, H. Odagiri, H. Sato, H. Kodama, Y. Tanaka, T. Takeuchi, K. Takanami, A. Usui, and T. Kaneta, "Optimization of block sequential regularized expectation maximization reconstruction parameters for striatal SPECT using a ring-type semiconductor SPECT/CT system," *J. Nucl. Med. Technol.*, vol. 54, no. 1, pp. 71–77, mar 2026. [Online]. Available: https://doi.org/10.2967/jnmt.125.269869 [Cited on page 20.]

[47] D. Cecchin, A. Zorz, R. Lhommel, A. Flaus, P. Tylski, G. Mathoux, N. Hartman, E. Guedj, F. Serani, L. Imbert, and A. Verger, "An european consensus on [123I]Ioflupane acquisition and reconstruction using 3D CZT SPECT/CT," *EJNMMI Phys.*, vol. 13, no. 1, p. 11, Dec. 2025. [Online]. Available: https://doi.org/10.1186/s40658-025-00830-8 [Cited on page 20.]

[48] J. C. Dickson, I. S. Armstrong, P. M. Gabiña, A. M. Denis-Bacelar, A. K. Krizsan, J. M. Gear, T. V. den Wyngaert, L.-F. de Geus-Oei, and K. Herrmann, "EANM practice guideline for quantitative SPECT-CT," *European Journal of Nuclear Medicine and Molecular Imaging*, vol. 50, no. 4, pp. 980–995, 2023. [Online]. Available: https://doi.org/10.1007/s00259-022-06028-9 [Cited on pages 20, 21, 22, 49, and 62.]

[49] D. L. Bailey and K. P. Willowson, "An evidence-based review of quantitative SPECT imaging and potential clinical applications," *Journal of Nuclear Medicine*, vol. 54, no. 1, pp. 83–89, 2013. [Online]. Available: https://doi.org/10.2967/jnumed.112.111476 [Cited on page 20.]

[50] B. J. Burkett, D. J. Bartlett, P. W. McGarrah, A. R. Lewis, D. R. Johnson, K. Berberoğlu, M. K. Pandey, A. T. Packard, T. R. Halfdanarson, C. B. Hruska, G. B. Johnson, and A. T. Kendi, "A Review of Theranostics: Perspectives on Emerging Approaches and Clinical Advancements," *Radiology: Imaging Cancer*, vol. 5, no. 4, p. e220157, 2023. [Online]. Available: https://doi.org/10.1148/rycan.220157 [Cited on page 21.]

[51] A. Könik, J. A. O'Donoghue, R. L. Wahl, M. M. Graham, and A. D. V. den Abbeele, "Theranostics: The Role of Quantitative Nuclear Medicine Imaging," *Seminars in Radiation Oncology*, vol. 31, no. 1, pp. 28–36, 2021. [Online]. Available: https://doi.org/10.1016/j.semradonc.2020.07.003 [Cited on pages 21 and 24.]

[52] A. Yordanova, E. Eppard, S. Kürpig, R. A. Bundschuh, S. Schönberger, M. Gonzalez-Carmona, G. Feldmann, H. Ahmadzadehfar, and M. Essler, "Theranostics in nuclear medicine practice," *OncoTargets and Therapy*, pp. 4821–4828, 2017. [Online]. Available: https://doi.org/10.2147/OTT.S140671 [Cited on page 21.]

[53] Y. K. Dewaraja, E. C. Frey, G. Sgouros, A. B. Brill, P. Roberson, P. B. Zanzonico, and M. Ljungberg, "MIRD pamphlet No. 23: quantitative SPECT for patient-specific 3-dimensional dosimetry in internal radionuclide therapy," *J.*

Nucl. Med., vol. 53, no. 8, pp. 1310–1325, aug 2012. [Online]. Available: https://doi.org/10.2967/jnumed.112.104261 [Cited on pages 21, 22, and 47.]

[54] M. A. Lodge and E. C. Frey, "Nuclear Medicine Imaging Devices," in *The Essential Physics of Medical Imaging*, 3rd ed., J. T. Bushberg, J. A. Seibert, E. M. L. Jr., and J. M. Boone, Eds. Lippincott Williams & Wilkins, 2012, pp. 299–330. [Cited on page 21.]

[55] T. Ichihara, K. Ogawa, N. Motomura, A. Kubo, and S. Hashimoto, "Compton Scatter Compensation Using the Triple-Energy Window Method for Single- and Dual-Isotope SPECT," *Journal of Nuclear Medicine*, vol. 34, no. 12, pp. 2216–2221, 1993. [Online]. Available: https://jnm.snmjournals.org/content/34/12/2216 [Cited on page 21.]

[56] T. Kuwert, J. Hornegger, H. Vija, and P. Ritt, "Absolute quantification in SPECT," *European Journal of Nuclear Medicine and Molecular Imaging*, vol. 38, pp. 69–77, 2011. [Online]. Available: https://doi.org/10.1007/s00259-011-1770-2 [Cited on page 22.]

[57] W. W. Lee and K.-S. Group, "Clinical Applications of Technetium-99m Quantitative Single-Photon Emission Computed Tomography/Computed Tomography," *Nuclear Medicine and Molecular Imaging*, vol. 53, no. 3, pp. 172–181, 2019. [Online]. Available: https://doi.org/10.1007/s13139-019-00588-9 [Cited on page 22.]

[58] A. Grings, C. Jobic, T. Kuwert, and P. Ritt, "The magnitude of the partial volume effect in SPECT imaging of the kidneys: a phantom study," *EJNMMI Physics*, vol. 9, no. 1, p. 18, 2022. [Online]. Available: https://doi.org/10.1186/s40658-022-00446-2 [Cited on page 22.]

[59] Data Spectrum Corporation, "NEMA IEC PET Body Phantom $(NU22018)^{TM}$," https://www.spect.com/pdf/NEMA-IEC-PET-Body-Phantom.pdf, 2025. [Cited on pages 22 and 28.]

[60] Technetium-99m (99m-Tc) Decay Data Tables. https://www.henri-becquerel.fr/decaydata/Tc-99m. Laboratoire Henri Becquerel,. [Cited on page 23.]

[61] Lutetium-177 (177-Lu) Decay Data Tables. https://www.henri-becquerel.fr/decaydata/Lu-177. Laboratoire Henri Becquerel. [Cited on page 24.]

[62] S. Zhang, A. Zhang, X. Qi, Z. Han, L. Song, J. Zhou, G. Wang, R. Zhu, and J. Li, "Radionuclide-Labeled Biomaterials: A Novel Strategy for Tumor-Targeted Therapy," *Biomimetics*, vol. 10, no. 6, p. 394, 2025. [Online]. Available: https://doi.org/10.3390/biomimetics10060394 [Cited on page 24.]

[63] Iodine-123 (I-123) Decay Data Tables. https://www.henri-becquerel.fr/decaydata/I-123. Laboratoire Henri Becquerel. [Cited on page 24.]

[64] T. Niu, M. Fan, B. Lin, F. Gao, B. Tan, and X. Du, "Current clinical application of lutetium-177 in solid tumors (review)," *Exp. Ther. Med.*, vol. 27, no. 5, p. 225, May 2024. [Online]. Available: https://doi.org/10.3892/etm.2024.12514 [Cited on page 26.]

[65] A. Könik, B. Auer, J. De Beenhouwer, K. Kalluri, N. Zeraatkar, L. R. Furenlid, and M. A. King, "Primary, scatter, and penetration characterizations of parallel-hole and pinhole collimators for I-123 SPECT," *Phys. Med. Biol.*, vol. 64, no. 24, p. 245001, Dec. 2019. [Online]. Available: https://doi.org/10.1088/1361-6560/ab58fe [Cited on page 26.]

[66] M. Ljungberg, A. Celler, M. W. Konijnenberg, K. F. Eckerman, Y. K. Dewaraja, K. Sjögreen-Gleisner, SNMMI MIRD Committee, W. E. Bolch, A. B. Brill, F. Fahey, D. R. Fisher, R. Hobbs, R. W. Howell, R. F. Meredith, G. Sgouros, P. Zanzonico, EANM Dosimetry Committee, K. Bacher, C. Chiesa, G. Flux, M. Lassmann, L. Strigari, and S. Walrand, "MIRD pamphlet no. 26: Joint EANM/MIRD guidelines for quantitative 177lu SPECT applied for dosimetry of radiopharmaceutical therapy," *J. Nucl. Med.*, vol. 57, no. 1, pp. 151–162, Jan. 2016. [Online]. Available: https://doi.org/10.2967/jnumed.115.159012 [Cited on pages 26 and 34.]

[67] A. A. Dobbeleir, A.-S. E. Hambÿe, and P. R. Franken, "Influence of high-energy photons on the spectrum of iodine-123 with low- and medium-energy collimators: consequences for imaging with 123 i-labelled compounds in clinical practice," *Eur. J. Nucl. Med. Mol. Imaging*, vol. 26, no. 6, pp. 655–658, May 1999. [Online]. Available: https://doi.org/10.1007/s002590050434 [Cited on page 26.]

[68] P. V. Harper, K. A. Lathrop, F. Jiminez, R. Fink, and A. Gottschalk, "Technetium 99m as a scanning agent," *Radiology*, vol. 85, no. 1, pp. 101–109, Jul. 1965. [Online]. Available: https://doi.org/10.1148/85.1.101 [Cited on page 26.]

[69] C. Desmonts, M. A. Bouthiba, B. Enilorac, C. Nganoa, D. Agostini, and N. Aide, "Evaluation of a new multipurpose whole-body CzT-based camera: comparison with a dual-head anger camera and first clinical images," *EJNMMI Phys.*, vol. 7, no. 1, p. 18, Mar. 2020. [Online]. Available: https://doi.org/10.1186/s40658-020-0284-5 [Cited on page 26.]

[70] E. Goshen, L. Beilin, E. Stern, T. Kenig, R. Goldkorn, and S. Ben-Haim, "Feasibility study of a novel general purpose CZT-based digital SPECT camera: initial clinical results," *EJNMMI Phys.*, vol. 5, no. 1, p. 6, Mar. 2018. [Online]. Available: https://doi.org/10.1186/s40658-018-0205-z [Cited on page 26.]

[71] Alara Consultants Inc., "Jaszczak SPECT Phantom," https://alaraconsultants.com/product/nuclear-medicine/accessories-nuclear-medicine/jaszczak-spect-phantom/, 2021. [Cited on page 31.]

[72] M. Lyra and A. Ploussi, "Filtering in SPECT image reconstruction," *Int. J. Biomed. Imaging*, vol. 2011, p. 693795, Jun. 2011. [Online]. Available: https://doi.org/10.1155/2011/693795 [Cited on page 36.]

[73] O. Ziv, B. Yuzefovich, J. Sachs, and G. Kovalski, "Clarify DL*: Deep Learning Image Reconstruction for Bone SPECT Scans," GE HealthCare, Tech. Rep. [Online]. Available: https://www.gehealthcare.com/content/dam/gehc/global/products/imaging/effortless-imaging/documents/white-paper-clarify-dl-nuclear-medicine-ds-en.pdf [Cited on page 37.]

[74] M. A. Rahman and A. K. Jha, "Task-based assessment of binned and list-mode SPECT systems," *Proc. SPIE*, vol. 11599, p. 1159904, Feb. 2021. [Online]. Available: https://doi.org/10.1117/12.2582266 [Cited on page 37.]

[75] N. Benabdallah, W. Scheve, N. Dunn, D. Silvestros, P. Schelker, D. Abou, U. Jammalamadaka, R. Laforest, Z. Li, J. Liu, D. H. Ballard, N. M. Maughan, H. Gay, B. C. Baumann, R. F. Hobbs, B. Rogers, A. Iravani, A. K. Jha, F. Dehdashti, and D. L. J. Thorek, "Practical considerations for quantitative clinical SPECT/CT imaging of alpha particle emitting radioisotopes," *Theranostics*, vol. 11, no. 20, pp. 9721–9737, Sep. 2021. [Online]. Available: https://doi.org/10.7150/thno.63860 [Cited on page 46.]

[76] D. Kupitz, H. Wissel, J. Wuestemann, S. Bluemel, M. Pech, H. Amthauer, M. C. Kreissl, and O. S. Grosser, "Optimization of SPECT/CT imaging protocols for

quantitative and qualitative 99mtc SPECT," *EJNMMI Phys.*, vol. 8, no. 1, p. 57, Jul. 2021. [Online]. Available: https://doi.org/10.1186/s40658-021-00405-3 [Cited on page 48.]

[77] V. Sawant, P. Diwedi, A. K. Jha, and V. Rangarajan, "Assessment of quantitative accuracy of SPECT/CT in dosimetric studies for 177Lu therapeutic radionuclide," *Health Technol. (Berl.)*, vol. 15, no. 3, pp. 651–659, May 2025. [Online]. Available: https://doi.org/10.1007/s12553-025-00960-0 [Cited on page 48.]

[78] J. I. Gear, M. G. Cox, J. Gustafsson, K. S. Gleisner, I. Murray, G. Glatting, M. Konijnenberg, and G. D. Flux, "EANM practical guidance on uncertainty analysis for molecular radiotherapy absorbed dose calculations," *Eur. J. Nucl. Med. Mol. Imaging*, vol. 45, no. 13, pp. 2456–2474, Dec. 2018. [Online]. Available: https://doi.org/10.1007/s00259-018-4136-7 [Cited on page 59.]

[79] D. Tian, H. Yang, Y. Li, B. Cui, and J. Lu, "The effect of Q.Clear reconstruction on quantification and spatial resolution of 18F-FDG pet in simultaneous PET/MR," *EJNMMI Physics*, vol. 9, 01 2022. [Online]. Available: https://doi.org/10.1186/s40658-021-00428-w [Cited on page 82.]

[80] E. K. Lysvik, L. T. G. Mikalsen, M.-E. Rootwelt-Revheim, K. E. Emblem, and T. Hjørnevik, "Optimization of Q.Clear reconstruction for dynamic 18F PET imaging," *EJNMMI Phys.*, vol. 10, no. 1, p. 65, Oct. 2023. [Online]. Available: https://doi.org/10.1186/s40658-023-00584-1 [Cited on page 82.]